Progressive Damage Modelling of Composite Materials

G R IBRAHIM

PhD 2023

Progressive Damage Modelling of Composite Materials

GHALIB RZAYYIG IBRAHIM

A thesis submitted in partial fulfilment of the requirements of Manchester Metropolitan University for the degree of Doctor of Philosophy

Faculty of Science and Engineering
Manchester Metropolitan University
2023

Abstract

The effects of thermal load combined with mechanical loading of composite laminates are analysed. A new incremental damage evolution law of the cohesive zone model has been developed that can take into account the effects of change in temperature of an interface element. The numerical model results for both test specimens were in good agreement with the data available in the literature.

The second goal of this work was to investigate a cohesive zone model under fatigue loading. A new damage evaluation law and a new evaluation rate of fatigue damage for each cyclic loading ($\partial D/\partial N$) have been presented. Single Lap Joint (SLJ) Model and Double Cantilever Beam (DCB) specimens were used to validate a proposed approach. The results confirmed that the maximum difference between numerical and experimental when using a DCB specimen was 5% at 250 cycles. Whereas the difference between the numerical results and experimental when using a SLJ was 5.2% at 2000 cycles and 4.6 % at 4000 cycles.

Finally, the new damage evolution law for matrix cracking and fibre damage is presented and investigated. The results obtained using the new damage evolution law were in good agreement with experimental results showing that the model presented has the ability to overcome convergence problems in numerical simulations.

Table of contents

List of Figures

List of Tables

A list of symbols

Symbols and Acronyms	Description
G_{IC}, G_{IIC} and G_{IIIC}	critical fracture energies of Modes I, II and III, respectively
δ_m	effective relative displacement
δ_m^f	effective displacement at complete failure
ψ	free potential energy
$\mathbb{C}$	thermodynamic conjugate force
$\mathcal{F}(\mathbb{C}, D)$	damage function
$\mathcal{R}(D)$	the resistance function to the crack propagation
ΔG	strain energy release rate
$\partial a/\partial N$	crack growth rate
G_C	critical fracture energy
R	load ratio
D	static damage parameter
D_f	fatigue damage parameter
τ	cohesive traction
k	interface stiffness
δ	relative displacement
τ_n	normal stress
τ_s	shear stress
τ_t	tear stress
L_u	undamaged part
L_d	damage fatigue crack lengths
L_{CZ}	length of the cohesive zone
E	Young's modulus of the material

σ_{11}	stress in the direction of the fibres
σ_{22}	stress in the transverse direction perpendicular to the fibres
X_T	tensile strength
X_C	compressive strength of the fibres
Y_T	tensile strength
Y_C	compressive strength of the matrix
σ_{12} and S_{12}	stress and transverse shear strength respectively
$\mathbb{F}_i$	Initiation criteria
Ψ	Propagation criteria
ε_{11}^{ft}	maximum values of strain (tension test)
ε_{11}^{fc}	maximum values of strain (compression test)
G_{f11}^{t} and G_{f11}^{c}	Intra-laminar fracture toughness in tension and compression respectively
ω_{11}^{t}, and ω_{11}^{c}	damage parameter symbol of a fibre under tension and compression
E_{11}	longitudinal Young's modulus
ε_{11}^{t} and ε_{11}^{c}	tension and compression strains in the direction of the fibres
ω_{22}^{t}	matrix damage parameter (tension test)
E_{22}	the transverse Young's modulus
Ψ_{22}^{t}	propagation failure criteria of the tension matrix cracking
G_{m22}^{t}	Intra-laminar fracture toughness in tension in the transverse direction
G_{22}	energy release rate during matrix cracking
ω_{22}^{c}	matrix damage parameter under a compressive load

ε_{22}^{c}	compression strain in the transverse direction
Ψ_{22}^{c}	propagation criteria of transverse matrix cracking under compression
G_{m22}^{c}	Intra-laminar fracture toughness in compression for the transverse direction of the compressive load
ω_{12}	damage evolution in plane 12
$d\boldsymbol{\varepsilon}^{\boldsymbol{p}}$	increment in the plastic strain tensor
$\dot{\boldsymbol{\varepsilon}}^{\boldsymbol{p}}$	plastic strain rate
$d\lambda$	plastic multiplier

Declaration

No portion of the work referred in this thesis has been submitted in support of an application for another degree or qualification at this, or any other university, or institute of learning.

Date: 13/03/2023

Signed: Ghalib Ibrahim

Acknowledgements

I would like to thank my supervisor Professor Alhussein Salim Albarbar for his understanding, support and guidance throughout the years I have spent at Manchester Metropolitan University.

Great thanks to my parents, my brothers and my sister. I would also like to thank my wife and son, without them, it would have been difficult to finish my study.

Chapter 1 Introduction

This chapter describes the development and classification of composite materials. It also introduces the advantages and limitations of composite materials and the mechanical analysis of composite laminates. Failure modes of composite laminates and failure criteria are presented in this chapter. Finally, the aims and objectives of the research are given.

1.1 Development of composite material

Many, if not most, naturally occurring biological materials are composites, often combinations of more than two components. Bamboo fibres, which possess good mechanical properties are one example of a natural bi-directional cellular composite, bone and celery are others. Skeletal muscle is composed of bundles of muscle fibres that form a multi-directional natural fibre composite, see Figure 1.1 (Shen 2015).

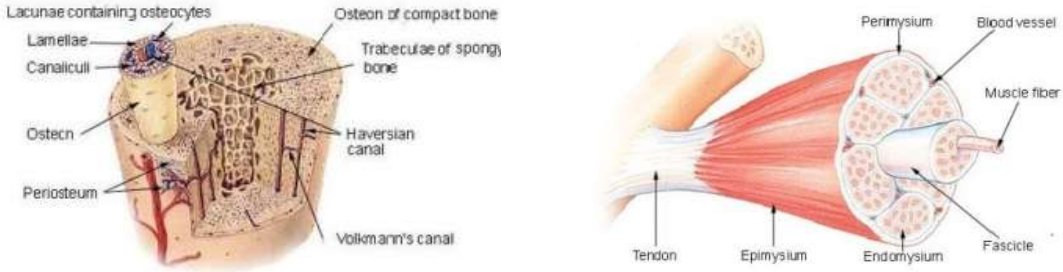

Figure 1.1 Natural composite materials (Shen 2015)

One of the earliest recorded uses of composite materials is the inclusion of straw with mud to make bricks. Improving the properties of one basic material such as clay by adding a second has been a technique chronicled throughout written history. Whether by accident or copying naturally occurring composite materials, such as bamboo, ancient civilisations were adept at mixing two or more components to produce a material more suited to a particular task. From the Ancient Mesopotamians who produced a form of plywood, through the civilisations of Latin America who increased the strength of their pottery by the addition of plant fibres to the Romans who developed an excellent concrete that would set underwater. For over a hundred years, advanced composite materials have been developed for, and used in, the aerospace, automobile and marine industries. The most

widely used composite, fibre-glass, combines relatively strong, stiff, but brittle glass fibres with a reinforcing resin that is relatively weak, flexible and ductile to produce a material that is ductile, flexible, stiff and strong and is widely used in the building and repair of, for example, boats since it was introduced in 1935 by Simpson and Little (Strong 2002).

Fibre reinforced composites (FRCs) possess enhanced stiffness- and strength-to-weight ratios due primarily to the addition of the reinforcement. A supporting framework, or matrix, is needed because of the intrinsic brittleness of the fibre reinforcement. The matrix serves a number of functions: it protects the fibres from any hostile environment, it shares the load between the fibres, and it binds the fibres together while isolating them from each other. The framework also bears the shear stresses in the FRC and limits the initiation and transmission of cracks. The more recent development of composite materials has been due to rapid advances made in developing new fibres (e.g., especially carbon, but also aramid and boron), and composite structures with ceramic and metal matrices. The greater strength of these new composites makes them especially suitable for the extreme conditions experienced in aerospace and military applications. Indeed, at the press conference at which the Airbus A350 XWB was launched it was described as having over half of the airframe (fuselage, wings and tail) made from advanced composites including, for example, carbon/epoxy laminates in the wings, see Figure 1.2. The wide use of composites in the A350 XWB reduced its weight significantly and increased fuel efficiency (Mrazova 2013).

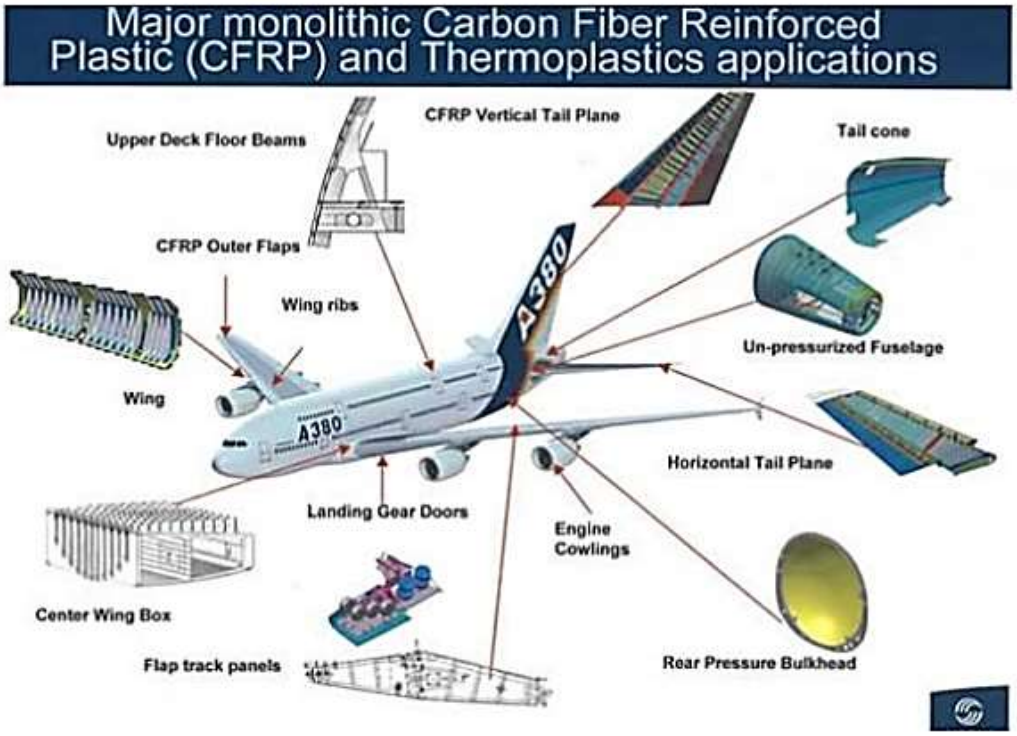

Figure 1.2 Applications of modern composite materials (Mrazova 2013)

1.2 Classification of composite materials

Generally composite materials comprise a continuous phase in which is implanted a discontinuous phase. The former is the matrix and this is reinforced by the latter which is substantially stronger and stiffer. The two most common methods classify composite materials according to (a) the material comprising the matrix: ceramic, metal or polymer, and (b) the geometry of the reinforcement: fibre, flake or particulate.

At present, one of the most widely used matrices in composites is fibre reinforced polymers (FRPs). It is possible to form the reinforcing fibre from a variety of substances, including carbon, aramid and glass. Materials commonly used as matrices include thermosets such as epoxies, phenolics, polyamides polyester and polypropylene and thermoplastics such as PEEK and PPS (Bunsell and Renard 2005)

1.3 Composite materials: advantages and limitations

Measured against commonly used materials, including metals and metal alloys, epoxy composites with carbon fibre reinforcement offer enhanced specific strength and specific elastic modulus, see Figure 1.3. These are important advantages when applied to aircraft construction. Additional important engineering advantages of composite materials include the possibility of optimising the desired mechanical properties by tuning the production of the composite material and hence extending design possibilities. For example, enhancing resistance to electrochemical corrosion would enhance operation stability, while part consolidation would reduce assembly cost and time (Llorca et al., 2013)

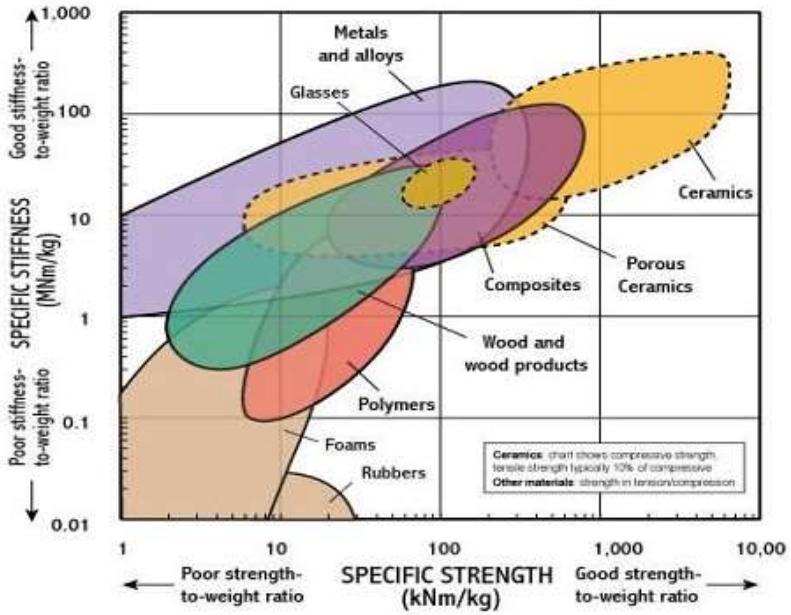

Figure 1.3 Specific strength and modulus of selected materials (Llorca et al., 2013)

Certain limitations with respect to conventional engineering materials constrain the applications of composite materials (Barbero 2011):

- High cost of fabrication.
- Complex nature of anisotropic composites

- Difficulty of analysis of anisotropic composites.
- Complex failure mechanisms
- Difficulty in detecting internal damage.
- Damage repair costly and complexity

1.4 An introduction to composite laminates

While composite laminates (CLs) are widely used in the aerospace industry the understanding of their failure mechanisms when subject to low velocity (LV) impact is inadequate, and this limits their applications. This gap in current knowledge needs to be filled if their potential is to be fully realised (Bouvet et al., 2012)

1.4.1 Characterisation of composite laminates

The lamina in a CL is, typically, a thin fibre reinforced layer with either a unidirectional fibre orientation, see Figure 1.4 (a), or configured as a woven fibre, see Figure 1.4 (b). CLs are formed by stacking laminas one on another, building up the thickness, see Figure 1.4 (c). The process which bonds the laminas together will depend on the materials which comprise the matrix and will include autoclave curing and resin transfer moulding (Bilisik and Syduzzaman 2021)

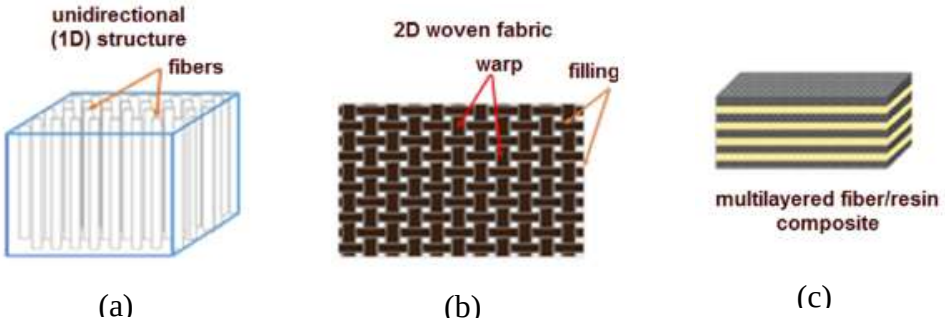

Figure 1.4 Schematic of (a) Unidirectional composite laminate and (b) Woven composite laminate (Bilisik and Syduzzaman 2021)

1.4.2 Lay-up of composite laminates

Generally, appropriate configurations of the build (lay-up) of CLs are able to provide the required structural stiffness and strength, and resistance to impacts perpendicular to the plane required in many structures including the bodies of aircraft. Composite materials of, say, woven laminates where the fibres are woven to form a sheet/layer can often be considered as quasi-isotropic. However, CLs made of unidirectional layers (plies) are usually anisotropic because the principal material axis of each ply is in a different direction. The builds of CLs made of unidirectional laminas, where it is assumed the plies are all of the same materials and thicknesses, can be separated into six classes which are defined by the relative orientations of the fibres (Balzani and Wagner 2008) and (Shen 2015):

- Unidirectional laminates: multiple plies with fibres aligned in one direction (e.g., $[0]_s$)
- Cross-ply laminates: the plies are laid so that the laminates are symmetrical or anti-symmetrical but with the orientations constrained to, e.g., $[0/90]_s$, as shown in Figure 1.5.

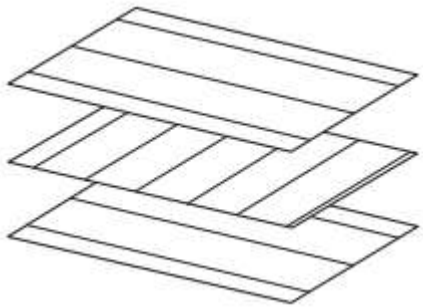

Figure 1.5 Schematic of cross-ply laminates (Mallick 2007)

•Symmetric laminates: plies are laid symmetrically with respect to the mid-ply, these are usually $[\pm 45/0/90]_s$. Plies equidistant above and below the mid-plane have the same orientation.

•Antisymmetric laminates: pairs of laminas with opposite fibre orientations are stacked symmetrically so that plies equidistant above and below the mid-plane have opposite orientations, e.g., [+45/-45/+45/-45].

•Angle-ply laminates: the plies may be laid symmetrically or anti-symmetrically with the orientation of pairs of plies $\pm\theta$ (e.g., [+30/-30/+30/-30]), as shown in Figure 1.6.

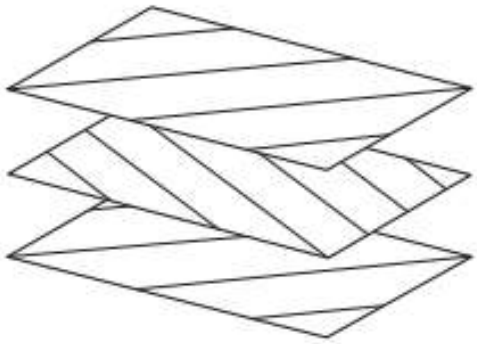

Figure 1.6 Schematic of angle-ply laminates (Mallick 2007)

•Quasi-isotropic laminates: plies are laid in the order $[\pm 45/0/90]_s$) to obtain the required in-plane isotropic properties.

1.4.3 Mechanical analysis of composite laminates

There is a comprehensive literature available in the public domain describing the accurate measurement of the mechanical performance of CLs. Typically, the first step is to measure the matrices representing compliance and stiffness of individual unidirectional lamina. The next step, usually, is to experimentally investigate the performance of laminate

composites as a function of ply thickness and build configuration (Mallick 2007)

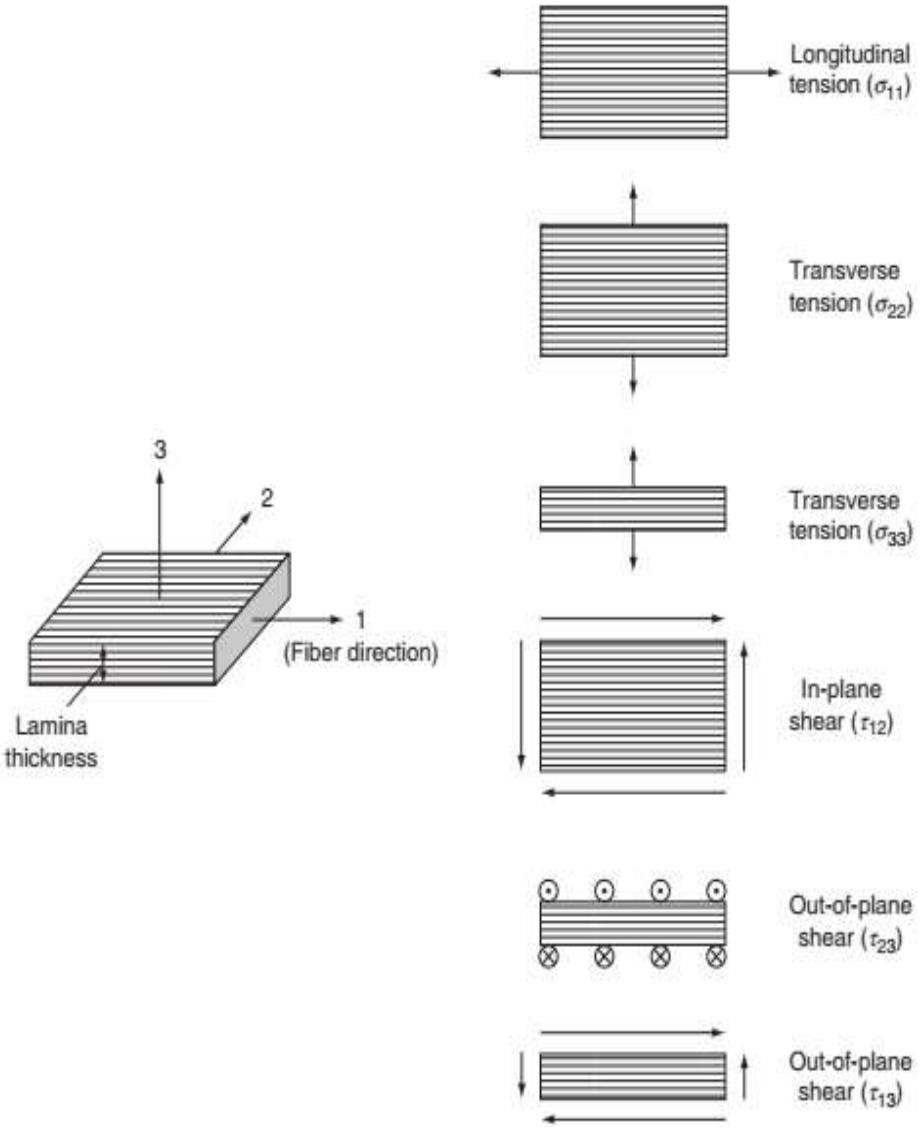

Figure 1.7 Schematic of normal and shear stress on a unidirectional fibre composite (Mallick 2007)

To determine a lamina's compliance in terms of its elasticity, normal stresses are applied, in turn, in the directions of the principal axes as shown in Figure 1.7. For applied stress, σ_1, the relationships between strains ε_1, ε_2, and ε_3, respectively, in the directions 1, 2, and 3 shown in Figure 1.7, and the material's elasticity can be written (Mallick 2007):

$$\varepsilon_1 = \frac{\sigma_1}{E_1}, \qquad \varepsilon_2 = \frac{-\nu_{12}\sigma_1}{E_1}, \qquad \varepsilon_3 = \frac{-\nu_{13}\sigma_1}{E_1}$$

When σ_2 is the only stress component, the developed strains are:

$$\varepsilon_1 = \frac{-\nu_{21}\sigma_2}{E_2}, \qquad \varepsilon_2 = \frac{\sigma_2}{E_2}, \qquad \varepsilon_3 = \frac{-\nu_{23}\sigma_2}{E_2}$$

When σ_3 is the only stress component, the developed strains are:

$$\varepsilon_1 = \frac{-\nu_{31}\sigma_3}{E_3}, \qquad \varepsilon_2 = \frac{-\upsilon_{32}\sigma_3}{E_3}, \qquad \varepsilon_3 = \frac{\sigma_3}{E_3}$$

where, $E_{i=1,2,3}$ is the modulus of elasticity in the *i*-direction, and

$$\text{vij} = -\left(\frac{\text{normal strain along } j \text{ direction}}{\text{normal strain along } i \text{ direction}}\right).$$

The compliance matrix, $[S]$, is found by combining the above equations with the relation:

$$[S] = \begin{bmatrix} \frac{1}{E_1} & \frac{-\upsilon_{12}}{E_1} & \frac{-\upsilon_{13}}{E_1} & 0 & 0 & 0 \\ \frac{-\upsilon_{21}}{E_2} & \frac{1}{E_2} & \frac{-\upsilon_{23}}{E_2} & 0 & 0 & 0 \\ \frac{-\upsilon_{31}}{E_3} & \frac{-\upsilon_{32}}{E_3} & \frac{1}{E_3} & 0 & 0 & 0 \\ 0 & 0 & 0 & \frac{1}{G_{23}} & 0 & 0 \\ 0 & 0 & 0 & 0 & \frac{1}{G_{31}} & 0 \\ 0 & 0 & 0 & 0 & 0 & \frac{1}{G_{12}} \end{bmatrix}$$

1.4.4 Failure modes of composite laminates

In CLs under an applied load, it is an individual ply that is the first to fail. Additional loads can be applied before the entire laminate fails. The manner in which the laminate fails is complicated, affecting both intra-laminar and inter-laminar damage mechanisms. The former will include cracks in the matrix that propagate normal to the plane of the laminate and can cause fibre fracture, the latter implies delamination and progressive separation of the plies. The most prevailing failure modes of composite materials can be categorized into two main groups. First the intra-laminar damages, such as

matrix cracking, fibre/matrix deboning or fibre breakage. Second the interlaminar damages, the damages constructing on the interface between two layers ‘’delamination’’.

The matrix crack shown in Figure 1.8 caused by compressive, shear and tensile stresses generated by a LV impact is parallel to the direction of the fibre. The delamination seen at the bottom of the figure is separation between adjacent plies with different orientations of the fibres, and is initiated by inter-laminar stresses generated by mismatch of the bending stiffnesses of adjacent layers. Fracture of the fibres usually takes place after matrix cracking and delamination. Fibres break when subject to large tensile stresses and buckle when subject to large compressive loads. Penetration is a form of macroscopic damage that takes place when the failure of the laminate rises to a catastrophic level, which is unusual with LV impacts. Much research has been carried out to obtain a comprehensive grasp of how damage is initiated and propagates in CLs under LV impacts (Shi et al., 2012).

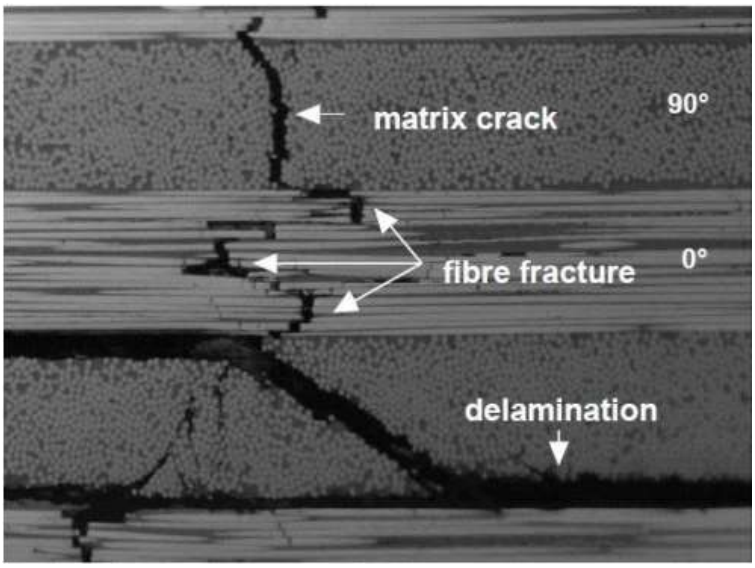

Figure 1.8 Cross-section of impact damaged composite laminate (Al-Hadrayi and Chwei 2016)

1.4.4.1 Matrix cracks

The distribution of cracks in the matrix is complex and not easy to predict accurately but, fortunately, the performance of CLs is not significantly affected by such cracks on their own. However, damage to the matrix, including cracks and debonding of matrix and fibre, can induce delamination at the interface and signal the beginning of other failure mechanisms.

(Zhang 1998) has described a characteristic damage pattern for CLs subject to LV impact, see Figure 9. The point of impact ("1" in Figure 1.9), shows highly localized contact damage which is referred to as "crushing", and can reach two or three layers into the specimen depending on the Hertz type contact forces, the local stresses that occur across the curved surfaces as they deform under the impact will be a function of the transverse stiffness of the material comprising the initial layer. Shear cracks in the face at the impact site are generated by large transverse shear stresses combined with compressive bending strains initiated by the impact. They will appear at the edge(s) of the impactor ("2" in Figure 1.9) and will be at an angle of about 45° to the mid-plane. The matrix fractures due to cracking of the lower face ("3" in Figure 1.9) are referred to as tensile cracks and are induced by large values of the in-plane normal stress/tensile bending strains due to flexural deformation of the plies. Delaminations near the mid plane, on faces nearer the impact are initiated by shear cracks and on faces further from the impact by tensile cracks ("4" and "5" respectively in Figure 1.9). When the sharp tip of a crack extends to the interface between plies, a concentration of stresses at the interface can initiate delamination.

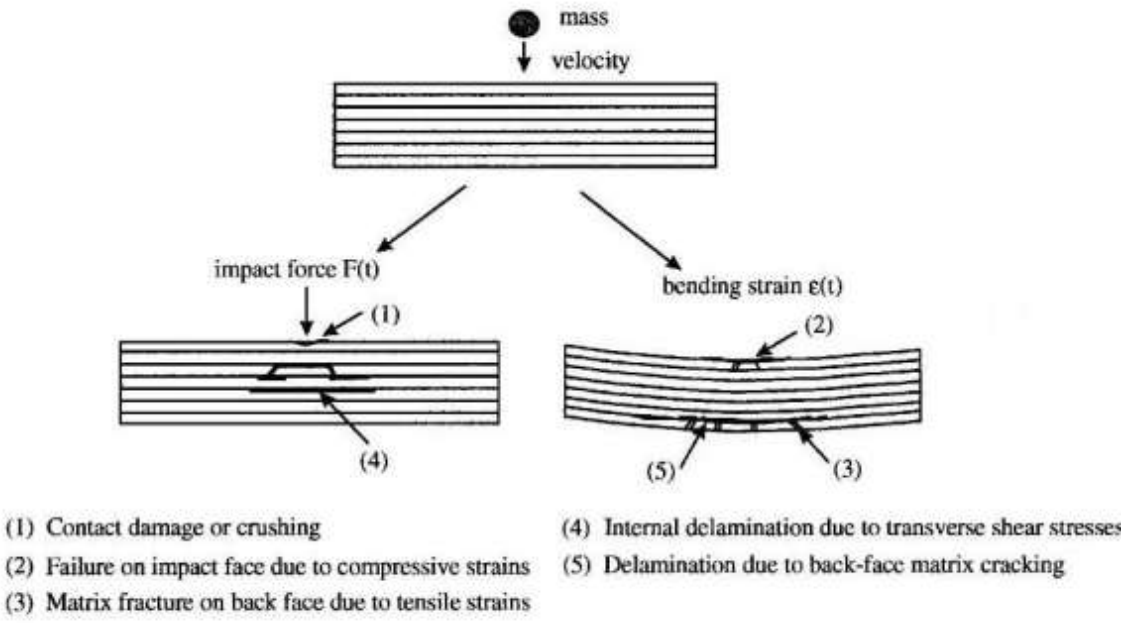

Figure 1.9 Schematic of LV impact damage in a composite laminate (Zhang 1998)

1.4.4.2 Delamination

Delamination is a dominant mechanism in transmitting damage in CLs subject to LV impact. Delamination and generation of cracks in the matrix interact and contribute up to 60% of the degradation of the compressive strength of the laminate. Delamination is believed to begin when the impact force is above a critical value, termed the delamination threshold load. Experimental research has consistently reported that delamination takes place primarily at ply interfaces with different orientations of fibres and explains the phenomenon as the result of the mismatch between bending stiffness and Poisson's ratio. Figure 1.10(a) presents the results of C-scan observations of the top and side views of delamination in a 32-ply laminate. The top-view shows that area of delamination has a circular projection, while the view from the side shows the circular appearance is the combination of multiple delaminations at different interfaces and shows that the delaminations tend to spread with distance into the laminate (Olsson 2012).

The shapes of the areas of the individual delaminations tend to be a ‘peanut’ with its major axis aligned with the fibres in the lower layer, see Figure 1.10(b). It can be seen that the delamination shapes become less regular with orientations that become more difficult to ascertain due to shadowing of the lower layers by the upper (Ellison and Kim 2020).

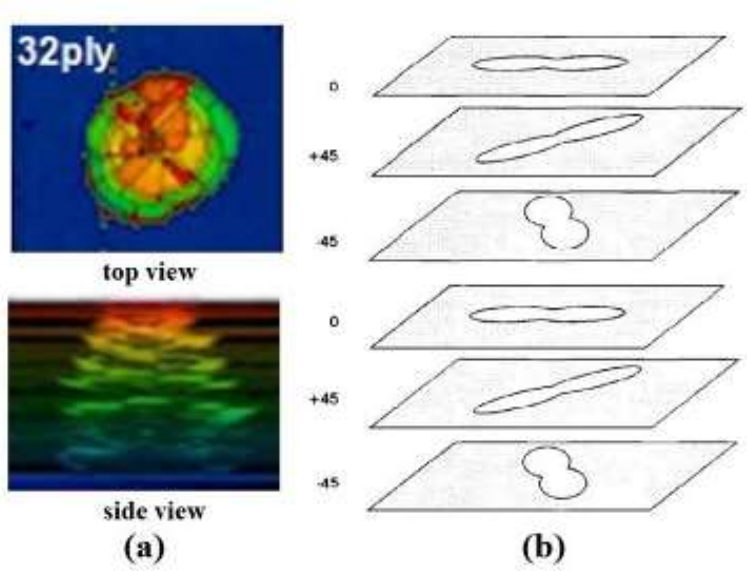

Figure 1.10 (a) Plan and lateral views of delaminations derived from C-scan observations (b) schematic of delaminations (Olsson 2012)

1.4.4.3 Fibre fracture

Matrix cracks generated by LV impacts are considered as precursors of delamination due to their weakening of the residual strength of CLs , whereas under high velocity impacts, fibre fracture is considered a precursor to the catastrophic failure of CLs. Fibre fracture generally occurs after the appearance of the matrix cracks and delamination due to the decrease in protection given by the matrix to the brittle fibres. A matrix which is damaged cannot ensure a load is uniformly distributed between fibres, which can cause high stress concentrations. In general, fibre failure modes occur in two main ways, tensile breakage, and compressive buckling. One established model for in-tension fibre breakage has proposed that the

breakage is due to high levels of bending stress in the non-impacted surface; and buckling of fibres and indentations are caused by high local contact stresses due to the impact. However, accurately predicting fibre fracture remains difficult, depending on successfully modelling every damage mode, including matrix cracks and delamination, as well as interactions between them as the damage progresses (Ouyang et al., 2021).

1.4.5 Composite laminates, failure criteria

A material's capacity to withstand tensile loads before failing is often referred to as its strength. Many failure criteria for CLs have been suggested based on experimentally obtained results. Maximum stress and strain were the earliest, and these have been modified and improved by many researchers. However, it is not possible to define the strength of a composite material in a simple manner because the material is anisotropic. CLs are anisotropic, they have three principal axes, which means the direction of principal stress may not be the same as the direction of principal strain. Additionally, CLs will present different strengths in different directions so that maximum strength as determined by simulation or measurement may not be in the direction of the applied critical loading. Thus, failure criteria for CLs must be determined via appropriate comparisons of applied stress fields and permitted strains (Jiang et al., 2017). The failure criteria include maximum stress criterion, maximum strain criterion, Tsai-Hill failure criterion, Hoffman Failure Criterion and the Hashin criterion (Knight 2006).

1.5 Aim of research and objectives

This study presents a cohesive zone model combining mechanical and thermal effects. Also, it will present a new approach to assessing static damage evaluation and incremental damage degradation law. In additional, the aim of this study is to present new rate of fatigue damage ($\partial \mathrm{D}/\partial \mathrm{N}$) and to develop progressive damage model of transverse matrix cracking

The objectives of the present study can be stated as:

1. Background reading and literature survey to determine research gaps and modelling strategies.
2. To derive a realistic inter-laminar damage model and implement it in finite element software using UMAT subroutine. Then, incorporating thermal effects into the model.
3. To investigate fatigue damage degradation to develop a new rate of fatigue damage ($\partial \mathrm{D}/\partial \mathrm{N}$).
4. To investigate intra-laminar damage in the laminated composites and implement the damage model using UMAT subroutine.
5. Assessing the performance of the developed model using experimental data available in the literature and paving the path for developing effective condition monitoring methods for detecting potential failures in composites e.g., aerospace, wind turbine blades, etc.

1.6 Organisation of the thesis

This thesis will be organised as shown in Figure 1.11.

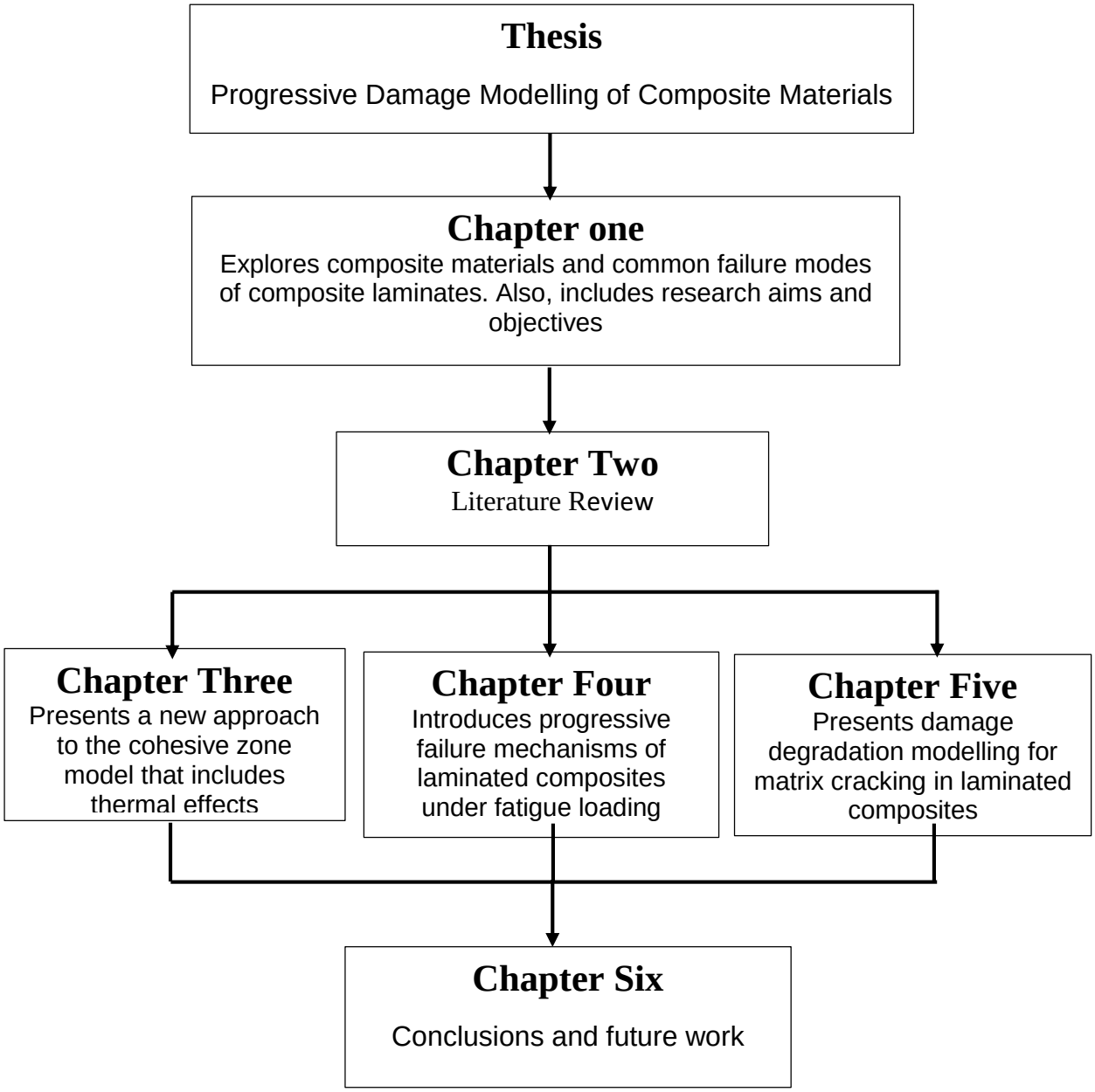

Figure 1.11 Flowchart of thesis outline

Chapter 2 Literature review

This chapter reviews research literature, and efforts to develop a cohesive zone model for composite laminates. This chapter is subdivided into four main sections. The first section explores the thermal effect on composite laminates. The second and third sections introduce fatigue loading and Intra-laminar damage, respectively. The fourth section presents the identification of the research gap.

2.1 Introduction

Composite materials offer many advantages compared to metals and metal-alloys due to their superior mechanical performance, especially where high strength and stiffness to weight ratios are concerned. Thus, advanced composite structures have been widely used in several industrial sectors such as aerospace, rotor blades in wind-energy systems, sports equipment, automotive parts, pressure vessels, among many other applications. However, static, dynamic or thermal load conditions may induce different forms of damage in composite structures which may then exhibit brittle behaviour. This can seriously degrade the stiffness of the component which then provides little damage resistance. And, of course, the load-carrying capability of composite materials decreases if internal damage is present. Modelling the progressive damage of composite materials under different load conditions is an important area, especially with, say, the rotor blades in wind-energy systems where barely visible impact damage can be a critical issue. The demand for high-performance laminated composite materials, especially with regard to long fatigue life, complex geometries and low temperature processing, requires the development of modelling tools that can reliably predict progressive damage, including damage occurring from a range of physical mechanisms (Shi et al., 2012) and (Reinoso et al., 2017).

2.2Thermal effect

(Reed and Golda 1994) investigated the effect of cryogenic temperature (-196^{o}C) on unidirectional CFRP laminates. Their experiments were performed under tensile and compressive loads, and the results indicated that the elastic modulus of CFRP increased by about 10% at a temperature of -196^{o}C. It was also noted that the tensile strength was enhanced at this low temperature.

(Rio et al., 2005) carried out low impact velocity tests on square carbon fibre /epoxy (CFRP) laminates with different stacking sequences (e.g. unidirectional, woven and cross ply) at temperatures ranging from room temperature down to -150^{o}C. The specimens were tested using a drop weight tower device as shown in Figure 2.1. The experimental results showed that there was a clear damage dependency on temperature and laminate type.

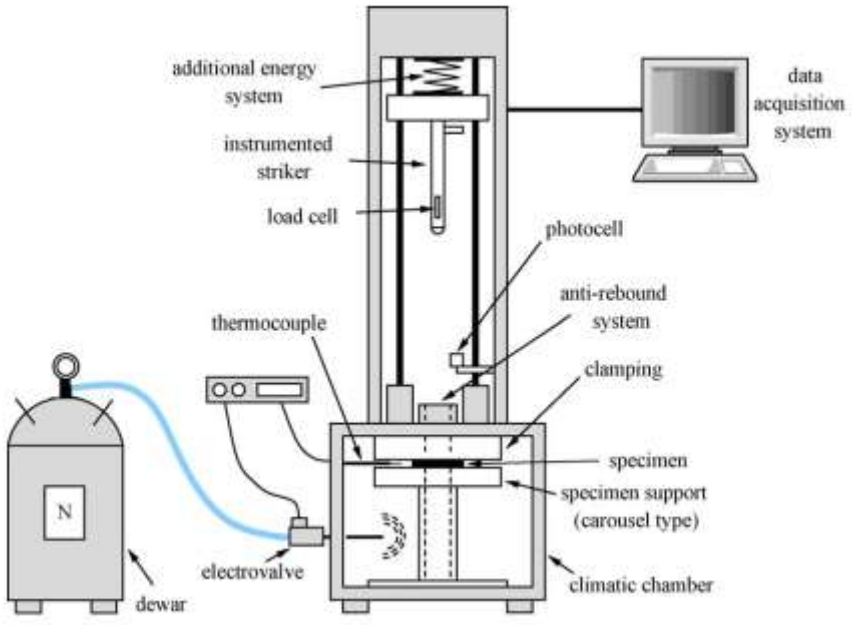

Figure 2.1 Drop weight tower with the cooling system (Rio et al., 2005)

The influence of temperature on Kevlar/glass composite laminates was investigated by (Khojin et al., 2006). The tests were examined under low velocity impact and temperature range is 50^{o}C to 120^{o}C. The findings indicated that the temperature has a significant effect on the behaviour of laminated composite.

(Ibekwe et al., 2007) used two types of beams; one was glass fibre reinforced unidirectional and the second it was a cross-ply laminated composite. Both beams were testing at low temperatures under low velocity impact and then were subjected to compression after impact (CAI) testing as shown in Figure 2.2. Fifty effective specimens (25 unidirectional and 25 cross-ply) were used in the tests. The experimental tests were carried out at temperatures 0^{o}C, -10^{o}C, and -20^{o}C. Also, the tests were conducted at temperatures 20^{o}C and 10^{o}C for comparisons. The influence of temperatures on the damage and elastic modulus was evaluated based on the findings of the experiments.

Figure 2.2 Test set-up for compressive test (Ibekwe et al., 2007)

(Ibekwe et al., 2007) used an optical microscope to take the images of the damage shape and area at the back surface of the specimens. Unidirectional and cross-ply specimens were impacted at different temperatures, the developed damage under 10^{o}C, -10^{o}C is illustrated in Figure 2.3. It is observed that the delamination area was elongated in the direction of the fibre for unidirectional specimens while the shape of delamination for cross-ply specimens is somewhat circular. The effect of temperature on the damaged area is clearly seen in Figure 2.3. The delamination area becomes bigger when the temperature was lower for both unidirectional and cross-ply specimens. The reason behind this is the resin matrix becomes more brittle when the specimen is at a lower temperature.

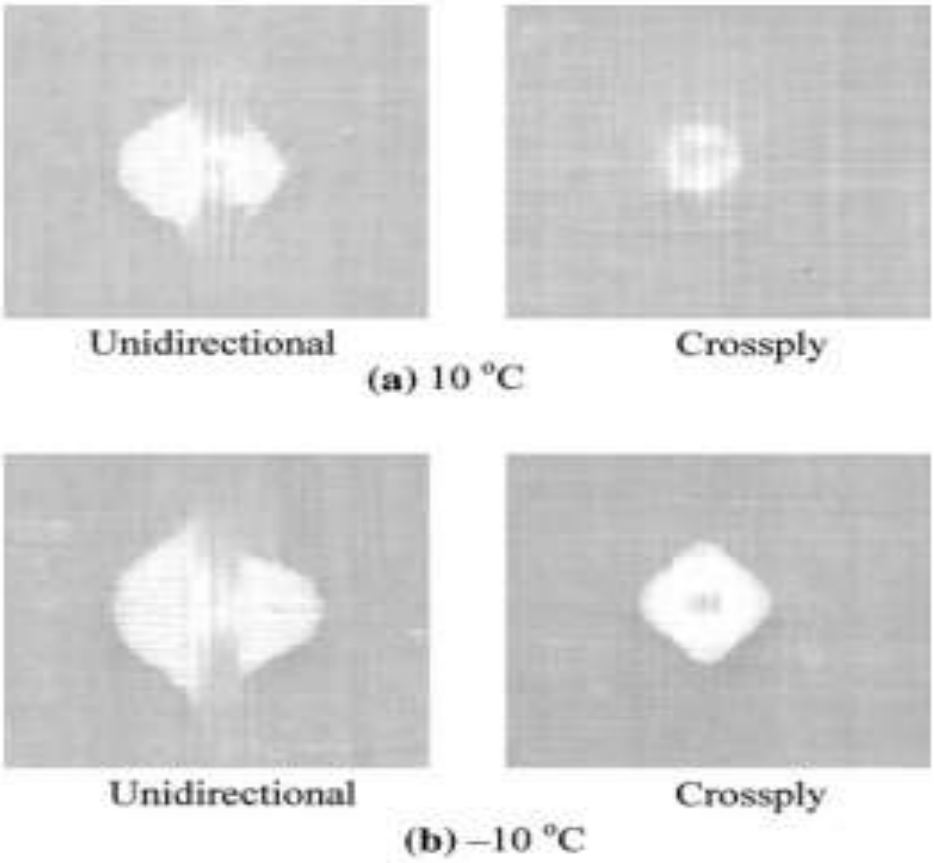

Figure 2.3 Developed damage at back surface (Ibekwe et al., 2007)

(Aktas et al., 2009) studied behaviour of composite materials at different temperatures 20 °C, 60 °C and 100 °C, subjected to impact loading. Their investigation confirmed that the effect of the maximum contact force was not affected by increasing the surrounding temperature.

(Icten et al., 2009) studied the behaviour of laminated composites under impact loading at different environmental temperatures (20 ^{o}C, -20 ^{o}C and -60 ^{o}C) experimentally. The stacking sequence of the composite specimens was $[0/90/45/45]_{s}$. A Fractovis Plus impact test machine integrated with an environmental conditioning chamber was used to carry out the tests at different temperatures, as shown in Figure 2.4. The environmental chamber could provide a temperature range of between -100 ^{o}C and +150 ^{o}C using liquid nitrogen and an electronic thermostatic controller. Different impact energies (5 J to 70 J) were used to investigate characteristics of the laminated composites such as contact load, contact time and absorbed energy. Results indicated that the testing temperature has a significant effect on the impact characteristics when the impact energy is larger than 20 J.

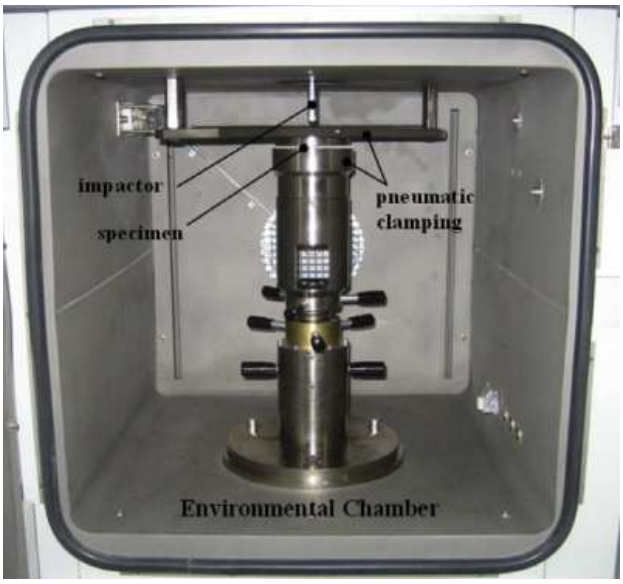

Figure 2.4 Impact testing machine (Icten et al., 2009)

(Sayer et al., 2012) experimental investigated the behavioural response carbon– glass fibre/epoxy (hybrid composites) subjected to impact loading under different temperatures. The impact tests were performed at various temperatures using Instron -Dynatup 9250 HV model instrumented drop weight integrated with an environmental conditioning system. Different temperatures above and below room temperature were chosen to see the influences of temperature on the impact response of laminated composite. Test results indicated that the maximum effect of temperatures on impact characteristics happens at values -20 ^{o}C or -60 ^{o}C. Also, they found that, at impact energies less than 15 J, the damage develops underneath the contact point between the indenter and specimen. But the damage i.e., fibre breakage through-thickness, matrix cracking, and delamination occurred between adjacent layers if the impact energy increases to above 15 J.

(Boominathan et al., 2014) subjected unidirectional and cross-ply (0/90) carbon/epoxy laminates to impacts with energy of 2.17 J at temperatures 30^{o}C, 55^{o}C, 75^{o}C and 90^{o}C. A CEAST Fractovis Drop impact tower, shown in Figure 2.5, was used in their investigation. They found the percentage reduction in flexural strength for both cross ply and unidirectional laminates impacted at high temperatures is lower than for those tested at room temperature.

Figure 2.5 Drop impact tower (Boominathan et al., 2014)

(Suvarna et al., 2014) studied the performance of CFRP laminates for low velocity impact (2 m/s) over a range of ambient temperatures: 30 ^{o}C, 55 ^{o}C, 75 ^{o}C and 90 ^{o}C). Ultrasonic C-scan and microfocus X-rays were used to capture the internal damage at the four temperatures as presented in Figure 2.6. As shown in the figure, the damage grows beneath the impact point leading to (i) intralaminar damage (matrix cracking) and (ii) delamination. They found that at the highest temperature, the damage can clearly be seen in the laminated composite specimen.

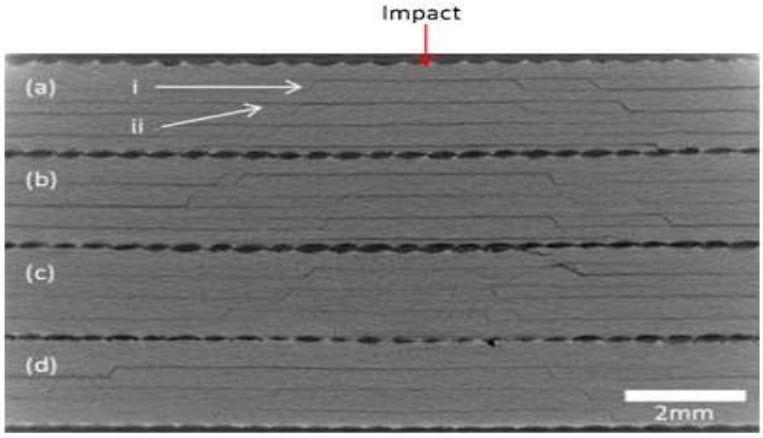

Figure 2.6 CT cross section of damage at different temperatures (Suvarna et al., 2014)

(Amaro et al., 2016) subjected CFRP to single and multiple impact tests. Two impact energies were used (1 J and 3 J) and the experiments were carried out at three different temperatures, room temperature, 60 ^{o}C, and 90 ^{o}C. The drop testing machine and experimental set-up are illustrated in Figure 2.7. Typical damages obtained by the authors experimentally at room temperature when the specimens were subjected to impact energies 1 J and 3 J are illustrated in Figure 2.8. It was observed that the temperature had a strong effect on matrix properties (stiffness and strength) and on the impact bending stiffness when low energy impacts were used, but that at the higher impact energy, the influence of temperature vanished. The number of impacts to failure remained constant at about four for impact energy of 3 J, but decreased with increase in temperature for impact energy of 1 J, from about twenty at room temperature to about fourteen at 90^{o}C.

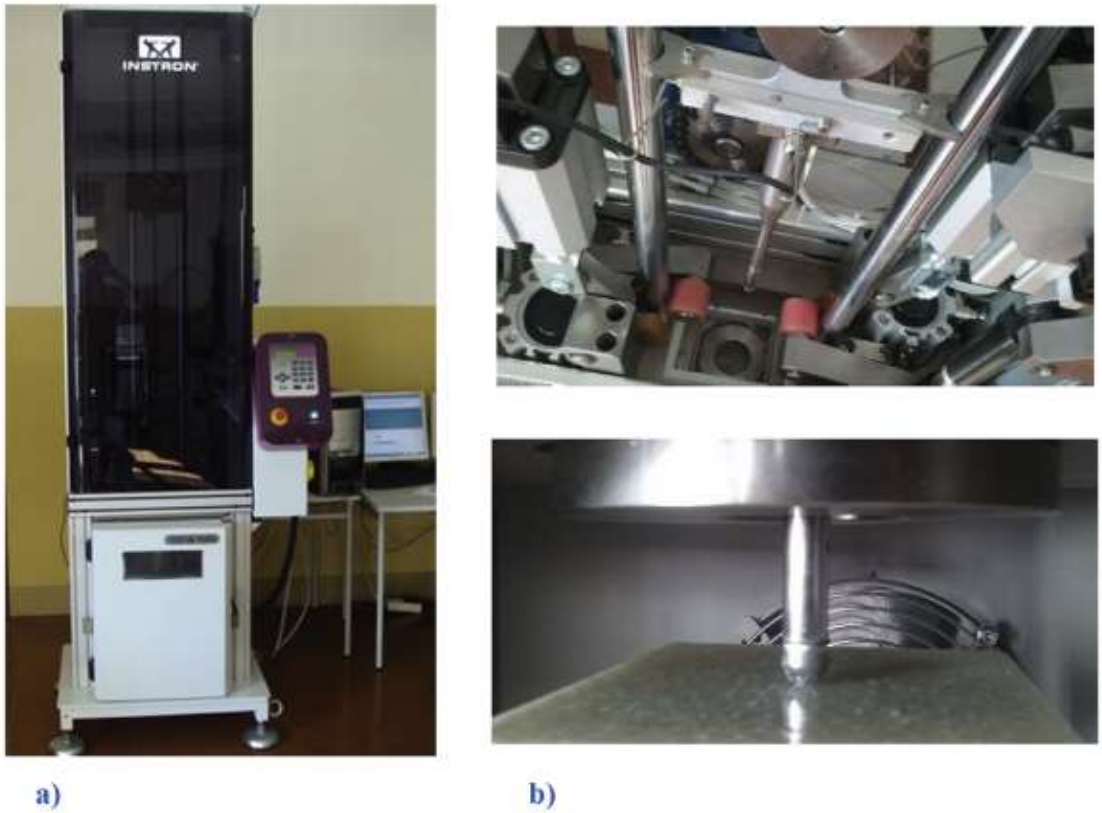

Figure 2.7 a) Drop testing machine; b) Experimental set-up (Amaro et al., 2016)

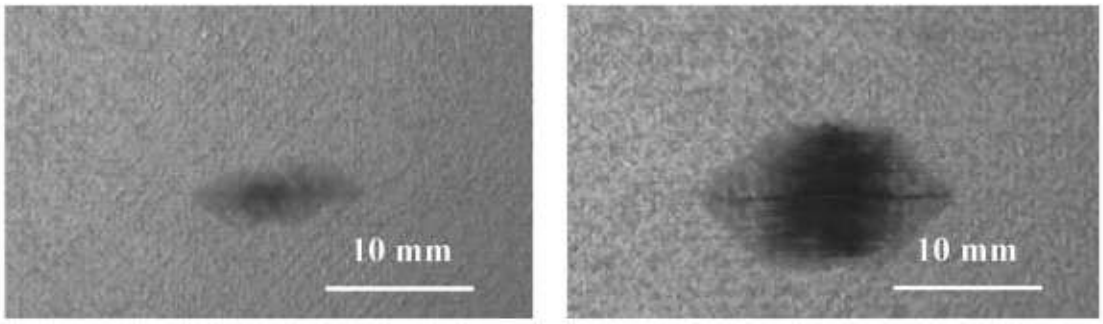

Figure 2.8 Typical damage obtained experimentally (Amaro et al., 2016) a) 1 J and b) 3 J

(Boumbimba et al., 2017) investigated thermoplastic resin composite (Pure_Acry/GF and Acry_Nano10/GF) behaviour under impact loading at temperatures of − 80 °C, 20 °C and 80 °C. Damage images were obtained by X-ray microtomography of impacted samples of Pure_Acry/GF and Acry_Nano10/GF as shown in Figures 2.9 and 2.10.The results revealed that the impact resistance increases when the temperature decreases. The damage zone extended with increase in temperature. Especially, the delamination area increased when the temperature and impact energy increased, also severe fibre breakage happened at the high-temperatures.

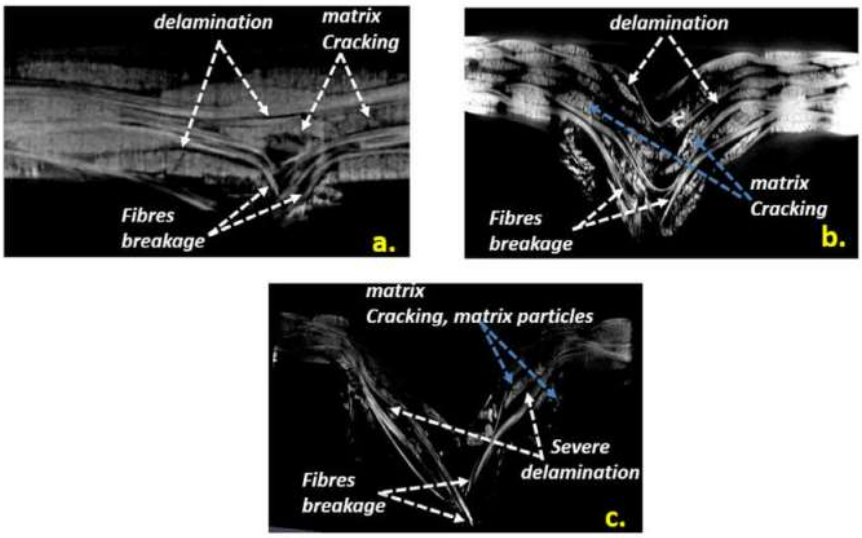

Figure 2.9 X-ray microtomography of damage behaviour in pure_Acry/GF at 40 J and (a.) -80°C, (b.) 20°C and (c.) 80 °C (Boumbimba et al., 2017)

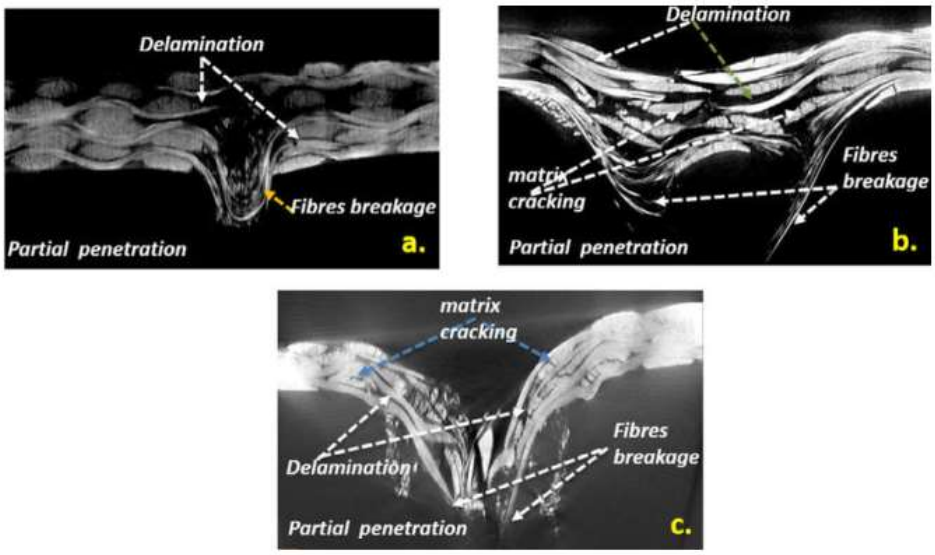

Figure 2.10 X-ray microtomography of damage behaviour in Acry_Nano10/GF at 40 J and (a.) -80°C, (b.) 20°C and (c.) 80 °C (Boumbimba et al., 2017)

(Dubary et al., 2017) used hybrid carbon and glass fibre woven PEEK laminates to investigate impact response at two different temperatures which were 20 °C and 150 °C. They found that the temperature had a large effect on the internal and external damage.

(Jia et al., 2018) studied the influence of temperature on the mechanical properties of CFRP using the three-point bending test integrated with an environmental chamber as shown in Figure 2.11. The experiments were performed under static and dynamic loads over the temperature range -100^{o}C to 100^{o}C. Experimental findings showed relatively poor performance when unidirectional laminated composite were tested at the high temperature, but that the mechanical properties (e.g. energy absorption, flexural strength and maximum deflection) were significantly enhanced at the lower temperature.

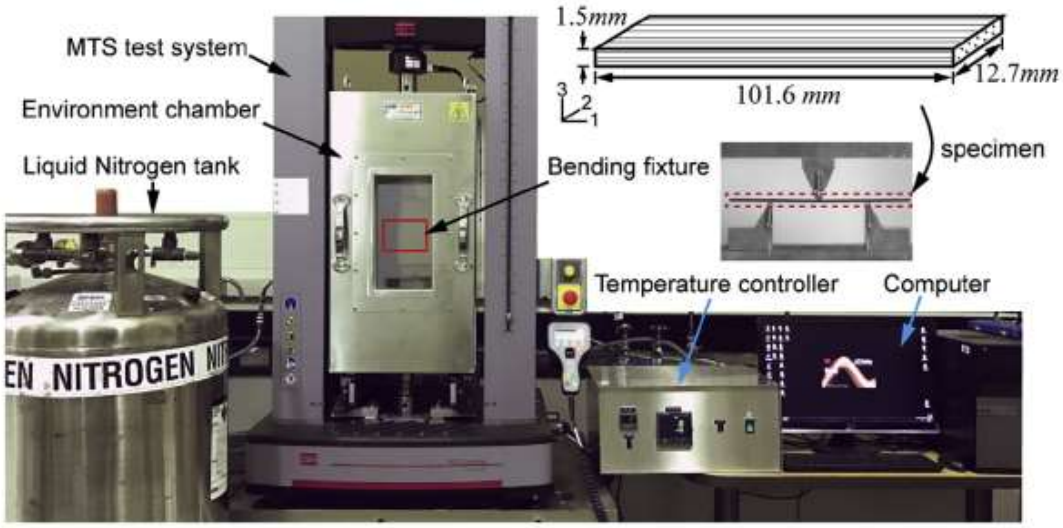

Figure 2.11 Electro-mechanical material experimental test integrated with an environmental chamber (Jia et al., 2018)

(Wang et al., 2018) performed an experimental investigation of the behaviour of woven carbon fabric/polyphenylene sulfide (CF/PPS) laminates impacted at room temperature and 95°C and 125°C. Macroscopic images of both side, front and back, of the specimen impacted at 15 J and 25 J are illustrated in Figure 2.12 and 2.13 respectively. At 95 °C, the intralaminar damage (matrix cracking) transformed partially from the glassy status to the rubber status. Therefore, the fibre breakage on the front side behaved in a ductile manner instead of brittle behaviour. At 125 °C, the matrix become softer and plastic deformation of the specimen was easily obtained. In general, the results showed that stiffness and degree of energy based damage for this material decreased with increase in temperature as the impact behaviour transformed from brittle to ductile.

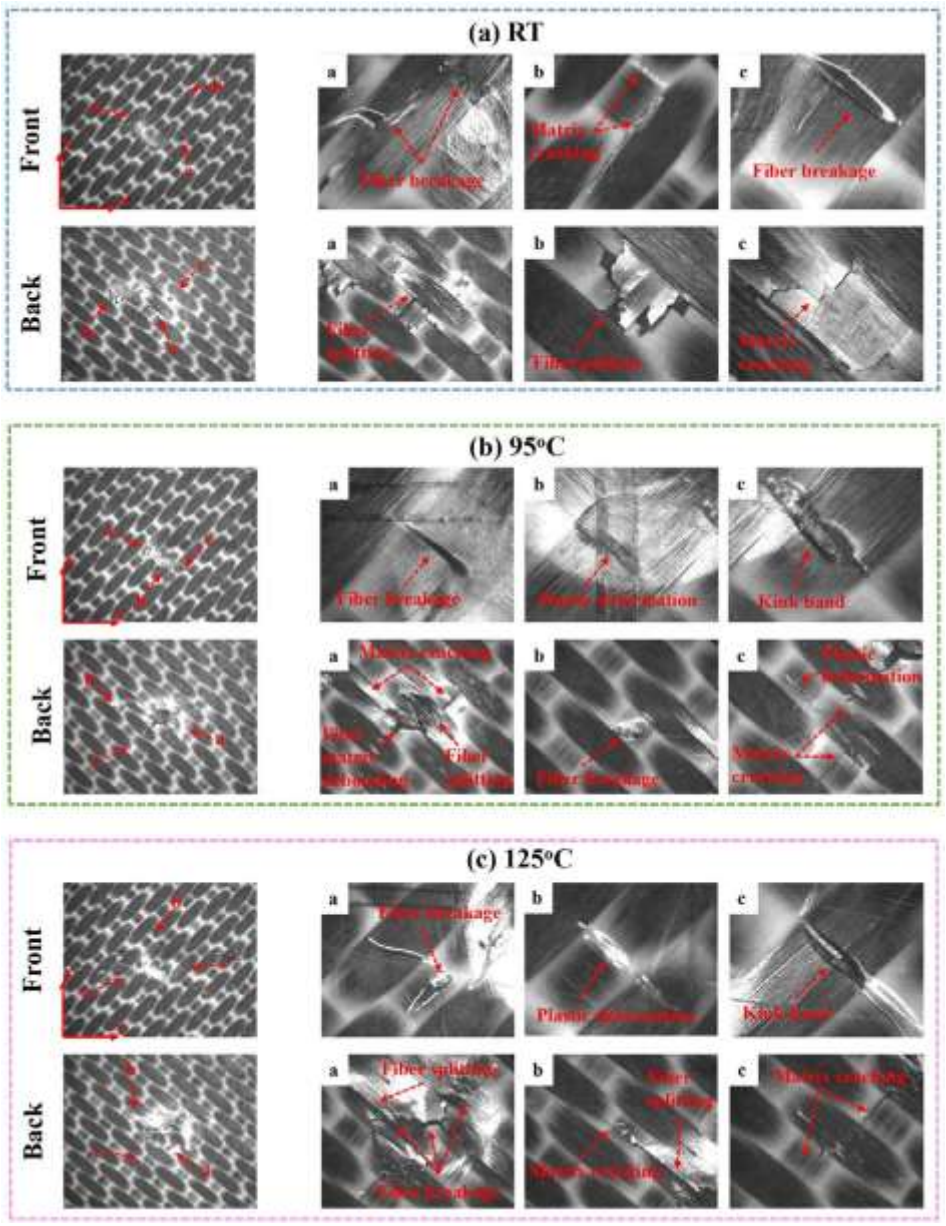

Figure 2.12 Macroscopic images of both side, front and back, of the specimen impacted at 15J (Wang et al., 2018)

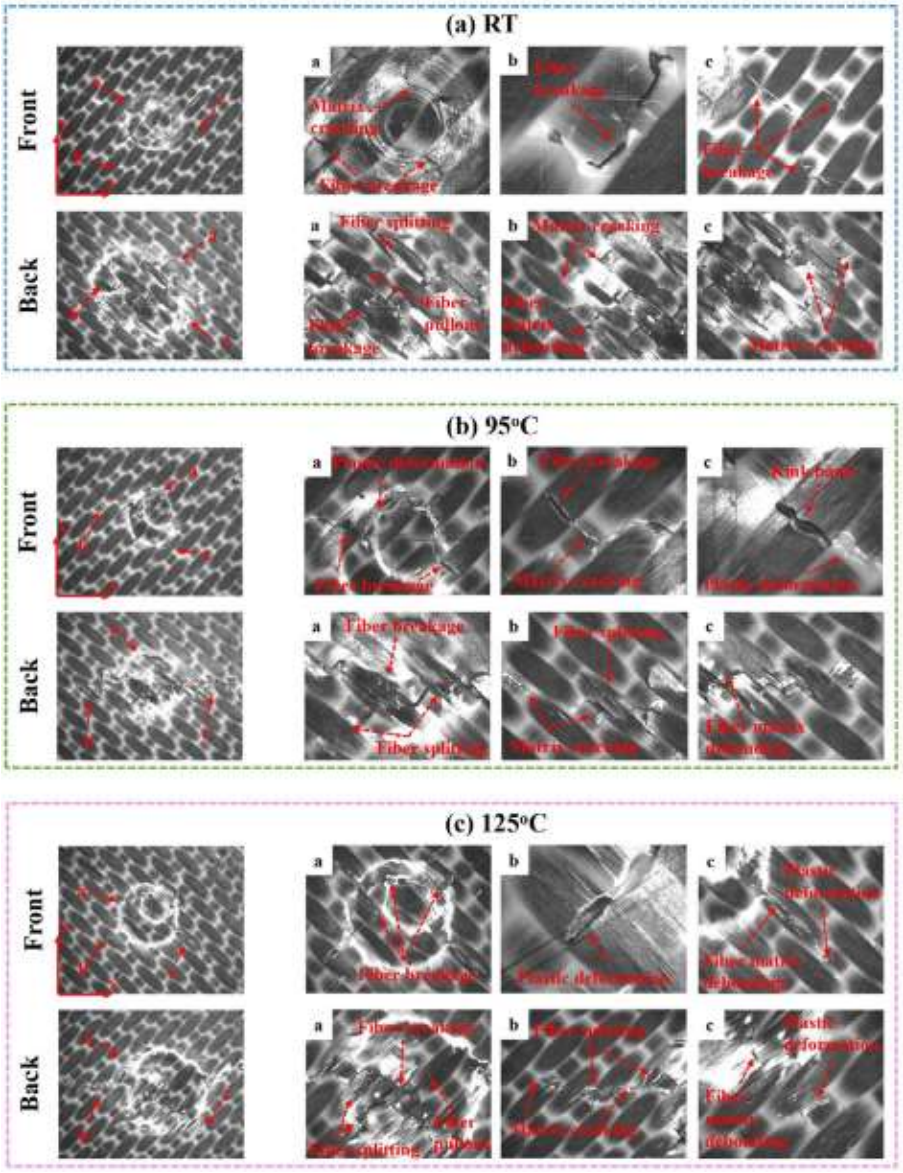

Figure 2.13 Macroscopic images of both sides, front and back, of the specimen impacted at 25J (Wang et al., 2018)

(Gong et al., 2022) studied the temperature influence on delamination propagation. Their tests were performed at three temperatures: 23°C, 80°C, and 130°C. The results showed the fracture toughness due to fibre bridging was largely insensitive to temperature in the range 23°C to 80°C, demonstrating a slight increase of 17.9%. However, in range of 80°C to 130°C, there was a large increase of 136.9% in fracture toughness. The bridging stress at 23°C was 100.48 KPa while it was 251.34 KPa at 130°C,

a substantial increase of 150.1%. Also, their results showed that the length of the fibre bridging zone significantly increased in the range of temperature 80^{o}C to 130^{o}C.

(Guo et al., 2022) investigated the influence of temperature variation on the plate-end debonding of fibre-reinforced polymer (FRP)-strengthened steel beams. They introduced an analytical solution based on a coupled mixed-mode cohesive zone model (CZM) to analyse the effect of thermal stress on the debonding failure of FRP-strengthened steel beams. Their results showed that the thermal stress is more significant for the response if a thicker and stiffer FRP plate is used.

2.2.1 Critical discussion

There are limitations when testing under different temperature conditions especially at low temperatures. The limitation is how to ensure the entire specimen reaches the same temperature before doing the test. A specimens needs around 20 min inside the chamber at -60 °C or 30 min at -150 °C, according to a thermal analysis carried out previously. Most researchers have not mentioned how long the specimen was in the climatic chamber before the test or how they ensured the thermal homogeneity of the specimen.

2.3 Fatigue loading

Fatigue-driven delamination in laminated composites is one of the general failure modes in composite structures e.g. airplanes, automobiles and wind turbines, all of which undergo cyclic loading (Bak et al., 2016). Fatigue is also a major contributor to failures in rotating machinery and has been addressed in many research works (Ibrahim and Albarbar 2011) and

(Ibrahim et al., 2013). Life estimation of composite materials is considered a serious challenge for engineers because of the uncertainties associated with damage initiation sites and propagation direction in these composites. There is a real and urgent need for reliable analytical methods to reduce the time and cost of experimental testing, and to enable optimally designed structures (Nojavan et al., 2016).

In composite structures, it is important to detect the damage at an early stage of failure and to know how the damage will grow during the service life of structures. A relationship between fatigue crack growth and stress intensity factor is generally written as a power law (i.e. the Paris law) for metals and composite materials (Vassilopoulos 2015).

Different approaches have been employed to analyse fatigue delamination growth, such as linear elastic fracture mechanics e.g. the virtual crack closure technique (VCCT), and cohesive zone models. Although the VCCT technique is widely used to simulate fatigue crack propagation, it has some limitations regarding crack path and re-meshing requirements. An alternative to the VCCT to simulate interface crack propagation, such as delamination in composite materials, is the cohesive zone model.

Over the last twenty years, many researchers have used finite element methods, including the cohesive zone model, rather than attempt analytical solutions to simulate crack growth

(Maiti and Geubelle 2005) introduced the instantaneous interface stiffness degradation law under cyclical fatigue loading. The rate of change of cohesive stiffness was defined as a function of the number of cycles. They proposed a power law for the cohesive model that can be expressed in

terms of discretized time steps. The instantaneous cohesive stiffness was assumed by (Serebrinsky and Ortiz 2005) to degrade exponentially with each unloading-reloading cycle.

Load envelope methods have been suggested by many researcher (Robinson et al., 2005), (Turon et al., 2007), (Tumino and Cappello 2007), (Moroni and Pirondi 2011), (Kawashita and Hallett 2012), (Landry and LaPlante 2012), and (Bak et al., 2017) to simulate fatigue damage growth based on experimental Paris law curves.

(Gornet and Ijaz 2011) investigated high-cyclic elastic fatigue damage model for carbon fibre epoxy matrix laminates. A classical interface damage was used to predict the fatigue damage parameters for different mode-mixtures.

(Nojavan et al., 2016) proposed a non-Paris law based fatigue cohesive zone model. The authors assumed a simple power law for fatigue delamination growth under pure Mode I and Mode II loading.

(Al-Azzawi et al., 2019) utilized a trapezoidal traction-separation law to describe the cohesive zone model in terms of elastic-plastic behaviour under high-cycle fatigue loading. Experimental tests on splice and doubler specimens, shown in Figure 2.14, manufactured from Glare® laminates were performed to validate the proposed damage fatigue model. The progressive fatigue damage accumulation obtained numerically by the authors under fatigue loading is illustrated in Figure 2.15. Their results showed that the doubler specimens had fatigue life higher than for splice specimens. They concluded that trapezoidal traction-separation was more

suitable for modelling delamination initiation and propagation than bilinear cohesive law.

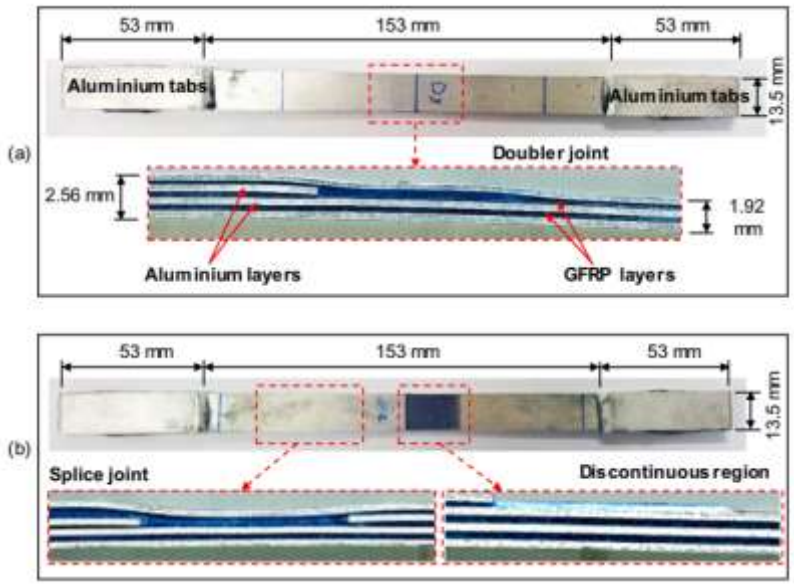

Figure 2.14 Specimen layout (a) doubler (b) splice (Al-Azzawi et al., 2019)

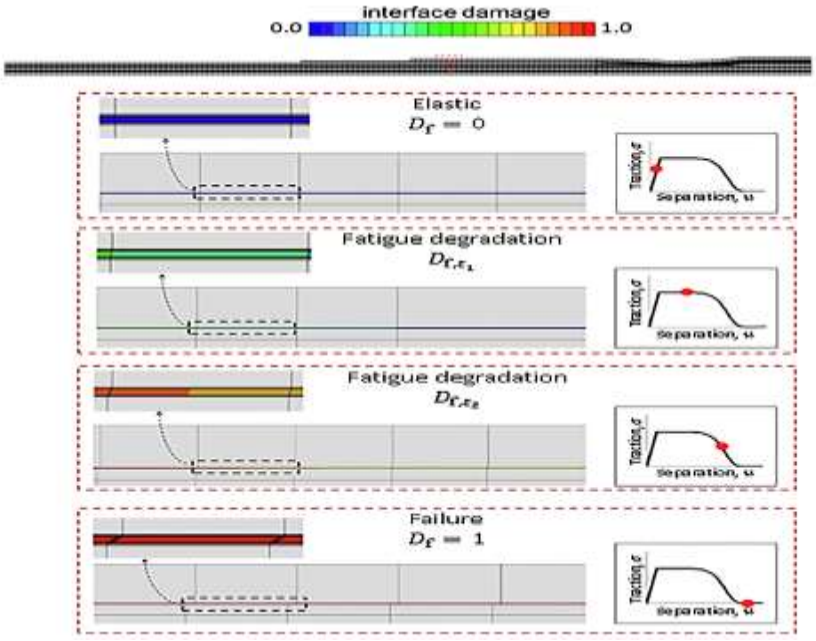

Figure 2.15 Fatigue damage accumulation (Al-Azzawi et al., 2019)

(de Oliveira and Donadon 2020) developed a virtual crack-tip integration point procedure based on the J-integral. Their method aimed to increase the accuracy of the estimation of the strain energy release rate during fatigue loading. The authors used the J-integral method to drive a fatigue

damage evolution law. They introduced a damage parameter related to the crack length as in Equation (2.1).

$$\frac{dD_A^f}{da_{el}^f} = \frac{1-D_A^{s,bf}}{l_{el}} - \frac{dD_A^{s,af}}{da_{el}^f} \tag{2.1}$$

Where $D_A^{s,bf}$ is static damage parameter before the fatigue loading. $D_A^{s,af}$ is damage accumulated after fatigue taken place. a_{el}^f is fatigue crack length. l_{el} is element length.

The proposed model was coded according to VUMAT and VEXTERNALDB subroutines that can be implemented in an explicit analysis using ABAQUS software.

The damage developing in the short fibre reinforced rubber sealing composites subjected to cyclic loading were investigated by (Yu et al., 2020) The specimen dimensions that were adopted by the authors are illustrated in Figure 2.14. The test was performed under different fibre mass fractions (2%, 5%, and 10%) at 1 MPa stress amplitude. Also, in this study, a low frequency of (0.1) Hz was adopted to avoid samples overheating. A fatigue damage model was used to predict the damage behaviour. The damage model is written as,

$$\frac{dD_f}{dn} = \alpha \left[\frac{\langle \frac{\sigma}{1-D_f} - \sigma_{th} \rangle}{\sigma_{th}} \right]^{\beta} \tag{2.2}$$

where α, β, and σ_{th} represent the material constants. D_f is the accumulated damage.

The traction-separation curve of the cohesive zone model at different fibre mass fractions for both experimental and simulation study is presented in Figures 2.15-2.17. From these figures, it is clearly seen that there was a difference between simulation and experimental results. The difference was clearly observed if the cycles were fewer than 1000 when the 2% fibre mass fraction was used, as shown in Figure 2.15. While when using 5% and 10% fibre mass fractions, the difference can be observed until nearly 4000 cycles, as illustrated in Figures 2.17 and 2.18.

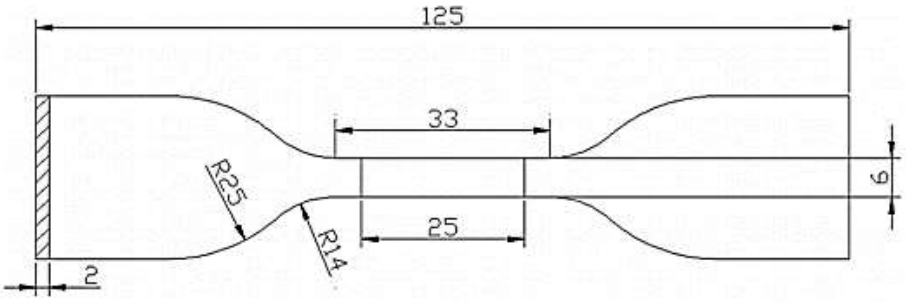

Figure 2.16 Specimen dimensions (Yu et al., 2020)

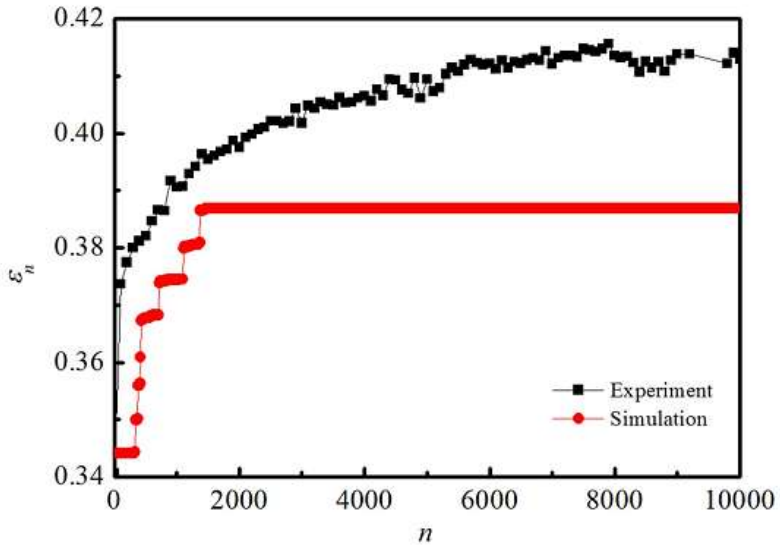

Figure 2.17 Traction-separation curve of cohesive zone model with 2% fibre mass fraction (Yu et al., 2020)

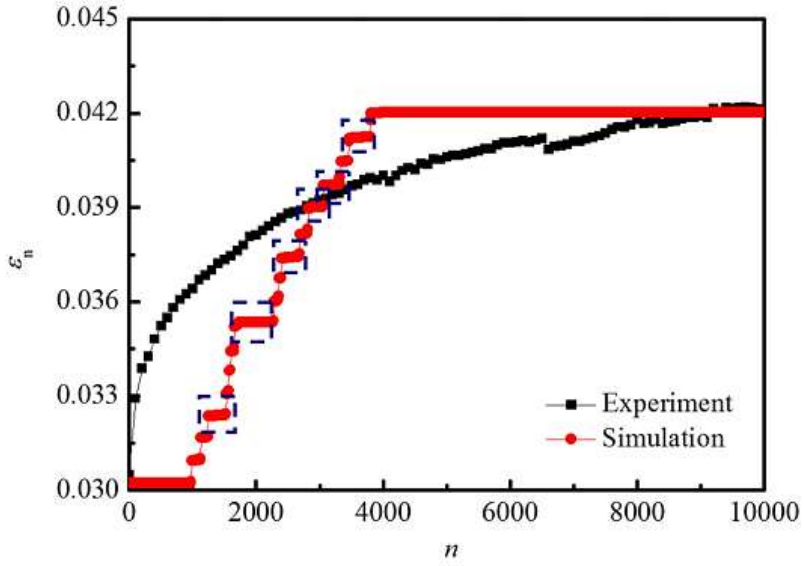

Figure 2.18 Traction-separation curve of cohesive zone model with 5% fibre mass fraction (Yu et al., 2020)

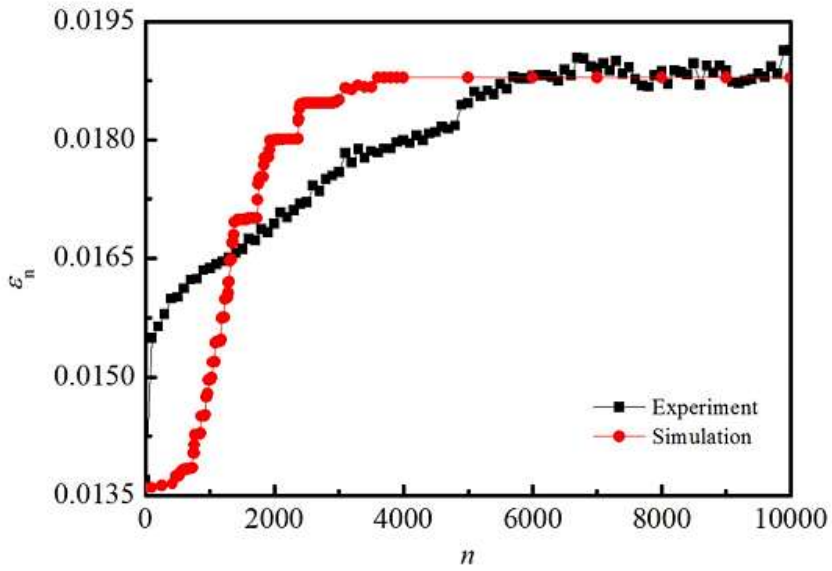

Figure 2.19 Traction-separation curve of cohesive zone model with 10% fibre mass fraction (Yu et al., 2020)

(Zhang et. al. 2022) used an artificial neural network to simulate cohesive zone models to predict fatigue-driven delamination growth in laminated composites. In their strategy, two twin cohesive elements were adopted to describe each segment of a composites interface and provide fracture mechanics parameters for a feedforward single-hidden-layer neural network. In this strategy the global load R ratio does not need to be known.

The neural network algorithm provides back again fatigue crack propagation rate to interface elements.

(Wang et al., 2022) presented cyclic cohesive zone model for fatigue crack growth considering the crack closure effect. They modified the damage evolution law to take into account the non-uniformity of the physical crack tip damage distribution. An adaptive cycle jump technique was used in their study to overcome the cycle-by-cycle calculation problems of the hysteresis damage models, and to reduce the computational cost.

(Eghbalpoor et al., 2023) investigated how cohesive properties change when subjected to low-cycle impact fatigue (LC-IF). End-notched flexure (ENF) specimens and single-lap joints (SLJs) were employed to generate pure shear and mixed mode impact loading conditions. A bilinear law was adopted to describe cohesive element and was implemented in ABAQUS using a user material subroutine (UMAT). Their results showed that adhesive's fracture energy and shear traction decrease with impact cycles.

2.3.1 Critical discussion

Some researchers used the trapezoidal traction-separation law to describe the cohesive zone model. But no comparisons were made in their articles which is a weakness in their studies. Others such as (Nojavan et al., 2016) introduced fatigue models of laminated composites. But although their proposed model can predict mixed mode delamination growth from simple parameters, their research demonstrated that the suggested cohesive zone model cannot be used for arbitrary damage onset and propagation. A crack path had to be pre-defined in order to arrange the elements along the crack path in the finite element model.

2.4 Intra-laminar damage

While composite laminates formally meet requirements, damage can be incurred due to foreign objects, e.g., heavy sand, birds, etc., impacting on the structure. All damage types start as unseen cracks and develop as one or more damage modes e.g., matrix cracking, fibre breakage, and/or delamination, all of which can lead to catastrophic failure of the structure (Zuo et al., 2018).

An impact load on the composite materials can be more dangerous than on metals components because the defect is undetectable by the naked eye. Investigations to assess the damage behaviour of composite structures subjected to impact loads are not a recent development. Composite structures used in aerospace and defence applications and, more recently, the issue of offshore wind blades have been examined by many researchers. The damage develops in the structures due to impact by an external object e.g. birds, or during installation when the wind blades are lifted from the ship or ground to the hub (Verma et al., 2019).

Numerical simulation is an effective tools to analyse fibre reinforced polymer composites, and computational simulation of intralaminar and interlaminar damage is considered a powerful and fast tool compared to experimental tests (Tarfaoui et al., 2017). Much research has been undertaken in this field, for example, the finite element analyses presented by (Turon et al., 2007), (Donadon et al., 2008), (Aymerich and Priolo 2008), (Yang et al., 2013), (Haselbach et al., 2016) and (Fagan et al., 2016) to investigate progressive damage modes.

(Liu et al., 2016) used various failure criteria, e.g. Puck, Hashin and Chang–Chang, to investigate how well they modelled dynamic progressive failure of laminated composites. Their investigation showed that, compared to the other two, the Puck criteria had some advantages when predicting failure, but was limited regarding accurate determination of the angle of the fracture plane. (Shor and Vaziri 2017) used the local cohesive zone (LCZ) method of progressive delamination in a large-scale laminated composite. Two dynamic models, axial crushing of tubes and transverse impact loading of plates, were investigated. Their results were compared to the conventional cohesive zone method and available experimental data. The results showed that the LCZ algorithm can adaptively split the structural elements through-thickness during the tubes axial crushing process.

(Namdar and Darendeliler 2017) investigated buckling, post-buckling and progressive failure of laminated plates numerically and experimentally. The 2D Hashin failure criteria was used to model intra-laminar damage in the laminated plates. The results indicated that the stacking sequence and the ply thickness affected the buckling, and failure progression.

(Tan et al., 2019) investigated the effect of matrix cracking on developing delamination in laminated composites. The extended finite element method (XFEM) and the Puck criteria were adopted by the authors to predict matrix cracking. Their findings showed that the matrix crack in the bottom layer contributed to narrow delamination in the region beneath the impact location.(Wu et al., 2020) studied the transverse low-velocity impact response and residual axial compression behaviour of braided composite tube. They carried out experimentally and numerically quasi-static axial

compression of intact and pre-damaged tubes. The effects of wall thickness on the mechanical response were investigated by these authors. The finite element model demonstrated that the proposed model has the capacity to capture damage variables due to transverse impact in the axial compression process.

(Jiang et al., 2020) used quasi-static and fatigue tests under various load conditions (stress levels) of cross-ply glass fibre reinforced plastic (GFRP) laminates. Their studies focused on the stiffness degradation curves and matrix damage evolution. It was observed that the fracture dimension evolution of transverse damage could be divided into three stages: (I) an initial slow rise, (II) a rapid rise, and (III) a final slow rise. (Sridharan and Pankow 2020) presented two progressive damage models and investigated them in the commercial finite element software; Abaqus/CAE and LS-Dyna. They used the VUMAT subroutine of the Abaqus/CAE and MAT 162 of LS-Dyna. Their study was carried out on composite laminates subject to both low velocity and high-velocity projectile. In general, the findings showed models are able to accurately predict the damage in the composite laminates subjected to either low and high velocities. Their results showed that Abaqus/CAE has good correlation with experimental test results for low velocity thicker laminates while MAT 162 can capture ballistic limits of high-velocity projectiles.

(Xia et al., 2022) introduced a three-dimensional damage model based on continuum damage mechanics (CDM) to analyse the damage and fracture in woven carbon fibre reinforced plastic laminates. A continuum damage model is presented to describe damage evolution in the composite

laminates with different ply orientations. Their proposed damage model can predict the matrix cracking (intralaminar) growth of woven fibre laminates under low velocity impact. The proposed damage model by those authors can predict the matrix damage of ply $[0]_8$ and $[45]_8$. So, the proposed method was more suitable for damage simulations of woven laminates with different ply orientations.

(Yuan et al., 2022) used a machine learning (ML) model to predict axial elastic modulus degradation of $[0_m/90_n]_s$ cross-ply laminates. They adopted an experimental data set available in the literature as well as finite element analysis (FEA) results. The ML accuracy depends on the reliability and amount of the data set, this may make ML model limited to apply on the other mechanical problems.

2.5 Identification of research gap

A literature review has confirmed that many researchers have experimentally investigated the effect of temperature on the behavioural response of laminated composites. However, very few studies have simulated damage under different thermal conditions. This study addresses that deficiency and presents a new approach of assessing incremental damage and takes into account thermal stress effects on delamination growth.

The literature has also shown that the previous research on fatigue damage in composite materials were largely experimental. Therefore, in this thesis, a developed damage model is presented by which to assess damage degradation under fatigue loading.

A damage degradation model and the incremental damage law under different load conditions (tension, compression, and shear) have been not fully numerically investigated, despite extensive computational simulation. Such a development is necessary to replace the time taken by experimental test and the associated costs. So, this study will present a developed model to assess damage degradation of matrix and fibres taking into consideration the load condition.

Chapter 3 : Cohesive zone model that includes thermal effects

The interface constitutive model without temperature dependency will be presented in this chapter. Prediction of onset of mixed mode softening and damage propagation prediction are also described. The thermal stress effect on the cohesive zone model will be derived in this section of the thesis.

3.1 Interface constitutive model without temperature dependency

Cohesive zone models are used to describe progressive damage in composite materials. Based on interfacial fracture mechanics, the fracture process zone ahead of a crack tip is illustrated as shown in Figure 3.1. In composite laminates the crack tip can be represented by a cohesive zone which depends on the separation displacement between two substrates. The required stress to resist this separation is determined as a function of the separation displacement using, for example, the bi-linear traction-separation constitutive law, see Figure 3.2, which is the most widely used to describe fracture behaviour in an interface element (Jousset and Rachik 2014).

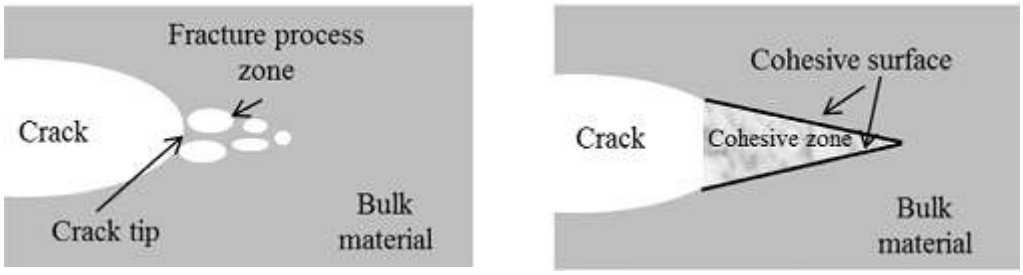

Figure 3.1 (a) Fracture process zone, and (b) Equivalent cohesive zone (Jousset and Rachik 2014)

The three active components of traction are Mode I, normal stress which is in a through thickness direction, and two shear tractions; Mode II and Mode III governed by separation displacement given by the traction-separation law. The elastic behaviour of the cohesive zone can be described as Equation 3.1;

$$\begin{bmatrix} \tau_n \\ \tau_s \\ \tau_t \end{bmatrix} = \begin{bmatrix} k_{nn} & 0 & 0 \\ 0 & k_{ss} & 0 \\ 0 & 0 & k_{tt} \end{bmatrix} \begin{bmatrix} \delta_n \\ \delta_s \\ \delta_t \end{bmatrix} \tag{3.1}$$

where τ_n , τ_s , τ_t are the normal, shear and tear stresses respectively, and δ and *k* are the separation displacement and the initial stiffness of the interface of each mode, respectively.

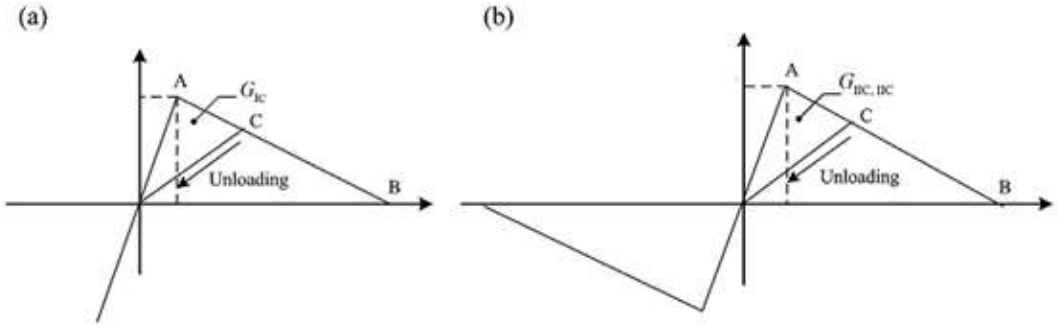

δ

Figure 3.2 Bi-linear traction-separation law under tension and compression (a) Mode I and (b) Mode II (Zhang et al., 2017)

As shown in Figure 3.3, the bi-linear traction-separation law under typical pure modes initially assumes a linear elastic behaviour followed by the initiation and evolution of damage. The softening initiation displacements are calculated as:

$$\delta_n^0 = {}^{\tau_{nc}}/_{k_{nn}}, \quad \delta_s^0 = {}^{\tau_{sc}}/_{k_{ss}}, \quad \delta_t^0 = {}^{\tau_{tc}}/_{k_{tt}}$$

The final separation or complete debonding is defined as:

$$\delta_n^{\mathrm{f}} = \frac{2G_{IC}}{\tau_{nc}}, \quad \delta_s^{\mathrm{f}} = \frac{2G_{IIC}}{\tau_{sc}}, \quad \delta_t^{\mathrm{f}} = \frac{2G_{IIIC}}{\tau_{tc}}$$

where G_{IC}, G_{IIC} and G_{IIIC} are the critical fracture energies of Modes I, II and III.

3.2 Prediction of onset of mixed mode softening

The damage onset of the cohesive element under pure Mode I, II or III loading, can be determined in a straightforward manner using a maximum traction stress criterion for each mode, obtained by comparing the traction components with allowable stress. However, when using this criterion to

determine damage onset under mixed-mode loading poor results are obtained, because softening behaviour may appear before any stress components. Therefore, the interactions between stress components of each mode should be taken into account to determine initiation of delamination damage.

The quadratic nominal stress criterion to predict the delamination onset under mixed mode loading, is one of the most frequently adopted failure criteria (Camanho et al., 2003),(Zou and Lee 2017). This criterion has been successfully utilized by many researchers, and is written as:

$$\left(\frac{\langle \tau_n \rangle}{\tau_{nc}}\right)^2 + \left(\frac{\tau_s}{\tau_{sc}}\right)^2 + \left(\frac{\tau_t}{\tau_{tc}}\right)^2 \geq 1 \tag{3.2}$$

Figure 3.3 illustrates the mixed-mode bi-linear traction-separation law for the interface element. The effective relative displacement, δ_m, is defined as:

$$\delta_m = \sqrt{\langle \delta_n \rangle^2 + \delta_s^2 + \delta_t^2} \tag{3.3}$$

Equation 3.3 can also be written as:

$$\delta_m = \sqrt{\langle \delta_n \rangle^2 + \delta_{shear}^2} \qquad \text{(where } \delta_{shear}^2 = \delta_s^2 + \delta_t^2 \text{)} \tag{3.4}$$

where the operator $\langle x \rangle$ is defined as:

$$\langle x \rangle = \begin{cases} x, & x > 0 \\ 0, & x \leq 0 \end{cases} \tag{3.5}$$

Using the same interface stiffness for Modes I, II and III and a quadratic nominal stress criterion, the onset of softening displacement under tension mixed-mode conditions ($\delta_1 > 0$), is obtained as (Zhang et al., 2017):

$$\delta_m^0 = \delta_1^0 \delta_{shear}^0 \sqrt{\frac{1-(\delta_{shear}/\delta_1)^2}{\left(\delta_{shear}^0\right)^2 + (\delta_{shear}/\delta_1)^2 \left(\delta_1^0\right)^2}} \qquad \delta_1 > 0 \tag{3.6}$$

In Equation (3.6), the pure Mode I can be obtained by setting $\delta_{shear}/\delta_1 = 0$, (i.e., $\delta_m^0 = \delta_1^0$). The mixed-mode is reduced to the shear model when the shear displacement (δ_{shear}) is much larger than the normal displacement, i.e. $\delta_{shear}/\delta_1 \Rightarrow \infty$.

When the cohesive zone undergoes a through-thickness compression, the stiffness degradation of the interface element will occur only in a shear mode (Mode II or Mode III), whereas there is no damage initiation and propagation of Mode I. Therefore, the onset of damage under mixed a mode occurs if $\delta_1 < 0$ is δ_{shear}^0.

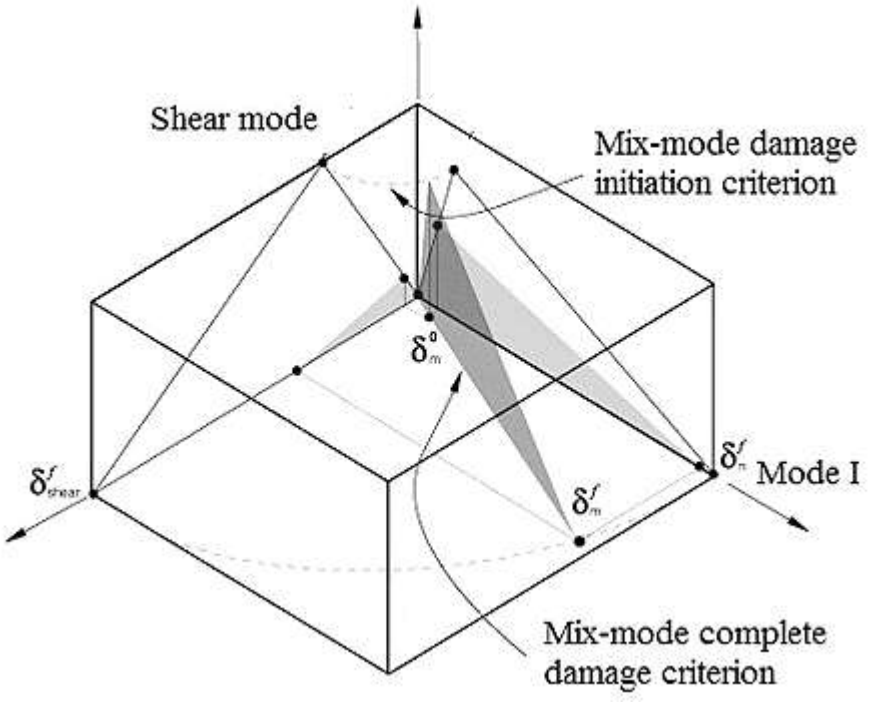

Figure 3.3 Mixed-mode bi-linear traction-separation law of interface element (Camanho et al., 2003)

3.2 Damage propagation prediction

Damage growth prediction under mixed-mode loading is predicted using the energy release rate during loading and unloading, and fracture toughness.

The power law criterion is most widely used to predict damage growth under mixed-mode loading. This criteria is based on the concept of interaction between the energy release rates (Camanho et al., 2003), (Zou and Hameed 2018) and is written as:

$$\left(\frac{G_I}{G_{IC}}\right)^{\alpha} + \left(\frac{G_{II}}{G_{IIC}}\right)^{\alpha} \geq 1 \tag{3.7}$$

The effective displacement at complete failure (δ_m^f) of a mixed mode is obtained based on a quadratic nominal stress criterion and the power-energy interaction law (Equation 3.7). Therefore, the final displacement of a mixed-mode under tension ($\delta_1 > 0$) is expressed as:

$$\delta_m^f = \frac{2(1+(\delta_{shear}/\delta_1)^2)/k\ \delta_m^0}{\sqrt{(1/G_{IC})^2+((\delta_{shear}/\delta_1)^2/G_{IIC})^2}} \tag{3.8}$$

Under through-thickness compression ($\delta_1 < 0$), the effective displacement at complete failure (δ_m^f) is:

$$\delta_m^f = \sqrt{\left(\delta_2^f\right)^2 + \left(\delta_3^f\right)^2} \tag{3.9}$$

3.2 Thermal stress effect

When a mechanical force acts on composite materials concurrent with a temperature change, the nominal strain contribution due to the temperature change should be added to the nominal strain due to the internal stress. An incremental damage evolution law will be developed to take into

consideration the mechanical effects of change in temperature of an interface element. Based on the Helmholtz free energy density, the free potential energy (ψ) is a function of the cohesive zone displacements, evolution of damage, and the effect of temperature across the interface (ΔT), and can be written as:

$$\psi(\delta_i, D, \Delta T) = \frac{1}{2}(1-D)k_i(\delta_i - \alpha\Delta T)^2 \quad (3.10)$$

where α is thermal expansion coefficient, and *D* is damage parameter which is calculated as:

$$D = \frac{\delta_m^f(\delta_m - \delta_m^o)}{\delta_m\left(\delta_m^f - \delta_m^o\right)} \quad (3.11)$$

The traction components are obtained by differentiating the potential energy relative to interface displacement as:

$$\tau_i = \frac{\partial\psi}{\partial\delta_i} = (1-D)k_i(\delta_i - \alpha\Delta T) \quad (3.12)$$

and the thermodynamic conjugate force is derived relative to the damage variable (D);

$$\mathbb{C} = -\frac{\partial\psi}{\partial D} = \frac{1}{2}k_i(\delta_i - \alpha\Delta T)^2 \quad (3.13)$$

The damage function is defined as:

$$\mathcal{F}(\mathbb{C}, D) = \mathbb{C} - \mathcal{R}(D) \quad (3.14)$$

The function $\mathcal{R}(D)$ is the resistance to the crack propagation and written as:

$$\mathcal{R}(D) = \frac{1}{2}(1-D)k_i(\delta_i - \alpha\Delta T)^2 \quad (3.15)$$

The incremental damage evolution law is calculated using the consistency condition $\dot{\mathcal{F}} = 0$:

$$\frac{\partial \mathbb{C}}{\partial \delta_i} \partial \delta_i - \frac{\partial \mathcal{R}(D)}{\partial D} \partial D = 0 \tag{3.16}$$

Therefore, the new incremental damage including the effect of temperature change is given by:

$$\partial D = \frac{\sum_{i=1}^{3} k_i (\delta_i - \alpha \Delta T)}{\sum_{i=1}^{3} \frac{1}{2} k_i (\delta_i - \alpha \Delta T)^2} \partial \delta_i \tag{3.17}$$

3.3 Results and discussion

3.3.1 Three-point bending specimen

(Jia et al., 2018) carried out static three-point bending tests on high strength carbon fibre reinforced plastic using MTS mechanical tests with a 1 kN load cell. The tests were performed on specimens with length along the longitudinal fibre of 101.6 mm, 12.7 mm across the specimen and height of 1.5 mm, see Figure 3.4. The material properties of high strength carbon fibre-reinforced polymer at room temperature are listed in Table 3.1.

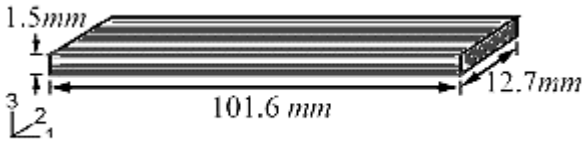

Figure 3.4 Specimen dimensions (Jia et al., 2018)

Table 3-1 The material properties of high strength carbon fibre-reinforced polymer (Jia et al., 2018)

Modulus (Pa)	227×10^9
Tensile strength (Pa)	2.8×10^9
Poisson's ratio	0.3
Elongation at failure	1.4%
Linear thermal expansion coefficient	4×10^{-6}

(Jia et al., 2018) performed mechanical experiments over a temperature range from 60^{o}C to -60^{o}C in an environmental chamber with temperature accurate to ±1^{o}C. Five specimens were examined and held for 20 minutes in the chamber to reach a uniform temperature prior to the experimental tests. A quasi-static test was conducted on all specimens with a constant strain rate of 0.01 s^{-1}, at the middle of the span along the specimen's length. The force-displacement responses of the three-point bending tests conducted at the various temperatures were measured. These results are used below to validate the predictions of the model being developed.

3.3.1.1 Numerical simulation

In this section, the experimental tests of (Jia et al., 2018) are simulated to validate the new incremental damage evolution law for interface elements. The incremental damage model developed was implemented in ABAQUS/Standard software using a user-defined material model via the UMAT subroutine.

The specimen was divided into two sub-laminates, each 0.75 mm thick, and connected to each other by a cohesive element via a 'Tie' interaction. An interface stiffness of $1x10^{14}$ N/m^3 was used in the simulation. The material properties of the interface element are presented in Table 3-2. The element type adopted for the layers was the 4-node bilinear, CPS4, and for the adhesive layer the 4-node cohesive element COH2D4 was used. A mesh independence/convergence study is presented to select the suitable mesh grid size. The failure load was computed over a range of mesh sizes: 0.07, 0.08, 0.09, 0.1, 0.2, and 0.3 mm. The mesh sizes less than or equal to 0.1 mm gave the same failure load, but when the mesh size was equal to or

large than 0.2 mm there was a drop in the failure load as shown in Figure 3.5. Therefore, the mesh size of 0.1 mm was adopted for all elements. The finite element model showing the loading and boundary conditions using ABAQUS software is illustrated in Figure 3.6. Stress contour of three-point bending specimen is presented in Figure 3.7, it is observed that the tension stress occurs at the lower surface while the compression stress appears at the upper surface. The deformation contour of the three-point bending specimen is shown in Figure 3.8, the displacement of the left end (red) is in a positive direction (+x) while the right end (blue) of specimen is in a negative direction (-x).

Table 3-2Material properties of the interface element (Shi et al., 2012)

τ_{nc} (MPa)	$\tau_{sc} = \tau_{tc}$ (MPa)	G_{IC} (J/m^2)	$G_{IIC} = G_{IIIC}$ (J/m^2)
62.3	92.3	280	790

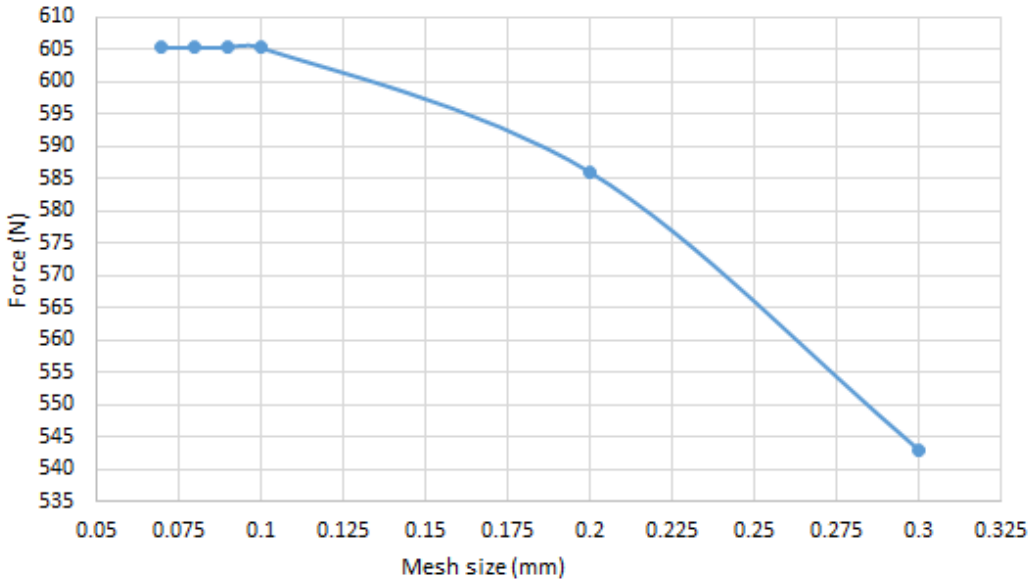

Figure 3.5 A mesh independence/convergence study

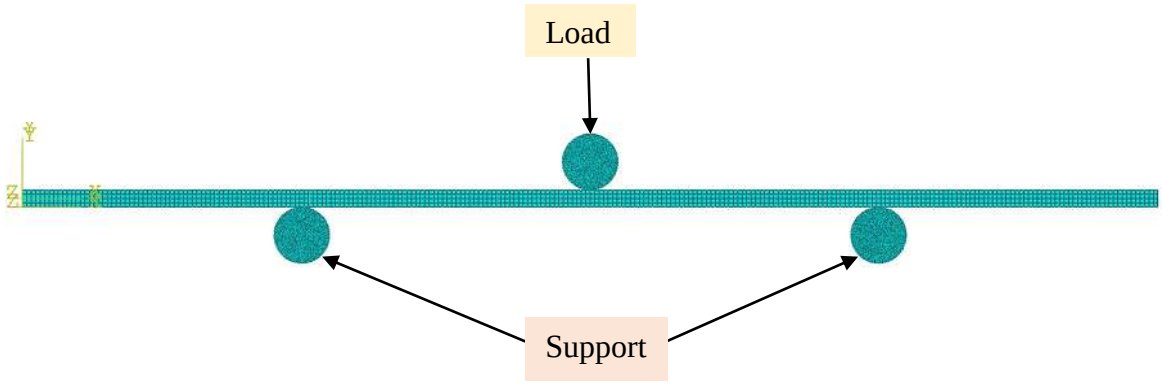

Figure 3.6 Finite element model of three-point bending specimen

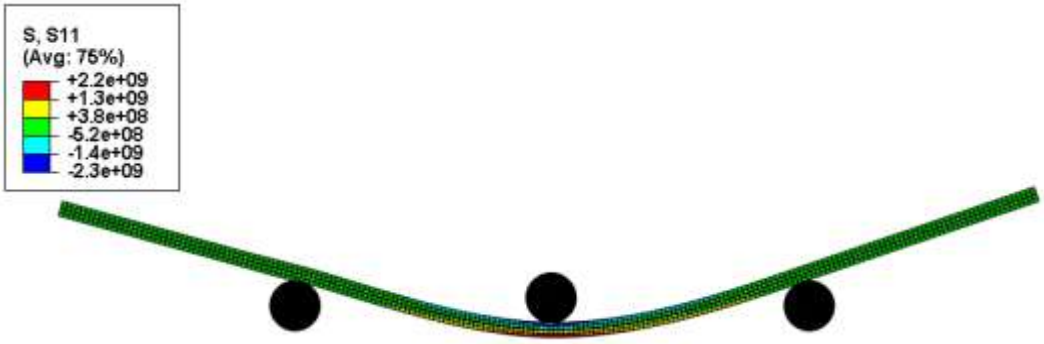

Figure 3.7 Stress contour of three-point bending specimen

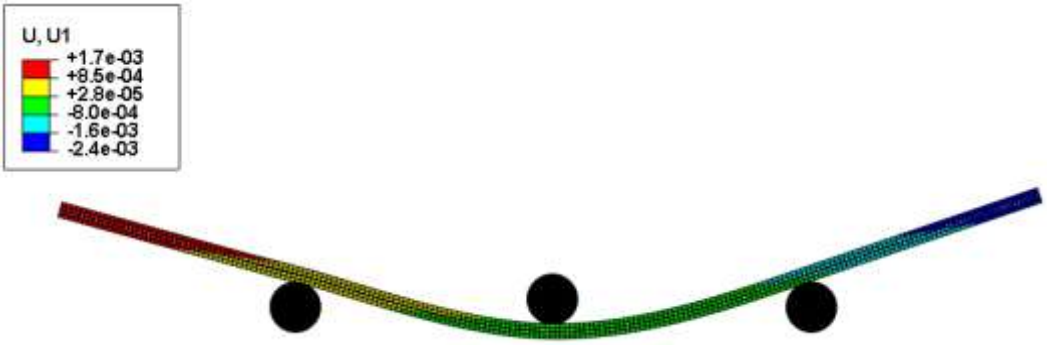

Figure 3.8 Deformation contour of three-point bending specimen

When the specimen was tested under different temperature conditions, the total traction stress of the interface element was a combination of thermal stress and normal /shear stress for each mode. The damage initiation stress was updated based on; $\tau_{inew} = \tau_i - \tau_{thermal}$, , and $\tau_{thermal} = k\alpha\Delta T$. Thus if the temperature changed resulting in a change in traction stress, the fracture energy was also affected.

Figure 3.9 is a schematic of the bilinear traction separation law at low and room temperature. It is clear that the traction at onset of damage increased when the specimen was at a low temperature. The fracture energy increased by $\Delta G = \frac{1}{2}\delta^f \delta^c \left[\left(\frac{\tau_c^{new}}{\tau_c}\right)^2 - 1\right]$.

In addition, the damage initiation displacement and final failure displacement increased to $\delta_{new}^c = (\tau_c^{new}/\tau_c)\,\delta^c$, and $\delta_{new}^f = (\tau_c^{new}/\tau_c)\,\delta^f$, respectively. The energy absorption is the area below the traction-separation curve. Thus, according to the traction separation law the energy absorbed is less at a higher temperature due to the cohesive behaviour. This is shown as ΔG in the figure.

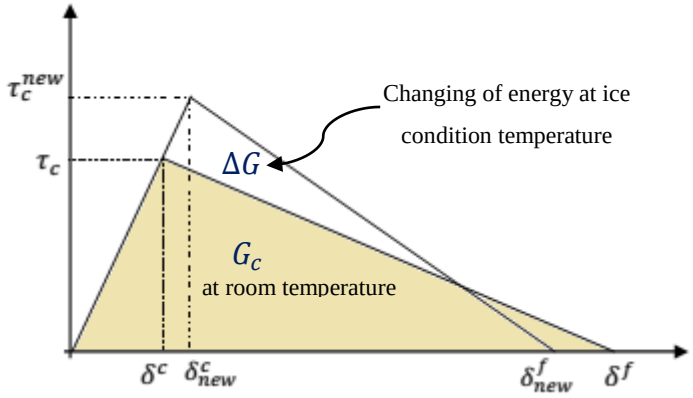

Figure 3.9 Schematic traction-separation law

Figure 3.10 shows the force-displacement curves for all the specimens under three different thermal conditions (60^0C, -20^0C and -60^0C). It can clearly be observed that the load-displacement response behaviour using this new approach is similar to the experimental data and both sets of curves have a linear elastic section followed by a force drop. There was some deviation between experimental data and proposed model especially when the displacement was less than 4mm. However, the deviation decreases

when the displacement is larger than 4 mm. This deviation occurs due to the interface stiffness value, which should be carefully chosen to overcome convergence problems in the numerical solution.

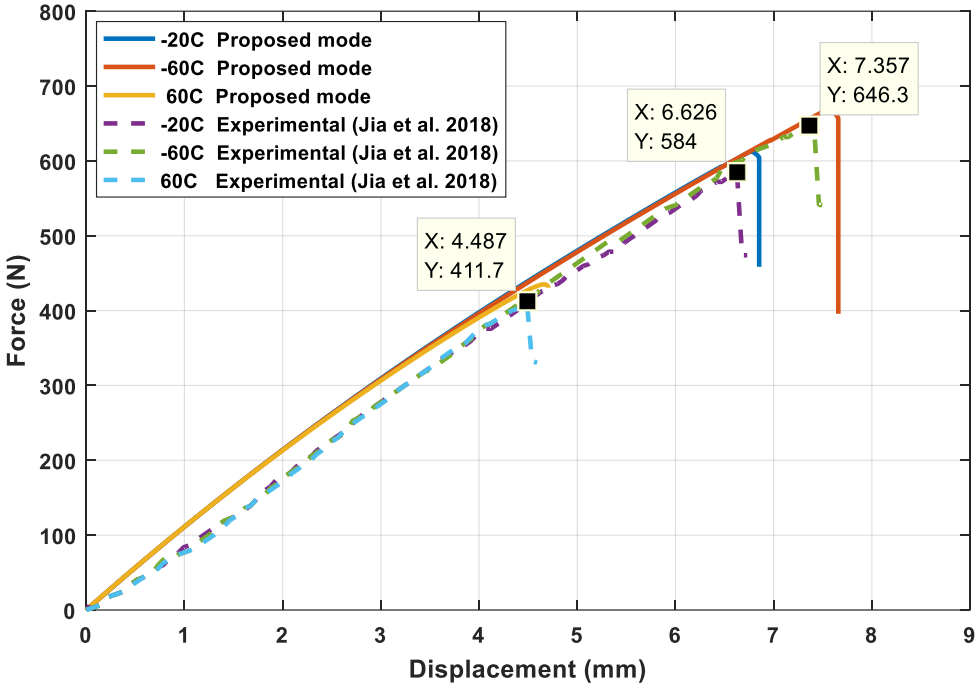

Figure 3.10 Force-displacement curve of three-point bending specimen

3.3.2 Double cantilever beam (DCB)

Inter-laminar damage in composite structures is a frequent failure mode which has a significant effect on strength, stiffness and structural integrity. Thus, the understanding of resistance to delamination fracture in composite materials is particularly important. The critical fracture energy of Mode I can be measured experimentally using a double cantilever beam (DCB). This energy will change when the composite material is subjected to different environmental conditions, i.e., different temperatures.

Many researchers have experimentally measured fracture toughness of unidirectional laminated composites at room and other temperatures, but temperature effects on inter-laminar damage have not been fully investigated numerically.

(Kim, 1999) investigated the fracture energy of Carbon/Epoxy composites at -100^{o}C, room temperature and 150°C, using a DCB with pre-cracked interface, [0_{12}//0_{12}]. Figure 3.11 is a schematic of the DCB specimen, showing dimensions and delamination between sub-laminates. The authors performed the tests using a servo-hydraulic machine to provide displacement control, and a thermostatic chamber which could accurately maintain the temperature at any temperature between -180°C and 320°C. The specimens were kept for one hour in the thermostatic chamber to reach a homogeneous distribution of temperature before the tensile testing.

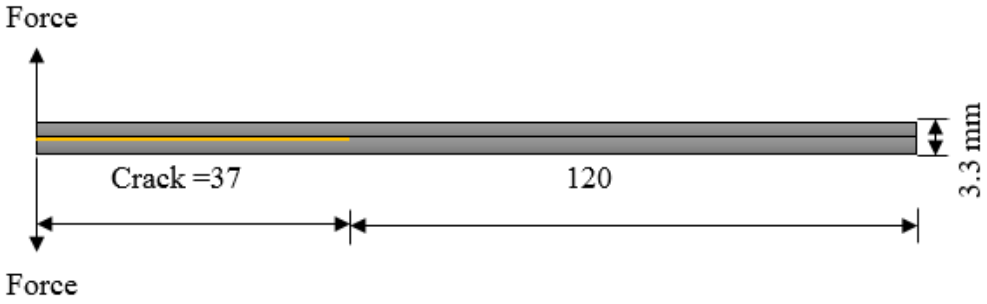

Figure 3.11 DCB specimen dimensions

The morphologies of the fracture surface when using the DCB specimen type [0//0] were reported by (Kim, 1999), and are shown in Figure 3.12. It is clearly seen that at cryogenic temperatures, the fibre breakage and fibre bridging happened at onset and propagation of damage. When the specimens were examined at a temperature higher than room temperature, the damage started in the matrix was followed by fibre bridging. Therefore, the failure occurred at a smaller fracture energy because the matrix critical energy is relatively low. This explains why the fracture toughness at room temperatures is lower than at cryogenic temperatures.

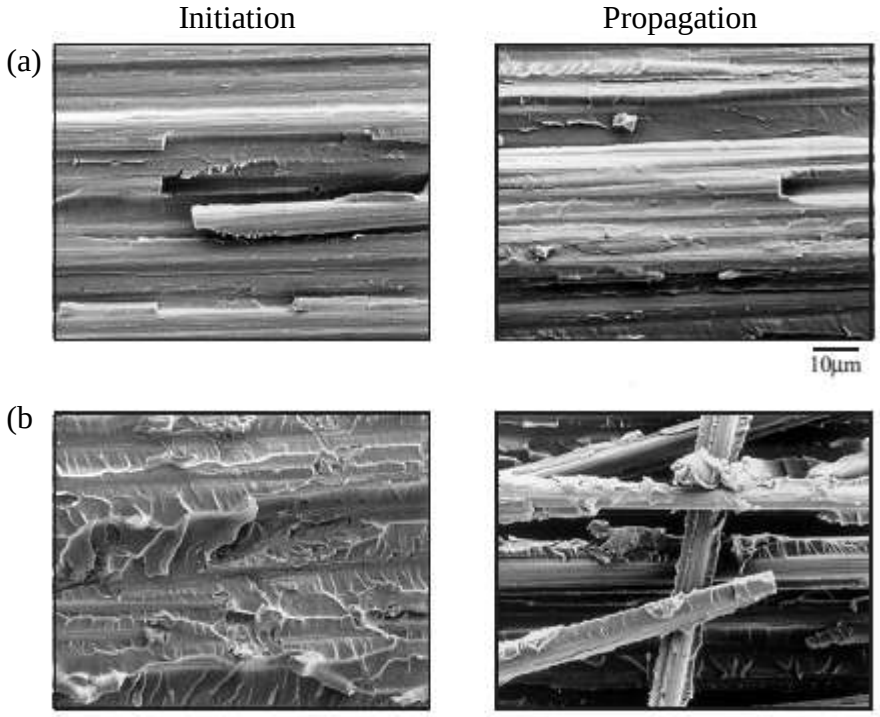

Figure 3.12 Images of fracture surfaces for unidirectional specimen (Kim HS 1999)

In the simulation model, the new approach was applied to investigate fracture energy and response behaviour of DCB at various temperatures. The numerical model was built in ABAQUS and again used element type COH2D4 for the interface elements, and element type CPS4 for the sub-laminates, both types had element size 0.1 mm. The interface stiffness used in the modelling was 1×10^{14} N/m^3.

Sensitivity analysis is introduced in this section to illustrate the impact of variation of key inputs to the output/response. Three different shear stresses of cohesive element 10, 20, and 30 MPa have been adopted to investigate the response of the developed analytical models. In addition, various fracture energy 90, 180, and 360 J/m^2 have been used to make sure the numerical model is sensitive to input parameters. Figures 3.13 and 3.14 illustrate the force-displacement response under different parameters. It is

clearly seen from these figures that the output/response of the analytical model has good sensitivity to the inputs.

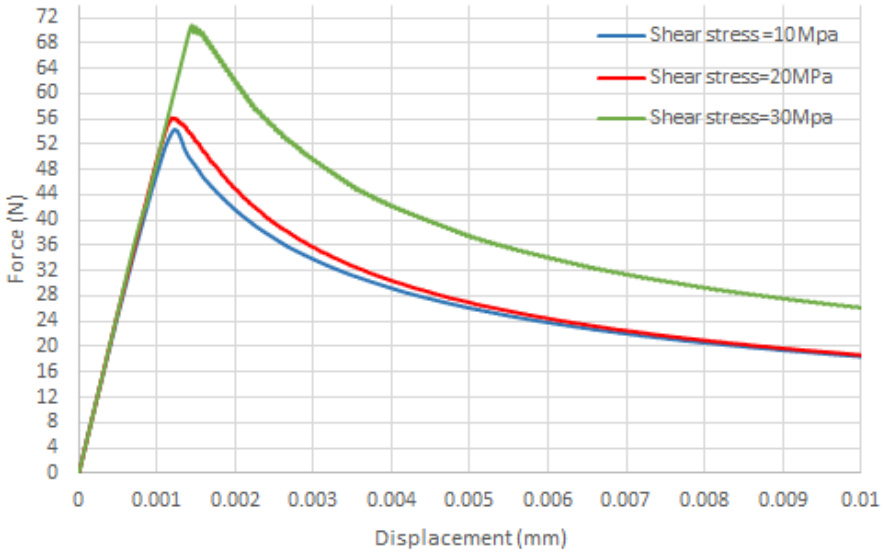

Figure 3.13 Force-displacement curve under different shear stresses

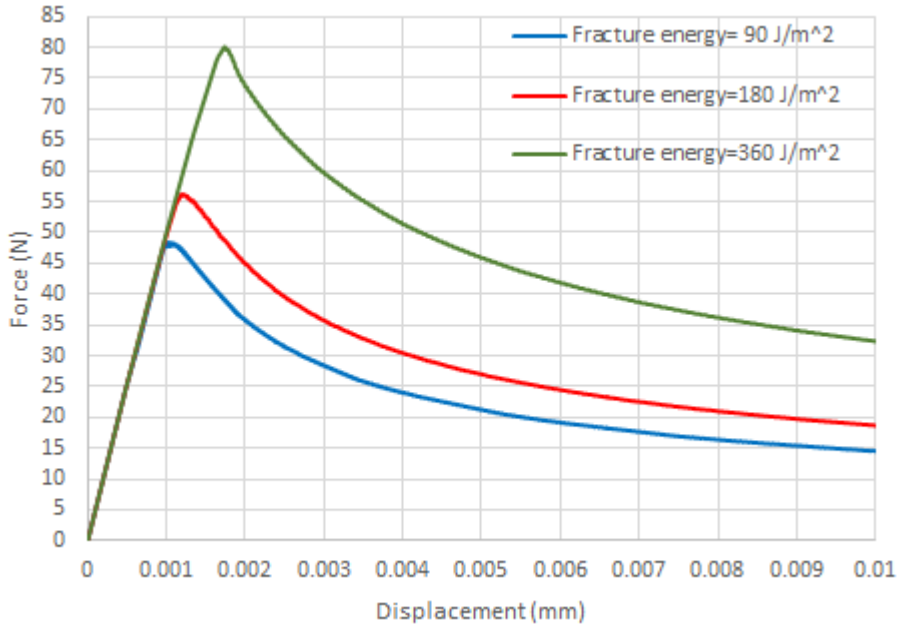

Figure 3.14 Force-displacement curve under different fracture energies

The force-displacement curves obtained for high (150^{o}C) and low (-100^{o}C) temperatures are presented in Figures 3.15 and 3.16. It was recognized that the change in temperature had a noticeable effect on damage initiation and propagation. The predicted force required for failure in the unidirectional specimen at the higher temperature was 52 N, less than the 60 N required

at the lower temperature. At 150°C, the predicted displacement at which the peak force occurs is very close to the measured value; both 1.6 mm. The predicted results compared well with Kim's measured data.

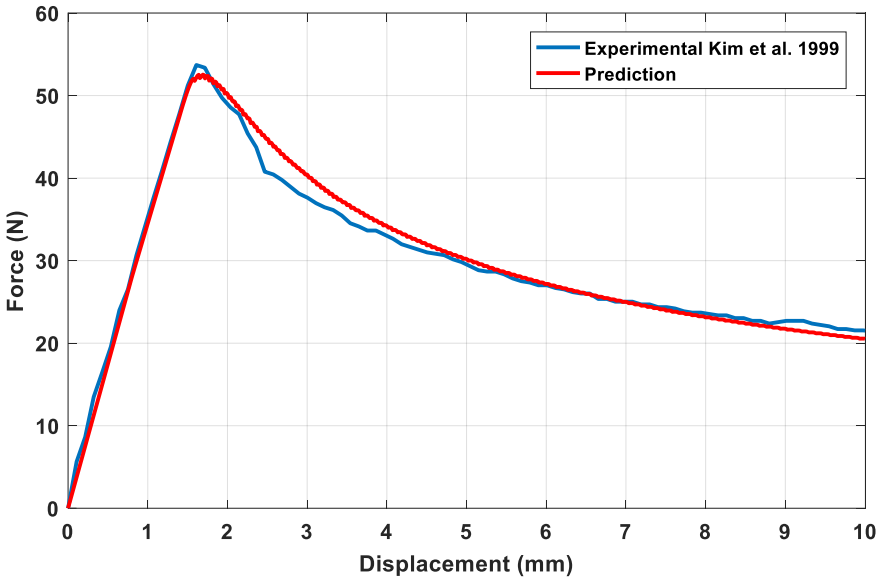

Figure 3.15 Force-displacement curve at high temperature (150°C)

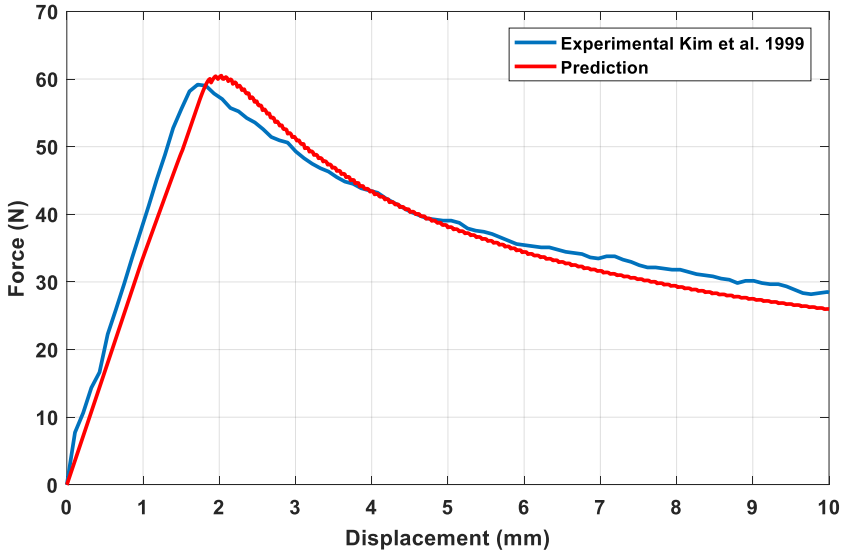

Figure 3.16 Force-displacement curve at low temperature (-100°C)

The displacement peaks move in the same direction as the temperature decreases to -100°C, and agreement remains good: 2.0 mm for the predicted and 1.75 mm for the measured. We see that predicted values and

experimental results reported by (Kim 1999) are in good agreement. The deviation between experimental data and proposed model is explained in the previous section (Numerical simulation). In addition, in the softening region, which starts after initiation damage, a loss in the stiffness occurs which leads to instability of the specimen which affects the collected data.

3.4 Summary

This chapter presents a cohesive zone model combining mechanical and thermal effects. Thermal stress was added to the Helmholtz free energy density in order to derive a new approach to incremental damage, which included the effect of temperature. The developed damage model has been implemented in ABAQUS using the UMAT subroutine and applied of two different specimens: a three-point bending specimen and a Double Cantilever Beam. The effectiveness of the new method was tested for the given specimens at different temperatures. The simulation results revealed that the total energy of the interface element of high strength carbon fibre reinforced plastic increased as its temperature decreased. It is demonstrated that the load-displacement curves obtained from the numerical model for both test specimens were in good agreement with experimental data available in literature. In this chapter, the cohesive zone model was investigated under static load. The effect of dynamic load on the cohesive zone will be described in the next chapter.

Chapter 4 : Progressive failure mechanism of laminated composites under fatigue loading

This chapter introduces the change in strain energy rate and the total damage parameter during cyclic loading. New damage evaluation and the rate of fatigue damage for each cyclic loading ($\partial D/\partial N$) will also be presented in this chapter. The Double Cantilever Beam (DCB) and Single Lap Joint (SLJ) Model has been adopted to validate the new approach.

4.1 Fatigue loading

Composite structures can be subject to cyclic loads with different wave shapes such as sinusoidal, square, etc. The load fluctuates with a certain frequency (fn) with a constant amplitude and produces a periodical stress or strain. Figure 4.1 shows typical sinusoidal and square loading curves with relevant parameters i.e., average stress is ((σ_{max}+σ_{min})/2), stress amplitude is ((σ_{max}-σ_{min})/2), and R-ratio (σ_{min}/σ_{max}). High amplitudes of fatigue loading reduce the remaining life of the structure (Kiefer, 2014).

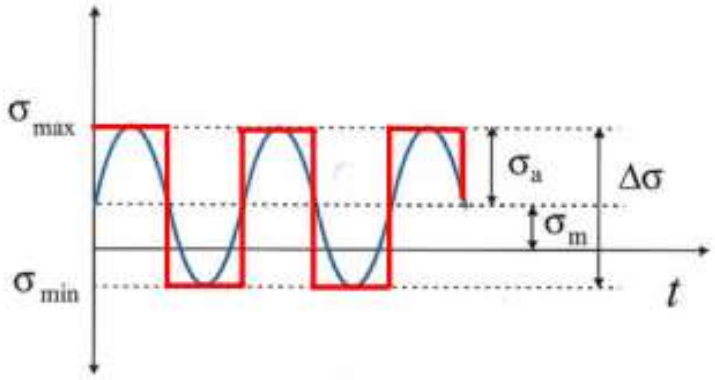

Figure 4.1 Sinusoidal and square stress functions

In fracture mechanics, the crack growth rate depends on the stress intensity factor or the energy release rate, and propagates according to the Paris law. In the last few years many researchers have introduced algorithms into the cohesive zone model which include fatigue damage degradation. (Belnoue et al., 2016) employed the Paris law to represent fatigue in an interface element based on change in strain energy release rate, ΔG. The crack growth rate, $\partial a/\partial N$, was assumed to be a function of change in strain energy release rate, in the crack tip within each cyclic loading and can be written as:

$$\partial a/\partial N = C(\Delta G / Gc)\hat{}m \quad (4.1)$$

where G_C is the critical fracture energy, C and m are fitting parameters determined experimentally.

When the specimen is under mixed mode loading, i.e. Mode I and Mode II, the parameters C and m can be determined depending on linear or parabolic equations based on pure mode cases as in the following expressions (Kawashita and Hallett 2012):

Linear rule

$$C = \frac{G_I}{G_I+G_{II}} C_I + \frac{G_{II}}{G_I+G_{II}} C_{II} \tag{4.2}$$

$$m = \frac{G_I}{G_I+G_{II}} m_I + \frac{G_{II}}{G_I+G_{II}} m_{II} \tag{4.3}$$

Parabolic rule

$$\log C = \log C_I + \left(\frac{G_{II}}{G_T}\right) \log C_m + \left(\frac{G_{II}}{G_T}\right)^2 \log \frac{C_{II}}{C_m C_I} \tag{4.4}$$

$$m = m_I + m_m \left(\frac{G_{II}}{G_I+G_{II}}\right) + (m_{II} - m_I - m_m) \left(\frac{G_{II}}{G_I+G_{II}}\right)^2 \tag{4.5}$$

where the subscripts I and II indicates Mode I ,Mode II, and mode ratio. m is a mixed mode parameter to be experimentally determined.

Fatigue delamination does not propagate if the strain energy rate does not reach the threshold value G_{th}. In this region no measurable fatigue crack growth occurs and it is called the subcritical growth region, as shown in Figure 4.2 (Region I). The delamination grows linearly when the energy release rate during the cyclic loading exceeds the threshold value. This is known as the region of stable growth (Region II) when plotted on a log–log scale, as shown in Figure 4.2. The nonlinear or unstable growth (Region III)

occurs if the strain energy release rate is near to the static fracture energy Gc, see Figure 4.2 (Landry and LaPlante 2012).

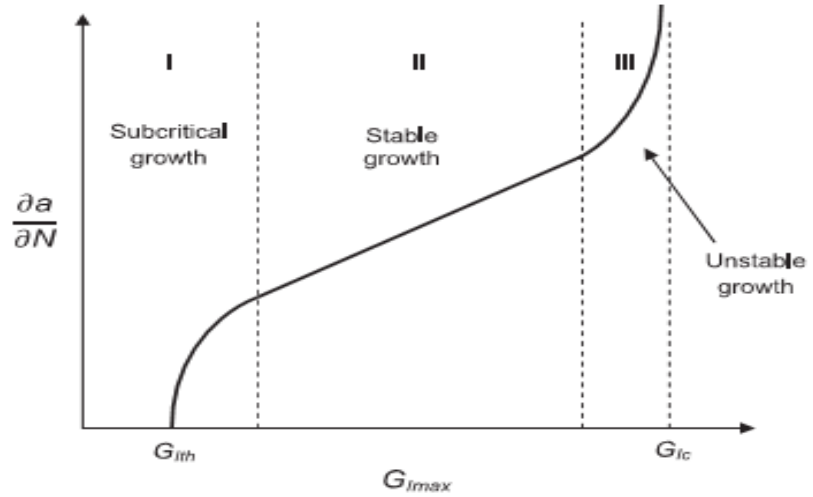

Figure 4.2 Typical fatigue delamination growth curve (Landry and LaPlante 2012)

The change in strain energy rate during fatigue loading can be calculated from the instantaneous maximum strain energy and the load ratio R as (Belnoue et al., 2016):

$$\Delta G = (1 - R^2) G_{max} \tag{4.6}$$

where R is the load ratio and is defined by the user input in the numerical model. G_{max} is calculated from the traction–separation curve of the cohesive zone model (CZM) for each fatigue cycle.

The interface element is easily simulated in a numerical model based on traction-separation responses, the fracture process zone ahead of a crack tip can be modelled using a CZM. Many different types of traction-separation relations have been investigated in the literature e.g. polynomial law (Needleman 1987), trapezoidal model (Tvergaard and Hutchinson 1992), perfectly plastic relationship (Cui and Wisnom 1993), exponential law (Xu and Needleman 1994), and bilinear cohesive law (Reedy et al., 1997). Among these the bilinear law gives good convergence of the finite element

model and numerically is the simplest formulation (Alfano 2006) and (Landry and LaPlante 2012).

It is worthwhile to mention that the static damage evolution should be included in modelling the delamination growth under fatigue conditions. The total damage parameter can be calculated during cyclic loading as:

$$\mathrm{D_{tot}} = \mathrm{D} + \mathrm{D_f} \tag{4.7}$$

where D is static damage evolution and $\mathrm{D_f}$ is fatigue damage parameter.

The total damage $\mathrm{D_{tot}}$ is used to update the cohesive traction at each element after each time-step. Complete failure of an element takes place once the total damage reaches unity and (Harper and Hallett 2010):

$$\tau = (1 - D)k\delta \quad static\ loading \tag{4.8a}$$

$$\tau = (1 - D_{tot})k\delta \quad fatigue\ loading \tag{4.8b}$$

where τ is cohesive traction , k is interface stiffness, and δ is relative displacement .

Energy release rate at the crack tip can be calculated by integrating the traction-separation curve under cyclic loading, unless complete failure occurs. The fatigue loading causes stiffness degradation in the interface element, this leads to increase separation as total damage evolution accumulates. The highest strain energy release rate will be in those elements that lie in the process zone near to the numerical crack tip. The response of traction separation will follow a non-vertical path which matches the bi-linear law for static loading according to (Turon et al., 2007) and (Harper and Hallett 2010).

4.2 Developed fatigue damage degradation

The quadratic nominal stress criterion to predict the onset of delamination under mixed mode loading is one of the most frequently adopted failure criteria (Ibrahim and Albarbar 2019). This criterion has been successfully utilized by many researchers e.g. (Hameed et al., 2020) , (Zou and Hameed 2018), (Belnoue et al., 2016) and (Kawashita and Hallett 2012), and is written as;

$$F_i = \left(\frac{\langle \tau_n \rangle}{\tau_{nc}}\right)^2 + \left(\frac{\tau_s}{\tau_{sc}}\right)^2 + \left(\frac{\tau_t}{\tau_{tc}}\right)^2 \quad (4.9)$$

where τ_n , τ_s , τ_t are the normal, shear and tear stresses respectively and where the operator $\langle x \rangle$ is defined as;

$$\langle x \rangle = \begin{cases} x, & x > 0 \\ 0, & x \leq 0 \end{cases}$$

Damage growth under pure-mode loading is predicted using the energy release rate during loading and unloading, and fracture toughness:

$$F_p = \frac{G}{G_c} \quad (4.10)$$

The static damage evaluation is derived from damage surface concept and is written as:

Damage initiation criterion (F_i) + Damage propagation criterion (F_p) = 1

From this condition, the static damage evaluation can be expressed as

$$D = 1 - \sqrt{\frac{1 - F_p}{\left[\frac{k_1^2 \delta_1^2}{\tau_{1c}^2} + \frac{k_2^2 \delta_2^2}{\tau_{2c}^2} + \frac{k_3^2 \delta_3^2}{\tau_{3c}^2}\right]}} \quad (4.11)$$

The ratio between damaged (L_d) and undamaged (L_u) parts was assumed by (Turon et al., 2007) to equal the ratio of the dissipated energy over the representative interface part. Therefore, the damage growth criterion for pure mode can be written as:

$$F_p = \frac{G}{G_c} = \frac{L_d}{L_u} \tag{4.12}$$

Where L_u is mesh size and L_d is the length of damaged elements.

Substitute Equation 4.12 into the static damage evaluation Equation 4.11, to obtain the relation between damage evaluation and damaged length ratio:

$$D = 1 - \sqrt{\frac{1-\frac{L_d}{L_u}}{\left[\frac{k_1^2\delta_1^2}{\tau_{1c}^2}+\frac{k_2^2\delta_2^2}{\tau_{2c}^2}+\frac{k_3^2\delta_3^2}{\tau_{3c}^2}\right]}} \tag{4.13}$$

By differentiating the above equation with respect to the damaged length, we obtain a novel term $\frac{\partial D}{\partial L_d}$, not found elsewhere in the literature and which can be written as:

$$\frac{\partial D}{\partial L_d} = \frac{1}{2} * \frac{1}{L_u} * \frac{1}{\sqrt{\frac{1-\frac{L_d}{L_u}}{\left[\frac{k_1^2\delta_1^2}{\tau_{1c}^2}+\frac{k_2^2\delta_2^2}{\tau_{2c}^2}+\frac{k_3^2\delta_3^2}{\tau_{3c}^2}\right]}}} * \frac{1}{\left[\frac{k_1^2\delta_1^2}{\tau_{1c}^2}+\frac{k_2^2\delta_2^2}{\tau_{2c}^2}+\frac{k_3^2\delta_3^2}{\tau_{3c}^2}\right]} \tag{4.14}$$

The evaluation of the rate of fatigue damage for each cyclic loading ($\partial D/\partial N$) on the traction–separation curve is a function of the novel term ($\partial D/\partial L_d$) and the damage growth rate ($\partial L_d/\partial N$) over the process zone. The expression for the required rate can be written as:

$$\frac{\partial D}{\partial N} = \frac{\partial D}{\partial L_d} * \frac{\partial L_d}{\partial N} \tag{4.15}$$

So,

$$\frac{\partial D}{\partial N} = \frac{1}{2} * \frac{1}{L_u} * \frac{1}{\sqrt{\frac{1-\frac{L_d}{L_u}}{\left[\frac{k_1^2\delta_1^2}{\tau_{1c}^2}+\frac{k_2^2\delta_2^2}{\tau_{2c}^2}+\frac{k_3^2\delta_3^2}{\tau_{3c}^2}\right]}}} * \frac{1}{\left[\frac{k_1^2\delta_1^2}{\tau_{1c}^2}+\frac{k_2^2\delta_2^2}{\tau_{2c}^2}+\frac{k_3^2\delta_3^2}{\tau_{3c}^2}\right]} * \frac{\partial L_d}{\partial N} \tag{4.16}$$

The damage accumulates ahead of the crack tip in the fracture process zone to give additional delamination length. This new length of delamination is calculated based on the damage fatigue crack lengths, L_d, of all elements

which lie in the cohesive zone area. It is written as a summation function in the direction of delamination growth as:

$$a = \sum_{e \in L_{CZ}} L_d^e \tag{4.17a}$$

where L_{CZ} is the length of the cohesive zone and calculated as (Turon et al., 2007):

$$L_{CZ} = \frac{9\pi}{32} \frac{G_c}{(\tau_c)^2} E \tag{4.17b}$$

Where E is the Young's modulus of the material.

The Equation (4.17a) is derived with respect to the number of cycles to obtain the crack growth rate, $\partial a/\partial N$, as function of $(\partial L_d/\partial N)$.

$$\partial a/_{\partial N} = \sum_{e \in L_{CZ}} \partial L_d^e/_{\partial N} \tag{4.18}$$

The incremental rate of delamination is assumed to be equal for all elements within the cohesive zone area. Therefore, the summation sign can be rewritten in terms of the number of elements (EN_{CZ}) in the process zone, L_{CZ} (Skvortsov et al., 2016). The fatigue delamination growth rate can then be written as:

$$\partial a/_{\partial N} = EN_{CZ} * \frac{\partial L_d}{\partial N} \tag{4.19}$$

where

$EN_{CZ} = length\ of\ cohesive\ zone\ (L_{CZ})/element\ length\ (L_u)$.

By substituting Equation 4.19 into Equation 4.16, the rate of fatigue damage ($\partial D/\partial N$) is related to Paris' law as:

$$\frac{\partial D}{\partial N} = \frac{1}{2} * \frac{1}{L_u} * \frac{1}{\sqrt{\frac{1-\frac{L_d}{L_u}}{\left[\frac{k_1^2\delta_1^2}{\tau_{1c}^2}+\frac{k_2^2\delta_2^2}{\tau_{2c}^2}+\frac{k_3^2\delta_3^2}{\tau_{3c}^2}\right]}}} * \frac{1}{\left[\frac{k_1^2\delta_1^2}{\tau_{1c}^2}+\frac{k_2^2\delta_2^2}{\tau_{2c}^2}+\frac{k_3^2\delta_3^2}{\tau_{3c}^2}\right]} * \frac{1}{EN_{CZ}} * C\left(\Delta G/_{G_c}\right)^m \tag{4.20}$$

In the UMAT subroutine, the fatigue damage degradation is updated in the model for each time-step as;

$$D_f^{new} = D_f^{old} + \Delta N \frac{\partial D}{\partial N} \quad (4.21)$$

ΔN is calculated as follows:

$$\Delta N = frequency * step\ time. \quad (4.22)$$

4.3 Double cantilever beam (DCB) model

Double cantilever beam (DCB) specimens as reported by (Landry and LaPlante 2012) were adopted for this numerical simulation. The length and width of the specimen was 150 mm and 20 mm respectively with pre-crack length of 50 mm. The specimens have two unidirectional 16 ply-thick (3 mm thick) layers made from carbon/epoxy with material properties shown in Table 4.1. All simulations in this study were subjected to Mode I static and fatigue loading, and carried out using commercial finite element software ABAQUS. A two dimensional finite element model of DCB was implemented to reduce computational effort and save computer time. The layers were meshed using 4-node plane strain elements, whereas the cohesive elements were meshed with element type COH2D4 and placed between layers where the crack was expected to propagate.

Table 4-1 Material properties of the carbon/epoxy layers used (Landry and LaPlante 2012)

E_{11} (GPa)	E_{22} (GPa)	E_{33} (GPa)	v_{12}	G_{12} (GPa)	G_{IC} (N/m)
155	10.5	10.5	0.32	4.83	422

First, the static load was numerically applied on the DCB by specifying an opening displacement of each cantilever arm. The numerical results for energy as a function of displacement have been validated with experimental data reported by (Landry and LaPlante 2012). The response of strain energy with each initial displacement is in good agreement with experimental results, as shown in Figure 4.3.

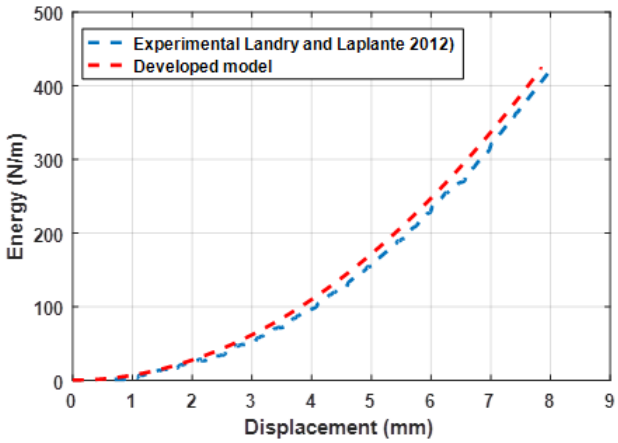

Figure 4.3 Comparison between developed model and experimental results of fracture toughness

The experimental procedure was performed by (Landry and LaPlante 2012) as follows; the specimens were cracked approximately 5 mm and then subsequently subjected to the quasi-static load. When opening displacement reached 9.5 mm, the static load was stopped and then, sinusoidal displacement cycles with an amplitude of 8 mm were performed as shown in Figure 4.4. The novel approach to fatigue damage degradation was implement in ABAQUS via the UMAT subroutine. It was necessary to define the cohesive zone length in the model which was estimated based on traction values, fracture toughness and Young's modulus of the cohesive material. Fatigue delamination growth is determined by relating the damage accumulation of cohesive elements to the Paris growth law, Equation 4.20.

The damage accumulates with each cyclic loading based on Equation 4.21 to produce a new crack length.

Figure 4.4 Opening displacement of DCB under cyclic loading

Figure 4.5 illustrates damage accumulation for the DCB under different numbers of cycles. It is clear that the delamination length increases when the number of cycles increases from 250 to 3500. The percentage error between proposed model and experimental data is determined as;

$$\boldsymbol{error} = \frac{\boldsymbol{experimental\ value - simulation\ value}}{\boldsymbol{experimental\ value}}\ \% \qquad (4.23)$$

For example, the error at 250 cycle is calculated as; $\boldsymbol{error} = \frac{\mathbf{61-58}}{\mathbf{61}}\ \% \cong \mathbf{5}\%$.

In the same way, the error at 3500 cycles can be determined and it is about 3% as shown in Figure 4.6. Figure 4.7 presented a comparison between developed model predictions and experimental results for delamination growth.

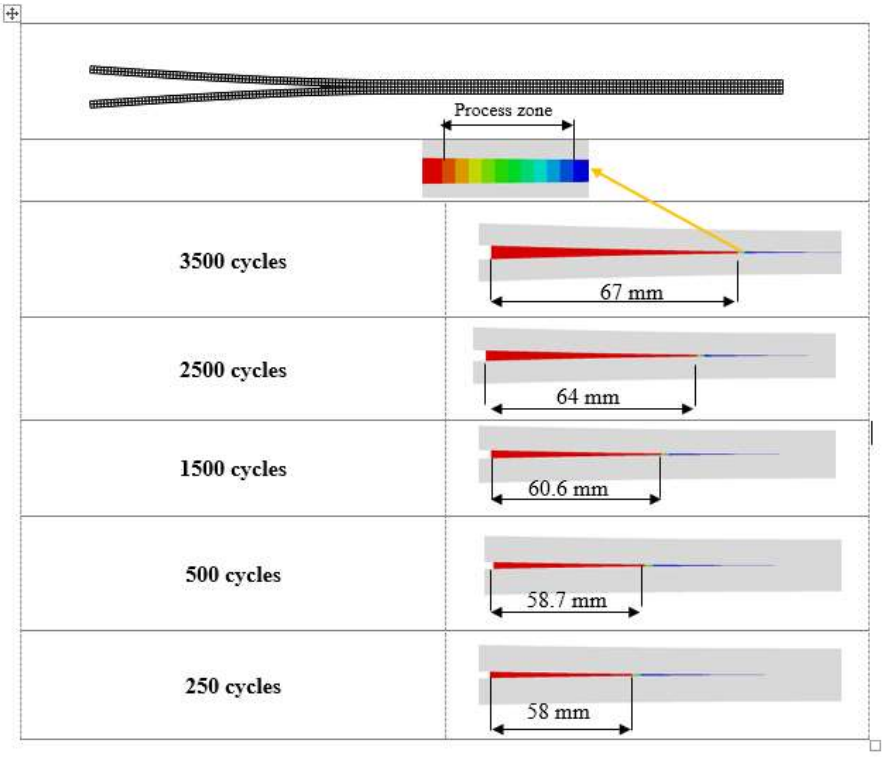

Figure 4.5 Delamination growth in DCB under different cyclic loadings

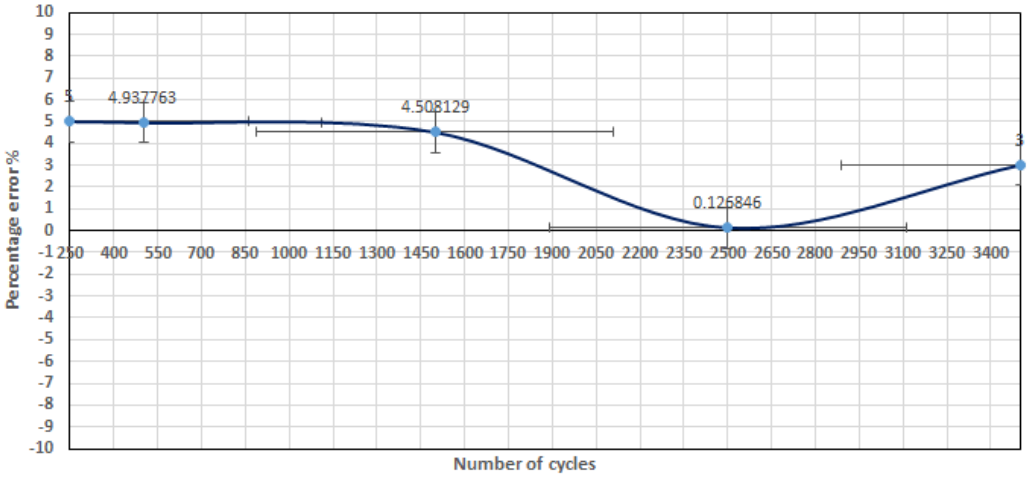

Figure 4.6 Percentage error between proposed model and experimental data

Figure 4.7 Comparison between developed model predictions and experimental results for delamination growth

The fatigue crack growth rate using the developed model can be represented by a Paris plot as shown in Figure 4.8. The stable growth area was adopted in this study rather than the full $\partial a/\partial N$ region .The simulation results of mixed mode were validated against experimental data available in literature (Kenane and Benzeggagh 1997).

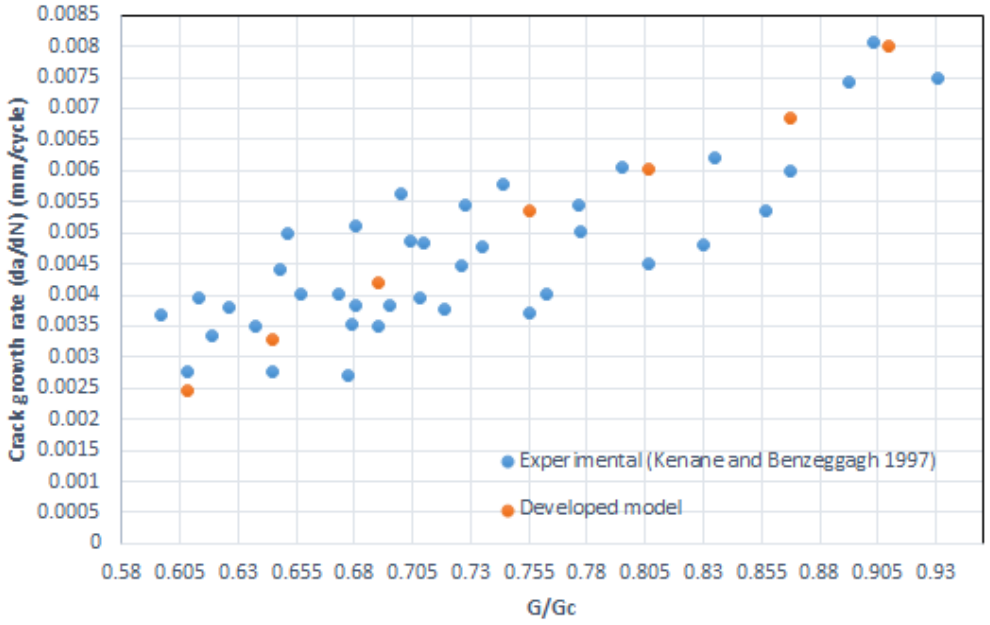

Figure 4.8 Comparison of simulated fatigue crack growth rates and experimental data available in literature (Kenane and Benzeggagh 1997)

4.4 Single lap joint (SLJ) model

Adhesively bonded joints have many advantages e.g., lower weight, and better fatigue performance compared with classical mechanically fastened joints. Therefore, they are used in many structural applications in industries such as automotive and aerospace. The increase in demand for adhesively bonded joints has been accompanied by investigating and developing numerical models to predict the response of the structure, and to describe the behaviour of damage in the adhesive joints (de Moura and Goncalves 2014). The cohesive zone model is a very effective way to model adhesively bonded joints using finite element analysis.

(Khoramishad et al., 2010) carried out static and fatigue loading of single lap joints (SLJ). The specimen consisted of two aluminium 2024-T3 layers bonded with FM 73 M OST toughened epoxy film adhesive. The substrates were pre-treated prior to bonding. This pre-treatment consisted of a chromic acid etch (CAE) and phosphoric acid anodising (PAA) followed by the application of BR 127 corrosion inhibiting primer, to maximise environmental resistance and bonding durability. The joints were cured at 120 ^{o}C, under 0.28 MPa pressure for 60 min. The dimensional details of the SLJ are shown in Figure 4.9. The overlap length, the width and the thickness of the bond line were 30, 12.5 and 0.2 mm, respectively. The finite element model showing the mesh element distribution using ABAQUS software is illustrated in Figure 4.10.

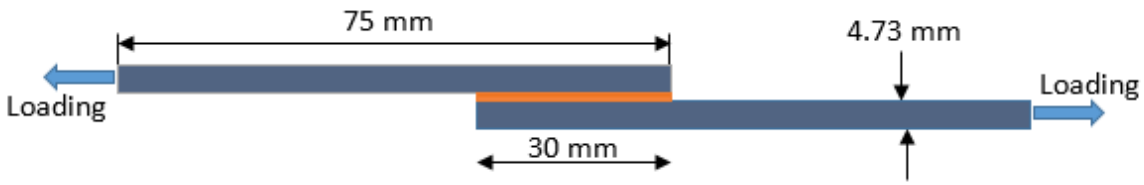

Figure 4.9 Single lap joint geometries

Figure 4.10 Mesh element distribution of single lap joint specimen

The static tests were carried out by (Khoramishad et al., 2010) on the single lap joints (SLJ) to find cohesive zone properties e.g., fracture energy. The displacement control was applied to the specimen at a rate of 0.1 mm/min. Average static strengths of 10.0 kN was observed for the SLJ. After that, the single lap joints (SLJ) specimen was tested under fatigue load condition at 5 Hz with a load ratio of 0.1.

The interface element length used over the cohesive zone depends on mesh size in the finite element model. It effects the sensitivity of the fatigue response according to (Naghipour et al., 2010). Vassilopoulos (Vassilopoulos 2015), in previous studies investigated the effect of mesh element size on convergence of the numerical model and found that using a mesh size less than 1 mm for the interface element provided better solution convergence. Therefore, in the present simulation the element size adopted for the adhesive was 0.2 mm.

Fatigue modelling was performed at maximum fatigue load of 40% of the static final failure load which was measured experimentally at about 10 kN. When the specimen was loaded statically at 4 kN, as shown Figure 4.11, it can be seen that, initially, the damage parameter is less than unity for each of the first three elements of cohesive layer. The elements 1, 2, and 3 are indicated in Figure 4.12a. When the fatigue loading was activated, the first and second elements needed 200 cycles for the rate of increase of damage to begin to accelerate rapidly whereas in the third element the rate of

increase of damage began to accelerate after about 500 cycles. This was because the value of the damage parameter for the third element at the end of the static stage was less than for the first and second elements.

The delamination growth was simulated based on the model developed here. It should be observed that the damage grew symmetrically on both side of the adhesively bonded joint as shown in Figure 4.12 .The variation of the damage parameter under different numbers of cycles, as predicted by the present model is also illustrated in Figure 4.12. The elements having state variable (SDV3) equal to unity in the damage contours represent complete failure of the cohesive zone, signifying no fatigue resistance. Based on the model proposed here the crack needed 2000 cycles to grow to 0.30 mm, and propagated to 0.45 mm when the number of cycles reached 4000. The measured delamination lengths by (Khoramishad et al., 2010) were 0.285 mm and 0.43 mm for 2000 and 4000 cycles respectively. Thus, the difference between numerical model and test was 5.2% at 2000 cycles and 4.6 % at 4000 cycles.

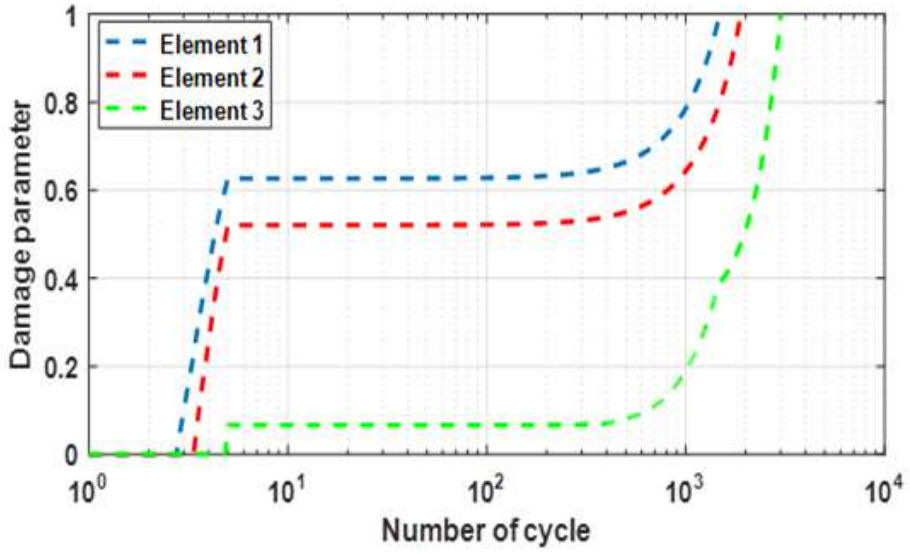

Figure 4.11 Damage propagation of the first, second and third element

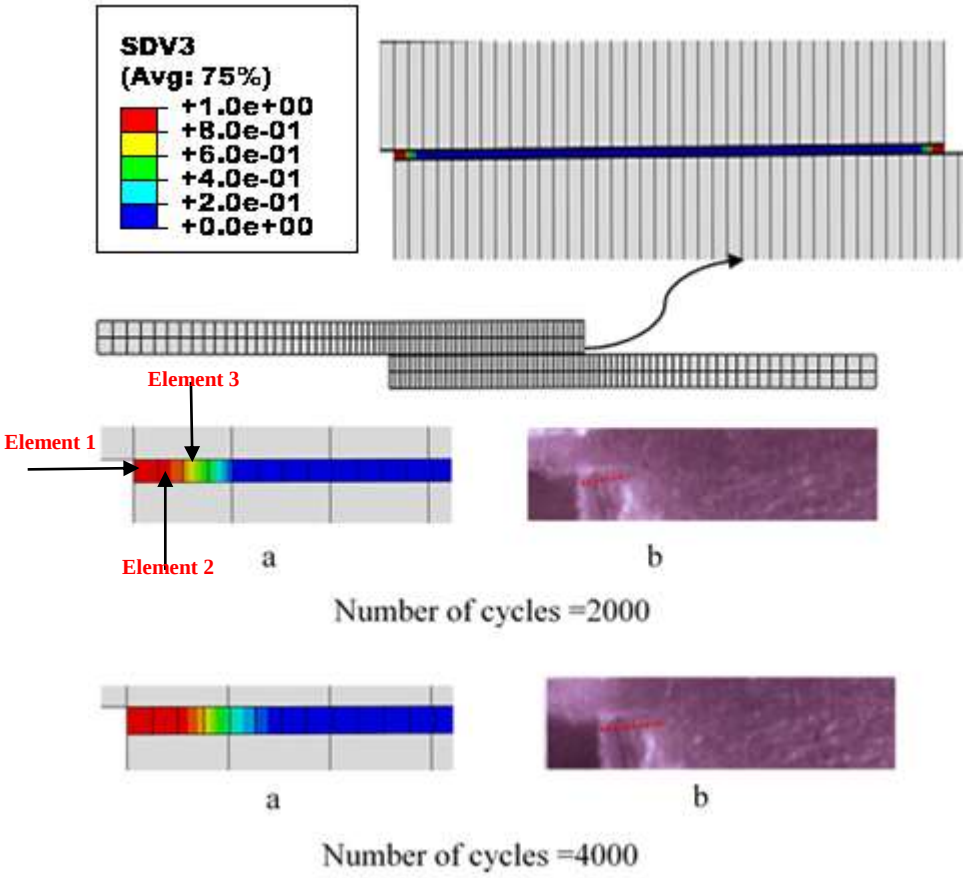

Figure 4.12 Delamination growth under different cyclic loading (a) developed model (b) experimental data (Khoramishad et al., 2010)

4.4 Summary

A cohesive zone model for delamination propagation in laminated composites under static and fatigue loading has been derived and validated with experimental data under different mode conditions. This chapter presents a new approach to quantify fatigue delamination degradation based on damage mechanics to evaluate the rate of fatigue damage ($\partial D/\partial N$). The static damage evaluation and fatigue damage degradation are derived from the surface damage concept. Both static and fatigue damage linked were to each other to establish fatigue crack growth formula in the laminated composites. A user-defined subroutine, UMAT, has been

employed to develop and implement a damage model in ABAQUS. Two different specimens; a double cantilever beam and a single lap joint were used to investigate the effectiveness of the new method. The simulation results revealed that the developed model had good agreement with experimental data available in literature.

Chapter 5 : Damage degradation modelling for transverse cracking in composite laminates under low-velocity impact

This chapter briefly introduces intralaminar yield surface criteria. Different failure criteria will be presented to describe how the damage initiation in the composite structure can be predicted. It then introduces the concept of damage surface and the steps that can be followed to achieve a new damage evolution law for both fibre and matrix cracking.

5.1 Intralaminar yield surface criteria

The yield surface behaviour in the laminated composite can be determined using strength-based yield criteria. Various failure criteria have been widely employed to predict the damage initiation in the composite structure. (Hashin and Rotem 1973) and (Hashin 1980) confirmed the need for failure criteria that are based on failure mechanisms and proposed a yield surface criterion based on their experimental observations made during tensile tests. Two failure criteria were introduced to indicate the damage in the fibre and matrix. Quadratic failure criteria were presented to include the stress interactions that acting on the failure plane. The Hashin failure criteria are written as follows (Hashin 1980):

Fibre tension damage initiation ($\sigma_{11} > 0$);

$$\left(\frac{\sigma_{11}}{X_T}\right)^2 \geq 1 \tag{5.1}$$

Fibre compression damage initiation ($\sigma_{11} < 0$);

$$\left(\frac{\sigma_1}{X_C}\right)^2 \leq 1 \tag{5.2}$$

Matrix tension damage initiation ($\sigma_{22} > 0$);

$$\left(\frac{\sigma_{22}}{Y_T}\right)^2 + \left(\frac{\sigma_{12}}{S_{12}}\right)^2 \geq 1 \tag{5.3}$$

Matrix compression damage initiation ($\sigma_{22} < 0$)

$$\left(\frac{\sigma_{22}}{Y_C}\right)^2 + \left(\frac{\sigma_{12}}{S_{12}}\right)^2 \leq 1 \tag{5.4}$$

where σ_{11} is the stress in the direction of the fibres, σ_{22} is the stress in the transverse direction perpendicular to the fibres, X_T is the tensile strength and X_C is the compressive strength of the fibres, Y_T is the tensile strength

and Y_C is the compressive strength of the matrix. σ_{12} and S_{12} are the shear stress and transverse shear strength respectively (Hameed et al., 2020).

Many studies have investigated the effectiveness of Hashin's criterion especially in the case of the compression mode. The experimental data indicates that the weakness of Hashin's criterion is its sensitivity to the onset of failure when the laminated composite undergoes compressive load. Experimental evidence has demonstrated that the shear strength of a ply increases when the unidirectional laminates are subjected to moderate transverse compression ($\sigma_{22} < 0$), (Davila et al., 2005).

Many modifications have been made to improve Hashin criteria's predictive capabilities. (Sun et al., 1996) introduced an empirical modification to matrix cracking failure under compressive load, they modified Hashin's criteria to take into consideration the increase in shear strength due to compressive stress ($\sigma_{22} < 0$). This modification is written as:

$$\left(\frac{\sigma_{22}}{Y_C}\right)^2 + \left(\frac{\sigma_{12}}{S_{12}+\mu\sigma_{22}}\right)^2 = 1 \qquad (5.5)$$

where μ is a constant found experimentally, it plays a role similar to a friction coefficient and is referred as an internal material friction parameter. The denominator of the modified criterion ($S_{12} + \mu\sigma_{22}$) increases the effective longitudinal shear strength when transverse compression occurs.

(Puck and Schürmann 2002) experimentally studied unidirectional composite laminate under transverse compression. Their investigation focused on the fracture plane orientation due to matrix compression. The experimental findings showed that the transverse damage occurred when shear stress along fracture plane was oriented by an angle $\alpha = 53 \mp 2^0$ with respect to the fibre orientation. The angle of the fracture plane, α, is

illustrated in Figure 5.1, which also shows the three stress transformations (L. T and N) which act on the fracture plane (Donadon et al., 2008) and (Liao and Liu 2017).

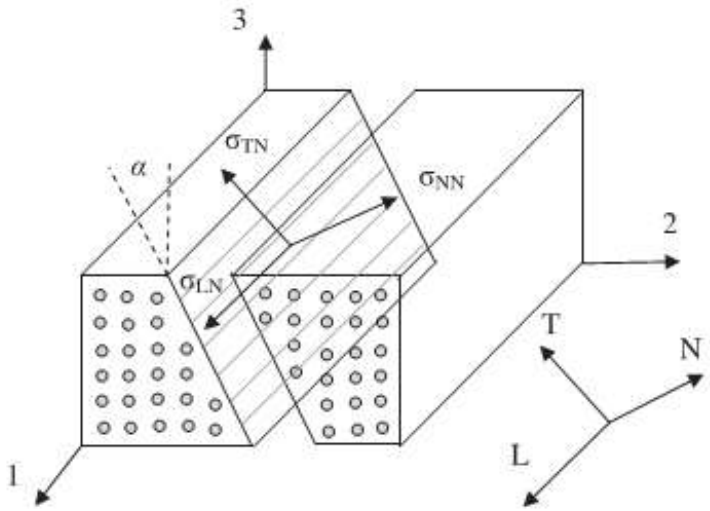

Figure 5.1 Fracture plane of matrix cracking under compressive load (Shi et al., 2012)

In order to take these features into consideration, the failure theory adopted should include the combination of the three stress transformations in the fracture plane. (Puck and Schürmann 2002) introduced a solution based on the Mohr-Coulomb failure criterion, and a local quadratic stress interaction was suggested to determine onset of the failure. In their modifications, normal compressive stress (σ_{nn}), shear stress (σ_{nt}) and (σ_{nl}) which act together on the fracture plane should be taken into consideration and compared with the strengths in their action planes.

The second suggestion presented by (Puck and Schürmann 2002) assumed that the transverse compressive stress on the yield surface plane affects failure initiation and enhances the resistance to shear fracture. Figure 5.2 shows how out-of-plane shear strength (S_{23}) and in-plane shear strength (S_{12}) can be enhanced as functions of the normal compressive

stress (σ_{nn}). The tangent to the Mohr–Coulomb curve for transverse compression, shown in Figure 5.2, is typically expressed by the equation of a line ($\bar{S}_{23} = S_{23} + \mu_{nt}\sigma_{nn}$), where the intercept point on the σ_{nt} axis is transverse shear strength S_{23}, and the gradient of the line is $\mu_{nt} = \tan(\varphi)$, where $\varphi = 2\alpha - 90$. Therefore, resistance to shear fracture increases as a function of the normal compressive stress. Similarly, ($\bar{S}_{12} = S_{12} + \mu_{nl}\sigma_{nn}$) for in-plane shear strength (S_{12}). The proposed fracture failure criterion of (Puck and Schürmann 2002) can be written as:

$$\mathcal{F}_{22}^{c}(\sigma_{nt}, \sigma_{nl}, \bar{S}_{12}, \bar{S}_{23}) = (\frac{\sigma_{nl}}{\bar{S}_{12}})^2 + (\frac{\sigma_{nt}}{\bar{S}_{23}})^2 \geq 1 \quad (5.6)$$

Substituting for $\bar{S}_{12}$ and $\bar{S}_{23}$, the failure criterion for transverse compression failure can be written as:

$$\mathcal{F}_{22}^{c}(\sigma_{nn}, \sigma_{nt}, \sigma_{nl}) = (\frac{\sigma_{nl}}{S_{12}+\mu_{nl}\sigma_{nn}})^2 + (\frac{\sigma_{nt}}{S_{23}+\mu_{nt}\sigma_{nn}})^2 \geq 1 \quad (5.7)$$

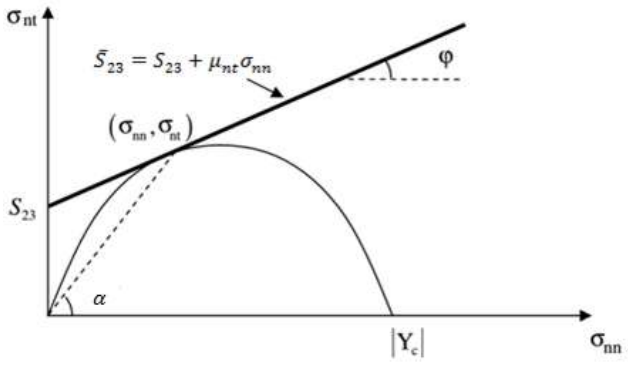

Figure 5.2 Tangential line of Mohr–Coulomb behaviour for transverse compression (Donadon et al., 2008)

5.2 Derivation of damage degradation model and incremental law

The experimental tests carried out as part of the World-Wide Failure Exercise (WWEF) for predicting failure in composite laminates (Hinton et al., 2002) compared failure results predicted by the failure criteria for unidirectional composite E-Glass/LY556 with experimental evidence to

investigate the strengths and weaknesses of each of the criteria. Figure 5.3 presents the failure envelopes of the various failure criteria together with experimental results over the transverse stress (σ_{22}) - shear stress (σ_{12}) domain to identify the overall effectiveness of each theory. It can be observed that in the tension test (positive range of σ_{22}) all failure criteria predictions of the yield surface are close to the experimental data (WWEF test) performed by (Hinton et al., 2002). In the compression test, the failure criteria should be carefully selected to determine the onset of the failure. The boundary of the failure envelope obtained by (Hashin and Rotem 1973) when σ_{22} has a negative sign (compressive) does not fit experimental data. (Hashin 1980) presented a modest improvement in accuracy of the predicted failures, and the failure behaviour was closer to the experimental results as shown in Figure 5.3. However , the modified failure criteria by (Sun et al., 1996) and (Puck and Schürmann 2002) gave more satisfactory results and showed significant improvement compared with Hashin's criteria.

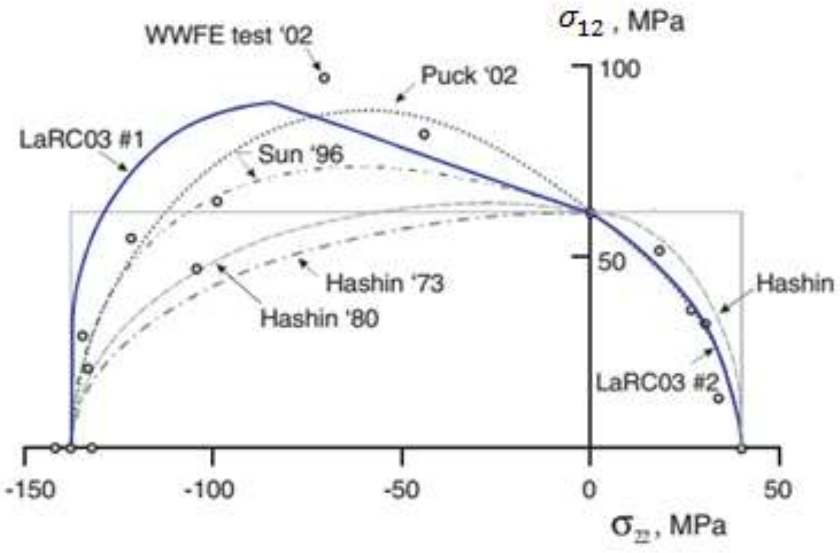

Figure 5.3 Failure envelopes of the various failure criteria (Davila et al., 2005)

If damage in the composite laminates takes place, it is very important to understand how the stiffness of the material is degraded by the damage mode. The concept of damage evolution assumes that material failure will follow an ongoing reduction in the stiffness of the material (Hameed et al., 2020). Damage evolution laws or rules are used for describing the failure propagation in the structure.

Stress or strain-based failure criteria have been used by many researchers to assess the damage level in laminated composites. The four major damage degradation modes in laminated composites are: matrix tension, matrix compression, fibre tension and fibre compression damage, in addition to which this study introduces shear damage degradation as a new approach. For simplicity, damage propagation behaviour will be developed based on (Hashin and Rotem 1973) when laminated composites were subjected to tensile or transverse compressive stresses.

The new approach to the damage evaluation law can be derived based on the damage surface concept (Ibrahim et al., 2020). The damage surface is written as:

Initiation criteria ($\mathbb{F}_i$) + Propagation criteria (Ψ) = 1

The undamaged specimen is assumed linearly elastic, see Figure 5.4, this is followed by the onset of damage, whether transverse cracking damage or fibre breakage can be determined by using one of the above-mentioned failure criteria. As shown in Figure 5.4, it is clearly observed that the strain, ε_{11}^{ft} and ε_{11}^{fc} represent the maximum values of strain when the damage parameter reaches unity in tension and compression tests, respectively. Also, it can be noticed the longitudinal direct stress σ_{11} is degraded

according to $\sigma_{11} = E_{11}(1 - \omega_{11})\varepsilon_{11}$ until complete failure of an element takes place in tension, or approaches a minimum residual strength which is comparable to the transverse compressive strength (Donadon et al., 2008), (Feng and Aymerich 2014), and (Liu et al., 2016).

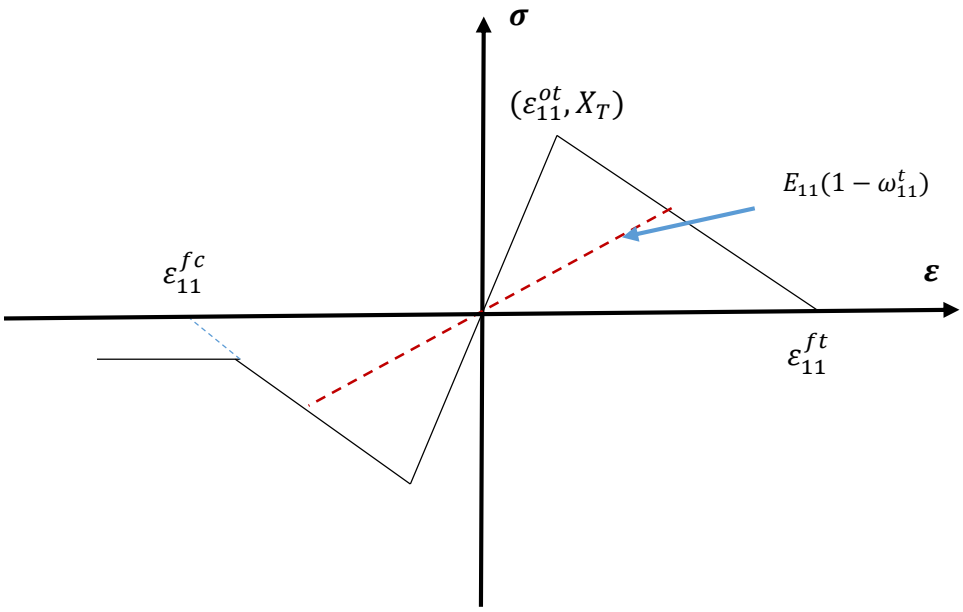

Figure 5.4 Damage behaviour in the fibre direction

The damage evolution law of each damage mode for fibre or matrix is achieved in this study using damage initiation and surface concepts. The damage initiation of the fibre was introduced by (Hashin and Rotem 1973) as ($\sigma_{11} > 0$) and ($\sigma_{11} < 0$) these are substituted in the damage surface as:

$$\left(\frac{\sigma_{11}}{X_T}\right)^2 + \Psi_{11}^{t} = 1 \qquad \sigma_{11} > 0 \qquad (5.8)$$

$$\left(\frac{\sigma_{11}}{X_C}\right)^2 + \Psi_{11}^{c} = 1 \qquad \sigma_{11} < 0 \qquad (5.9)$$

where Ψ_{11} is the damage growth function which depends on energy release rate (G_{11}) during loading and unloading, and fracture toughness (Ibrahim and Albarbar 2019). Damage growth under pure-mode loading based on

energy release rate during loading, and fracture toughness (Ibrahim, et al., 2020), is written as:

$$\Psi_{11}^{t} = \frac{G_{11}}{G_{f11}^{t}} \qquad \sigma_{11} > 0 \tag{5.10}$$

$$\Psi_{11}^{c} = \frac{G_{11}}{G_{f11}^{c}} \qquad \sigma_{11} < 0 \tag{5.11}$$

where G_{f11}^{t} , G_{f11}^{c} are intralaminar fracture toughness in tension and compression respectively with respect to the direction of the fibres.

The damage parameter symbol of a fibre under tension and compression is written in this study as ω_{11}^{t}, and ω_{11}^{c} respectively. Therefore, the stress will be degraded for both load conditions (tension and compression) as follows;

$$\sigma_{11} = E_{11}(1 - \omega_{11}^{t})\varepsilon_{11}^{t} \qquad \sigma_{11} > 0 \tag{5.12}$$

$$\sigma_{11} = E_{11}(1 - \omega_{11}^{c})\varepsilon_{11}^{c} \qquad \sigma_{11} < 0 \tag{5.13}$$

where E_{11} is longitudinal Young's modulus, ε_{11}^{t} and ε_{11}^{c} are tension and compression strains in the direction of the fibres.

Substituting the longitudinal direct stress (σ_{11}) degradation into the damage surface and re-arranging the equations, we derive the new damage evaluation law for fibres. The new damage parameter function is written as:

$$\omega_{11}^{t} = 1 - \left(\frac{X_T}{E_{11}\varepsilon_{11}^{t}}\right)\sqrt{1 - \Psi_{11}^{t}} \qquad \sigma_{11} > 0 \tag{5.14}$$

$$\omega_{11}^{c} = 1 - \left(\frac{X_C}{E_{11}\varepsilon_{11}^{c}}\right)\sqrt{1 - \Psi_{11}^{c}} \qquad \sigma_{11} < 0 \tag{5.15}$$

The second goal of this study is to determine a new approach to the matrix damage degradation law. The failure criteria of the matrix damage initiation introduced by (Hashin and Rotem 1973) when ($\sigma_{22} > 0$) is substituted in the damage surface as:

$$\left(\frac{\sigma_{22}}{Y_T}\right)^2 + \left(\frac{\sigma_{12}}{S_{12}}\right)^2 + \Psi_{22}^t = 1 \quad (5.16)$$

The stress (σ_{22}) in the transverse direction is assumed to degrade as $\sigma_{22} = E_{22}(1 - \omega_{22}^t)\varepsilon_{22}^t$. Where ω_{22}^t is the matrix damage parameter under tension, ε_{22}^t is the tension strain in the transverse direction, and E_{22} is the transverse Young's modulus. The propagation failure criteria of the tension matrix cracking, Ψ_{22}^t, is written as:

$$\Psi_{22}^t = \frac{G_{22}}{G_{m22}^t} \quad (5.17)$$

where G_{m22}^t is the intralaminar fracture toughness in tension in the transverse direction, and G_{22} is energy release rate during matrix cracking. When the transverse stress degradation is substituted in the damage surface condition, the equation can be written as:

$$\left(\frac{E_{22}(1-\omega_{22}^t)\varepsilon_{22}^t}{Y_T}\right)^2 + \left(\frac{\sigma_{12}}{S_{12}}\right)^2 + \Psi_{22}^t = 1 \quad (5.18)$$

The new approach to the damage evolution law for matrix cracking in tension is developed as:

$$\omega_{22}^t = 1 - \left(\frac{Y_T}{E_{22}\varepsilon_{22}^t}\right)\sqrt{1 - \left(\frac{\sigma_{12}}{S_{12}}\right)^2 - \Psi_{22}^t} \quad (5.19)$$

The failure criteria introduced by (Hashin and Rotem 1973) is also adopted to develop the damage degradation law when a compressive load is applied ($\sigma_{22} < 0$). It is useful to mention that the stress (σ_{22}) in the transverse direction under compression is degraded as $\sigma_{22} = E_{22}(1 - \omega_{22}^c)\varepsilon_{22}^c$. So that ω_{22}^c is the matrix damage parameter under a compressive load, and ε_{22}^c is compression strain in the transverse direction. The damage surface for matrix cracking under compression is written as:

$$\left(\frac{\sigma_{22}}{Y_C}\right)^2 + \left(\frac{\sigma_{12}}{S_{12}}\right)^2 + \Psi_{22}^c = 1 \quad (5.20)$$

The propagation criteria of transverse matrix cracking under compression is Ψ_{22}^c, is written as:

$$\Psi_{22}^t = \frac{G_{22}}{G_{m22}^c} \quad (5.21)$$

Where G_{m22}^c is intralaminar fracture toughness in compression for the transverse direction of the compressive load.

The stiffness degradation is determined based on the damage surface condition as:

$$\left(\frac{E_{22}(1-\omega_{22}^c)\varepsilon_{22}^c}{Y_C}\right)^2 + \left(\frac{\sigma_{12}}{S_{12}}\right)^2 + \Psi_{22}^c = 1 \quad (5.22)$$

The new damage evolution law of matrix cracking under compressive load is now developed as:

$$\omega_{22}^c = 1 - \left(\frac{Y_C}{E_{22}\varepsilon_{22}^c}\right)\sqrt{1 - \left(\frac{\sigma_{12}}{S_{12}}\right)^2 - \Psi_{22}^c} \quad (5.23)$$

It is important to determine the incremental damage constitutive relationship for each damage scenario. The incremental form of the relationship between strain and damage parameter can be obtained for the fibre and matrix using an infinitesimal change in the condition of the damage surface. The procedure below is adopted to consider incremental damage due to matrix cracking under tension load ($\sigma_{22} > 0$).

The criteria for the onset of failure and damage propagation can be written as:

$$F_s = \left(\frac{\sigma_{22}}{Y_T}\right)^2 + \left(\frac{\sigma_{12}}{S_{12}}\right)^2 - 1 = 0 \quad \text{(Damage initiation)} \quad (5.24)$$

$$\Pi_g = \Psi - 1 = 0 \quad \text{(Damage propagation)} \quad (5.25)$$

Therefore, the damage surface can be written as:

$$\mathcal{F}(\sigma, \Psi) = F_s + \Pi_g - 1 \tag{5.26}$$

The incremental damage evolution law can be determined based on the consistency condition, $\dot{\mathcal{F}} = 0$, (Ibrahim and Albarbar 2019) as:

$$\frac{\partial F_S}{\partial \sigma_{22}}(\partial \sigma_{22}) + \frac{\partial F_S}{\partial \sigma_{12}}(\partial \sigma_{12}) + \frac{\partial \Pi_g}{\partial \Psi}\partial \Psi = 0 \tag{5.27}$$

So that,

$$\partial \sigma_{22} = E_{22}(1 - \omega_{22}^t)\partial \varepsilon_{22}^t - E_{22}\varepsilon_{22}^t(\partial \omega_{22}^t) \tag{5.28}$$

$$\partial \sigma_{12} = G_{12}(1 - \omega_{12})\partial \varepsilon_{12} - G_{12}\varepsilon_{12}(\partial \omega_{12}) \tag{5.29}$$

where ω_{12} is the damage evolution in plane 12, due to the in-plane shear stress. The maximum shear stress criterion is adopted here as the damage criterion for shear failures to determine shear damage degradation.

Shear failures is:

$$\left(\frac{\sigma_{12}}{S_{12}}\right)^2 \geq 1 \tag{5.30}$$

The shear failure criteria of damage initiation in plane 12 is substituted in the damage surface as:

$$\left(\frac{\sigma_{12}}{S_{12}}\right)^2 + \Psi_{12} = 1 \tag{5.31}$$

By substituting, $\sigma_{12} = G_{12}(1 - \omega_{12})\varepsilon_{12}$, in above equation, the stiffness degradation is determined based on the damage surface condition as:

$$\left(\frac{G_{12}(1-\omega_{12})\varepsilon_{12}}{S_{12}}\right)^2 + \Psi_{12} = 1 \tag{5.32}$$

Therefore, the new damage evolution law of shear stress can be expressed as:

$$\omega_{12} = 1 - \left(\frac{S_{12}}{G_{12}\varepsilon_{12}}\right)\sqrt{1 - \Psi_{12}} \tag{5.33}$$

and new damage degradation increment ($\partial\omega_{12}$) is written as:

$$\partial\omega_{12} = \frac{(1-\omega_{12})}{\varepsilon_{12}}\partial\varepsilon_{12} \tag{5.34}$$

where G_{12}, ε_{12} represent shear moduli and shear strain, respectively, in plane 12.

Π_g is assumed to be a constant for each increment and is updated at the end of the current increment. According to this assumption $\frac{\partial\Pi_g}{\partial\Psi}$ equals zero, so the incremental damage constitutive relationship can now be expressed as:

$$\frac{\partial\omega_{22}^t}{\partial\varepsilon_{22}^t} = \frac{\frac{\partial F_S}{\partial\sigma_{22}}\left(E_{22}\left(1-\omega_{22}^t\right)\partial\varepsilon_{22}^t\right)+\frac{\partial F_S}{\partial\sigma_{12}}\left(G_{12}(1-\omega_{12})\partial\varepsilon_{12}\right)-\frac{\partial F_S}{\partial\sigma_{12}}\left(G_{12}\varepsilon_{12}(\partial\omega_{12})\right)}{\frac{\partial F_S}{\partial\sigma_{22}}\left(E_{22}\varepsilon_{22}^t(\partial\varepsilon_{22}^t)\right)} \tag{5.35}$$

The same procedure can be followed to develop a new approach to the incremental damage evolution law for matrix cracking under compressive load as well as incremental damage of the fibre.

- incremental damage for matrix cracking ($\sigma_{22} < 0$)

$$\frac{\partial\omega_{22}^c}{\partial\varepsilon_{22}^c} = \frac{\frac{\partial F_S}{\partial\sigma_{22}}\left(E_{22}(1-\omega_{22}^c)\partial\varepsilon_{22}^c\right)+\frac{\partial F_S}{\partial\sigma_{12}}\left(G_{12}(1-\omega_{12})\partial\varepsilon_{12}\right)-\frac{\partial F_S}{\partial\sigma_{12}}\left(G_{12}\varepsilon_{12}(\partial\omega_{12})\right)}{\frac{\partial F_S}{\partial\sigma_{22}}\left(E_{22}\varepsilon_{22}^c(\partial\varepsilon_{22}^c)\right)} \tag{5.36}$$

- incremental damage of fibre ($\sigma_{11} < 0$)

$$\frac{\partial\omega_{11}^c}{\partial\varepsilon_{11}^c} = \frac{1-\omega_{11}^c}{\varepsilon_{11}^c} \tag{5.37}$$

- incremental damage of fibre ($\sigma_{11} > 0$)

$$\frac{\partial\omega_{11}^t}{\partial\varepsilon_{11}^t} = \frac{1-\omega_{11}^t}{\varepsilon_{11}^t} \tag{5.38}$$

(Donadon et al., 2008), (Feng and Aymerich 2014), and (Liu et al., 2016) adopted the damage evaluation law for fibres and matrix in the form:

$(d(\varepsilon) = \varepsilon_{failure}(1 - \frac{\varepsilon_{initiation}}{\varepsilon})/(\varepsilon_{failure} - \varepsilon_{initiation}))$

and incremental damage as:

$\Delta d(\varepsilon) = \varepsilon_{failure}(\frac{\varepsilon_{initiation}}{\varepsilon^2})/(\varepsilon_{failure} - \varepsilon_{initiation})\,\Delta\varepsilon.$

It is clearly seen both damage evaluation law and its incremental are a function of strain during the iterations in each increment. This leads sometimes to severe convergence problems that are often encountered during the non-linear solution procedure of some complicated case studies. To overcome this convergence problem in numerical simulations, the proposed damage evolution law of each damage mode for fibre or matrix takes into account the damage growth function which depends on energy release rate during loading /unloading, and fracture toughness as well as the displacement (strain). In addition, the damage evolution law for the matrix includes the shear stress in plane 12. Also, incremental damage for matrix cracking is a function of the rate of damage initiation, strain, shear moduli, and shear, and as adopted by (Donadon et al., 2008), (Feng and Aymerich 2014), and (Liu et al., 2016) is just a function of strain, so sometimes the numerical solution faces convergence problems. Consequently, it is more sensitive to incremental damage and has more accurate predictions.

5.3 Hypotheses of plasticity model

The direction of flow (damage propagation) can be determined based on the normality hypothesis of plasticity. In this hypothesis, the plastic strain tensor grows perpendicular to the tangent to the yield surface at the load point as shown in Figure 5.5, which represents the von Mises yield surface for isotropic plane stress.

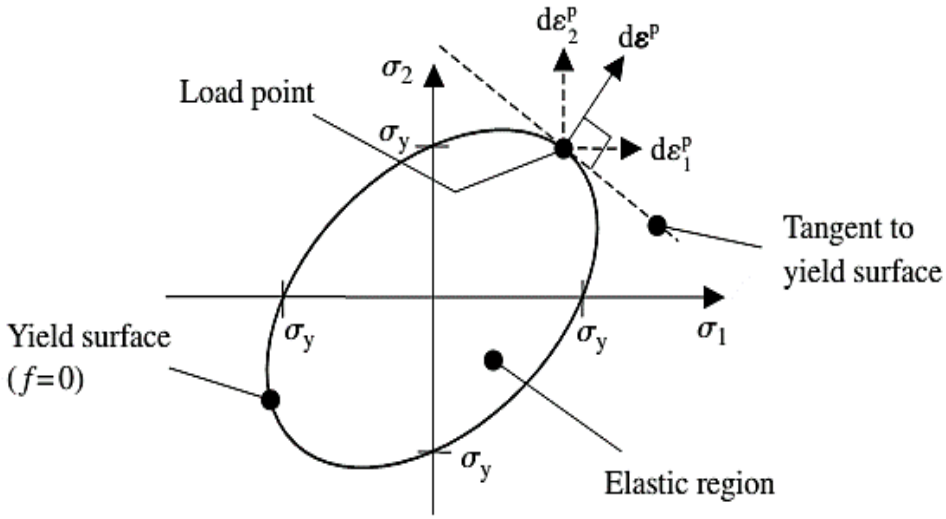

Figure 5.5 Plastic strain increment based on von Mises theory (Dunne and Petrinic 2005)

The failure functions mentioned in the previous section have been adopted here to determine the increment in the plastic strain tensor $d\boldsymbol{\varepsilon^p}$. By using the associated flow rule, the plastic strain can be written in terms of the failure criteria (yield function) as:

$$d\boldsymbol{\varepsilon^p} = d\lambda \frac{\partial F_s}{\partial \boldsymbol{\sigma}} \tag{5.39}$$

while the plastic strain rate ($\dot{\boldsymbol{\varepsilon}}^{\boldsymbol{p}}$) can be expressed as:

$$\dot{\boldsymbol{\varepsilon}}^{\boldsymbol{p}} = \dot{\lambda} \frac{\partial F_s}{\partial \boldsymbol{\sigma}} \tag{5.40}$$

where $d\lambda$ is the plastic multiplier, $\frac{\partial F_s}{\partial \boldsymbol{\sigma}}$ is determined by the direction of plastic flow, and F_s is the yield criterion which is used here as the plastic potential

function (Dunne and Petrinic 2005). The direction of plastic flow of each failure mode can be written as:

- plastic flow of fibre damage (tension or compression)

$$\left(\frac{\partial F_S}{\partial \boldsymbol{\sigma}}\right)_{fibre} = \begin{bmatrix} \frac{\partial F_S}{\partial \sigma_{11}} \\ \frac{\partial F_S}{\partial \sigma_{22}} \\ \frac{\partial F_S}{\partial \sigma_{33}} \\ \frac{\partial F_S}{\partial \sigma_{12}} \\ \frac{\partial F_S}{\partial \sigma_{13}} \\ \frac{\partial F_S}{\partial \sigma_{23}} \end{bmatrix} = \begin{bmatrix} \frac{\partial F_S}{\partial \sigma_{11}} \\ 0 \\ 0 \\ 0 \\ 0 \\ 0 \end{bmatrix} \tag{5.41}$$

- plastic flow of matrix damage (tension or compression)

$$\left(\frac{\partial F_S}{\partial \boldsymbol{\sigma}}\right)_{matrix} = \begin{bmatrix} \frac{\partial F_S}{\partial \sigma_{11}} \\ \frac{\partial F_S}{\partial \sigma_{22}} \\ \frac{\partial F_S}{\partial \sigma_{33}} \\ \frac{\partial F_S}{\partial \sigma_{12}} \\ \frac{\partial F_S}{\partial \sigma_{13}} \\ \frac{\partial F_S}{\partial \sigma_{23}} \end{bmatrix} = \begin{bmatrix} 0 \\ \frac{\partial F_S}{\partial \sigma_{22}} \\ 0 \\ \frac{\partial F_S}{\partial \sigma_{12}} \\ 0 \\ 0 \end{bmatrix} \tag{5.42}$$

To calculate the plastic multiplier, the damage surface consistency condition is applied as:

$$\partial \mathcal{F}(\sigma, \Psi) = \frac{\partial \mathcal{F}(\sigma,\Psi)}{\partial \sigma} \cdot (\partial \sigma) + \frac{\partial \mathcal{F}(\sigma,\Psi)}{\partial \Psi} \cdot (\partial \Psi) = 0 \tag{5.43}$$

The incremental stress–strain equation can be derived based on Hooke's law in incremental form to relate the stress and elastic strains. The explicit incremental of the orthotropic material relationship can be written as:

$$\partial \sigma = C \cdot d\varepsilon^e = C(d\varepsilon - d\varepsilon^p) \tag{5.44}$$

Substituting the plastic strain in the above equation:

$$\partial \sigma = C\left(d\boldsymbol{\varepsilon} - d\lambda \frac{\partial F_S}{\partial \boldsymbol{\sigma}}\right) \tag{5.45}$$

This equation is substituted into the damage surface consistency condition as:

$$\frac{\partial \mathcal{F}(\sigma,\Psi)}{\partial \sigma} \cdot C\left(d\boldsymbol{\varepsilon} - d\lambda \frac{\partial F_S}{\partial \boldsymbol{\sigma}}\right) + \frac{\partial \mathcal{F}(\sigma,\Psi)}{\partial \Psi} \cdot (\partial \Psi) = 0 \quad (5.46)$$

Thus, the plastic multiplier can be obtained as:

$$d\lambda = \frac{\frac{\partial \mathcal{F}(\sigma,\Psi)}{\partial \sigma} \cdot C \cdot d\boldsymbol{\varepsilon} + \frac{\partial \mathcal{F}(\sigma,\Psi)}{\partial \Psi} \cdot (\partial \Psi)}{\frac{\partial \mathcal{F}(\sigma,\Psi)}{\partial \sigma} \cdot C \cdot \frac{\partial F_S}{\partial \boldsymbol{\sigma}}} \quad (5.47)$$

Where C is the effective stiffness matrix, which can be written (Donadon et al., 2008) as:

$$C = \begin{bmatrix} \frac{(1-\omega_{11})E_{11}(1-\nu_{23}\nu_{32})}{\Delta} & \frac{(1-\omega_{22})E_{22}(\nu_{12}-\nu_{13}\nu_{32})}{\Delta} & \frac{E_{33}(\nu_{13}-\nu_{12}\nu_{23})}{\Delta} & & & \\ \frac{(1-\omega_{11})E_{11}(\nu_{21}-\nu_{31}\nu_{23})}{\Delta} & \frac{(1-\omega_{22})E_{22}(1-\nu_{13}\nu_{31})}{\Delta} & \frac{E_{33}(\nu_{23}-\nu_{21}\nu_{13})}{\Delta} & & 0 & \\ \frac{(1-\omega_{11})E_{11}(\nu_{31}-\nu_{21}\nu_{32})}{\Delta} & \frac{(1-\omega_{22})E_{22}(\nu_{32}-\nu_{12}\nu_{31})}{\Delta} & \frac{E_{33}(1-\nu_{12}\nu_{21})}{\Delta} & & & \\ & & & (1-\omega_{12})G_{12} & 0 & 0 \\ & 0 & & 0 & (1-\omega_{13})G_{13} & 0 \\ & & & 0 & 0 & (1-\omega_{23})G_{23} \end{bmatrix} \quad (5.48)$$

$$\Delta = 1 - \nu_{12}\nu_{21} - \nu_{23}\nu_{32} - \nu_{31}\nu_{13} - 2\nu_{13}\nu_{21}\nu_{32}$$

and

$$\omega_{11} = \omega_{11}^t + \omega_{11}^c - \omega_{11}^t\omega_{11}^c$$

$$\omega_{22} = \omega_{22}^t + \omega_{22}^c - \omega_{22}^t\omega_{22}^c$$

The stress-strain constitutive relationship of the damage model is updated as:

$$\boldsymbol{\sigma} = C \cdot d\boldsymbol{\varepsilon}^{\boldsymbol{e}} = C(\boldsymbol{\varepsilon} - \boldsymbol{\varepsilon}^{\boldsymbol{p}}) \quad (5.49)$$

Where,

$$\boldsymbol{\sigma} = [\sigma_{11} \quad \sigma_{22} \quad \sigma_{33} \quad \sigma_{12} \quad \sigma_{13} \quad \sigma_{23}]^T$$

$$\boldsymbol{\varepsilon} = [\varepsilon_{11} \quad \varepsilon_{22} \quad \varepsilon_{33} \quad \varepsilon_{12} \quad \varepsilon_{13} \quad \varepsilon_{23}]^T$$

and

$$\boldsymbol{\varepsilon}^{\boldsymbol{p}} = \left[\varepsilon_{11}^p \quad \varepsilon_{22}^p \quad \varepsilon_{33}^p \quad \varepsilon_{12}^p \quad \varepsilon_{13}^p \quad \varepsilon_{23}^p\right]^T$$

5.4 Validation of proposed damage model

5.4.1 Impact test

Laminated composites have been widely adopted in load-bearing structures because they possess the necessary properties in terms of strength, stiffness, and fatigue resistance. In the most common scenario, the impact loads on the structures are in the through-thickness direction and can lead to serious damage, and this is considered an obstacle to the more widespread use of laminates. The energy released during loading is absorbed through a combination of damage such as intralaminar damage (matrix cracking), fibre breakage and fibre–matrix debonding. As a result, the capacity of composite laminates to carry a load will be significantly reduced when damage takes place. In some cases, such as high velocity impact (ballistic impacts), the damage can be seen by the naked eye. In other cases, especially when the structure is impacted by a low-velocity object, the defect develops internally and it is difficult to discern the damage by the naked eye or external inspection. This internal damage will directly affect the material properties and can lead to a growing but unnoticed degradation in stiffness, so that a consequent sudden failure of the mechanical parts and a catastrophe could happen. A series of experimental tests had been implemented by (Aymerich and Priolo 2008), both drop-weight and compression tests, in their investigation to examine the behaviour of cross-ply graphite/epoxy laminates subjected to low-velocity impact. The development of the damage in the laminates' structure, impact energy, released energy and post-impact behaviour were investigated. They used different, complementary observation techniques e.g., X-

radiography, ultrasonic inspection, optical microscopy, and visual observation to identify internal damage propagation phenomena. Panels of cross-ply sequences $[0_3/90_3]_s$ were used in their experiments with average thickness of the cured panels 2.0 mm. The experiments were carried out using a drop weight testing machine, with rectangular plate of dimensions 65 mm x 87.5 mm, and hemispherical ended impactor 12.5 mm diameter and mass 2.28 kg. To measure the impact velocity of the impactor, an infra-red sensor was employed, and a strain-gauge bridge to measure the contact force between indenter and specimen.

5.4.1.1 Simulation model

In this section, the impact tests performed by (Aymerich and Priolo 2008) are modelled to validate the new approach to a damage evolution law and incremental constitutive relationship for intralaminar damage whether matrix or fibre. The developed models were coded and then implemented in finite element software. The model was divided into three sub-laminates, the thicknesses of the uppermost and lowermost sub-laminates were 0.666 mm with 0^0 fibre orientations, and each was connected to the mid layer (90^0 fibre orientations and 1.332 mm thick) by a cohesive element. The properties of the graphite/epoxy prepreg are presented in Table 5-1 and the actual geometry of the model as mentioned in the previous section is a 65 mm x 87.5 mm rectangular plate. A quarter model was adopted in the ABAQUS software as shown in Figure 5.6. Another sensitivity analysis is presented in this study to illustrate the impact of variation of key inputs to the output/response. Two different shear stresses of cohesive element (40, and 80 N/m^2) have been used to make sure the developed analytical models

response to the input parameters. In addition, two values of fracture energy (970, and 1250 J/m^2) have been adopted to investigate the sensitivity developed analytical models. Figures 5.7 and 5.8 show the delamination width over range of impact energies. Both sensitivity analysis was compared with experimental data obtained by (Aymerich and Priolo 2008), and it is clearly observed that the output/response of the analytical model has good sensitivity to the inputs.

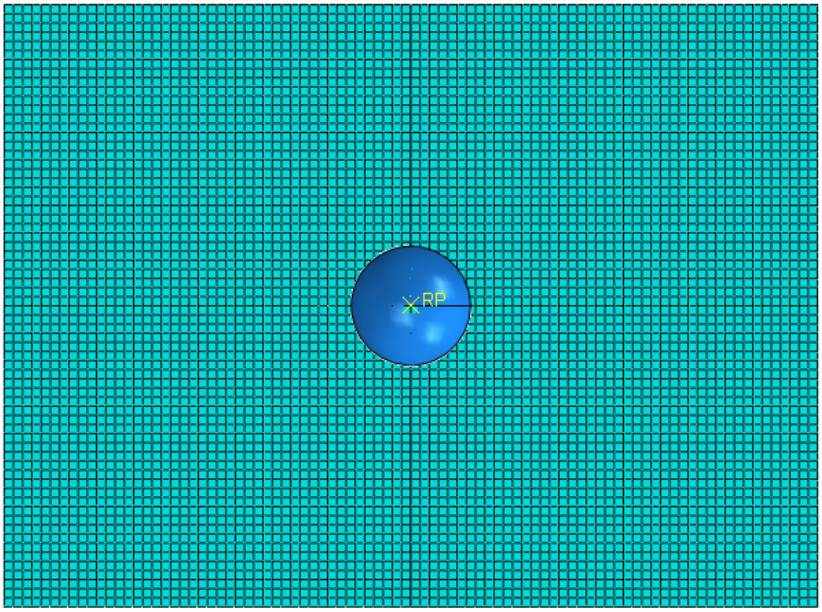

Figure 5.6 A finite element model of cross-ply graphite/epoxy laminates

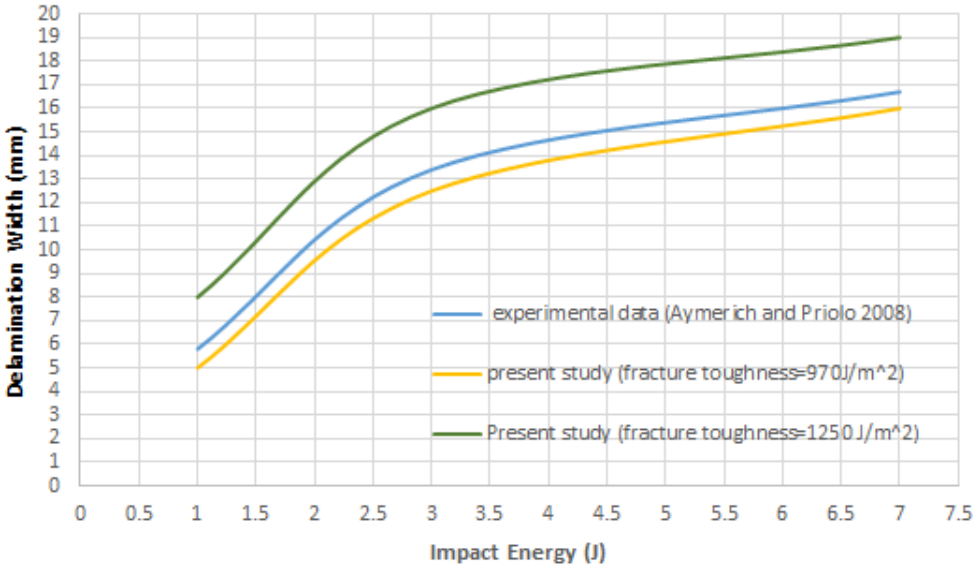

Figure 5.7 Delamination width under different fracture toughness

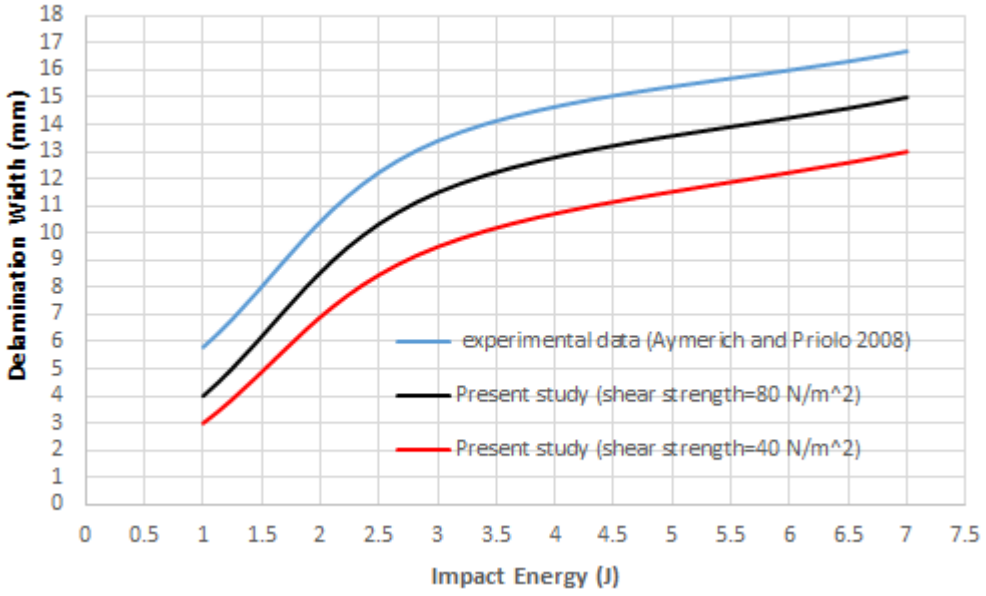

Figure 5.8 Delamination width under different shear strength

It is necessary to update the plastic stresses and strains at each iteration, and a sequence of time steps (t_n, t_{n+1}, t_{n+2}, ...) have been used for discrete iterative solutions. The incremental plastic constitutive model of stress is $\sigma_{n+1} = C\left(\varepsilon_{n+1} - \varepsilon^p_{n+1}\right)$ and incremental plastic strain can be updated as $\varepsilon^p_{n+1} = \varepsilon^p_n + \Delta\varepsilon^p_{n+1}$. The developed numerical model has been investigated for two impact energies 1.0 J and 12.5 J and the simulation findings which are in terms of the impact responses, damage propagation, matrix cracking and delamination interface behaviour are compared with experimental data available in the literature. Transverse matrix damage initially evolves in the layer with fibre orientation of 0^0, at the bottom of the laminate sequence, see Figures 5.9 and 5.10, for results obtained experimentally by (Aymerich and Priolo 2008). These two Figures 5.9 and 5.10 obtained from ABAQUS software represent the lowermost layer and middle layer and the cohesive element between them. They also include the experimental data published by (Aymerich and Priolo 2008).

Table 5-1 Carbon /epoxy properties (Hameed et al., 2020)

Carbon /epoxy properties			
Longitudinal modulus E_1 (GPa)	93.7	Longitudinal tensile strength $X_T\ (MPa)$	1850
Transverse modulus E_2 & E_3 (GPa)	7.45	Longitudinal compressive strength $X_C\ (MPa)$	1470
Shear modulus $G_{12},\ G_{13}, G_{23}$ (GPa)	3.97	Transverse tensile strength $Y_T\ (MPa)$	30
Poisson's ratio $\upsilon_{12}, \upsilon_{13}, \upsilon_{23}$	0.261	Transverse compressive strength $Y_C\ (MPa)$	140
Density $\rho\ (kg/m^3)$	1600	Shear strength S (MPa)	80

Tensile matrix cracking occurs due to tension stress in the lowermost layer, subsequently the damage develops upward into the other plies (middle and uppermost). Figure 5.9 illustrates the tensile matrix crack in the lowermost layer and shear matrix cracks in the 90^0 plies when the specimen was impacted by 1.0 J energy. Figure 5.9 also presents the simulation results based on the new damage evaluation law and incremental damage constitutive relationship. It can be seen that the transverse matrix tension damage obtained from simulation is almost identical with the X-radiographs of the impact damage. As the damage moves upwards into the middle layer with fibre orientation of 90^0, the matrix cracking propagates along 90^0 plies. The same behaviour for damage growth was observed in the middle layer for both simulated and experimental results. Another type of damage was diagnosed at the interface between bottom and middle layers, this failure is

known as interface delamination and it propagates in the same direction as the fibres in the bottom layer (0^0 fibre orientation), see Figure 5.9.

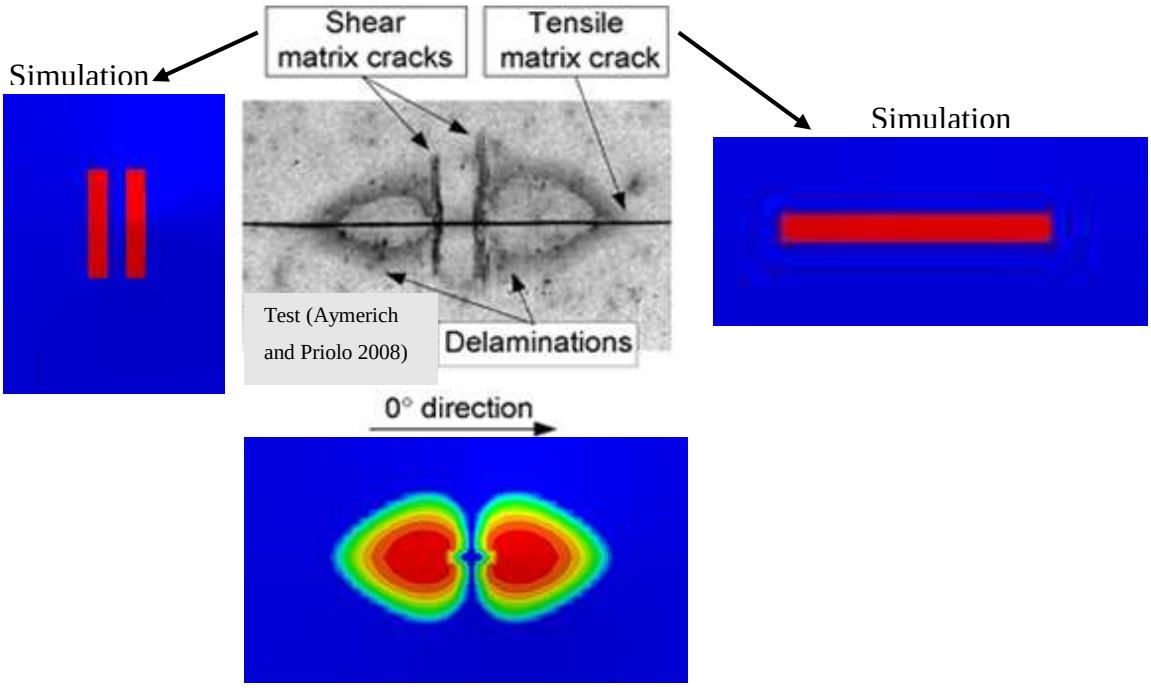

Figure 5.9 Matrix cracking and delamination compared with experimental data obtained by (Aymerich and Priolo 2008). (impact energy 1.0 J)

With an impact energy of 12.5 J, the tensile matrix crack is seen as three lines parallel to the 0^0 fibre orientation in Figure 5.10. Due to the greater impact force and enlarged contact area between indenter and specimen we see additional shear matrix cracks in the middle layer. The experimental evidence showed two separate delaminated areas propagating as lobes along tensile and shear matrix cracks. In the simulation, it can be seen that the process zones of damage congregate around matrix cracks in both 90^0 and 0^0 plies to produce the delamination lobes. The damage at the interface will take place when the damage parameter reaches unity.

If the process zone is removed from the output solution the distance between lobes observed in experimental data will also be seen in numerical model, as seen in Figure 5.10. Therefore, the developed model of impact damage has the ability to simulate damage behaviour very similar to that observed in the X-radiographs obtained by (Aymerich and Priolo 2008).

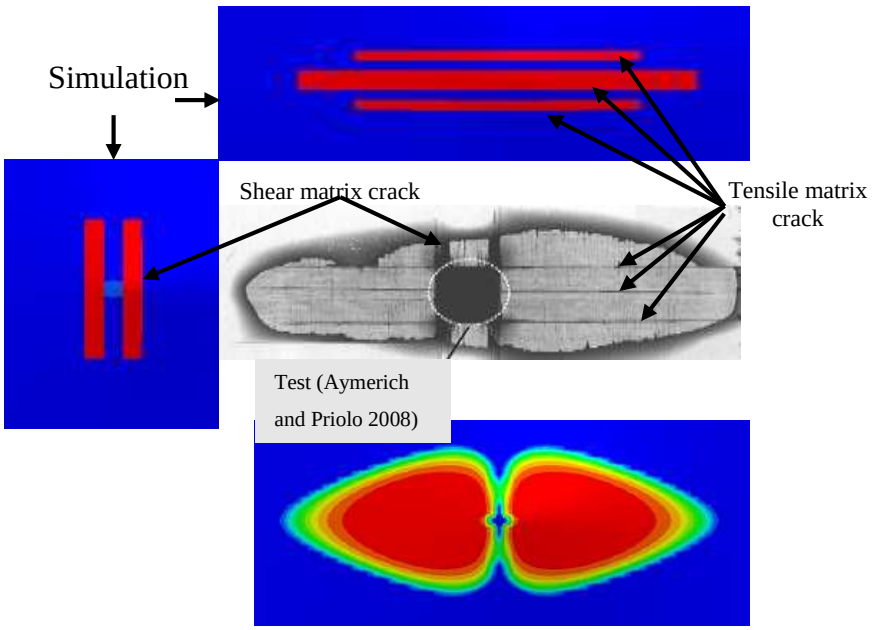

Figure 5.10 Matrix cracking and delamination compared with experimental data obtained by (Aymerich and Priolo 2008). (impact energy 12.5 J)

5.4.2 Open hole tension model

In this section, the tension tests of the holed specimen performed by (Yashiro et al., 2007) are modelled to validate the new approach of composite materials under tensile load. (Yashiro et al., 2007) used CFRP cross-ply laminate (T800H/3631) with stacking configuration $[0_2/90_2]_S$. The specimen was rectangular in shape with a hole (diameter = 5 mm) at the centre. The dimensions of the specimen are illustrated in Figure 5.11.

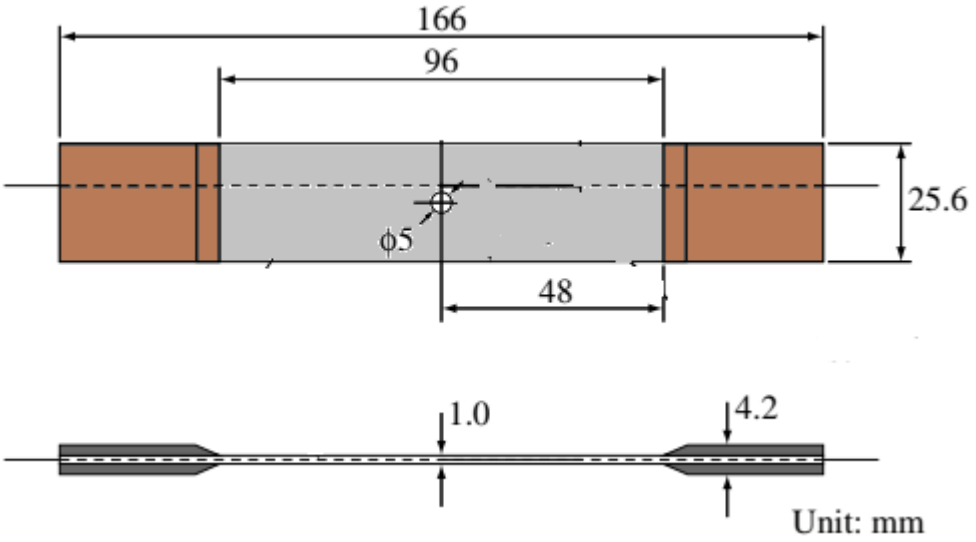

Figure 5.11 Dimensions CFRP specimen (Yashiro et al., 2007)

Quasi-static tensile tests were carried out by (Yashiro et al., 2007) using a universal electromechanical system with a cross-head speed of 0.25 mm/min. Different types of damage can be seen in the experiment test using soft X-ray radiography. The X-ray image obtained by (Yashiro et al., 2007) is shown in Figure 5.12. The transverse cracks are clearly observed at (90^0 ply), and the number increased when the applied load increased.

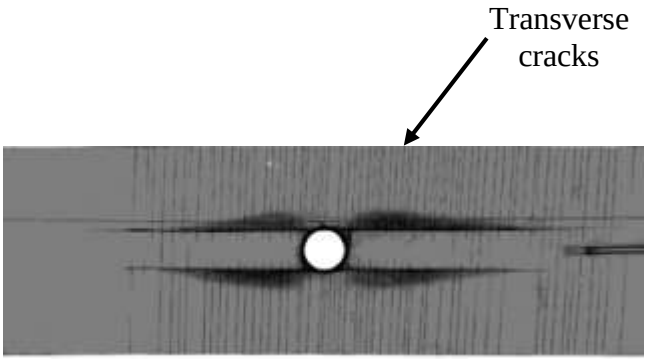

Figure 5.12 X-ray images obtained experimentally (Yashiro et al., 2007)

The holed cross-ply laminate model was divided into two sub-laminates (0^0 fibre orientation and 90^0 fibre orientation of plies) with thicknesses of each layer 0.25 mm thick. Due to the symmetry of the holed specimen, only a quarter model was performed in finite element software to reduce the time-consuming to analyse the model. The simulation results of the specimen under tension load are illustrated in Figure 5.13. It is clearly seen that the damaged region spread (transverse cracks) increased at (90^0 ply) when the applied load increased, this is similar to that presented in the X-ray image. This confirms the validity of the new approach to a damage evolution law for intra-laminar damage.

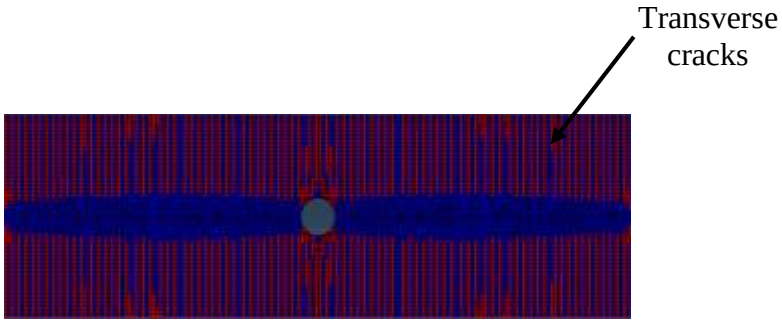

Figure 5.13 Transverse cracks at 90^0 ply using proposed damage model

5.5 Summary

A new expression for the damage parameter of fibres and matrix have been proposed. It also proposes an approach to the matrix damage degradation law. A proposed approach to both the constitutive damage degradation model and increment law was developed to predict intralaminar damage evolution in composite laminates. Failure envelopes for different failure criteria were discussed in term of the fracture plane of matrix cracking under compressive load. The damage surface consistency condition was applied to derive a plastic multiplier as a function of the damage plastic flow so that the plastic strain was updated at each time increment and the stress-strain constitutive relationship of the damage model was also updated. A user-defined subroutine has been adopted to implement a proposed constitutive damage degradation model. The effectiveness of the proposed method has been examined under low velocity impact. The numerical findings confirm that results obtained using the suggested approach are in good agreement with experimental results.

Chapter 6 : Contribution, conclusions, and future work

The contribution of this research are presented in this chapter and it gives a description of how the objectives mentioned in chapter one were achieved. The chapter concludes the main points of study and presents some suggestions for further work.

6.1 Novel feature summary and contribution to knowledge

This study introduced a number of important issues that which are considered new and have not previously fully investigated by other researchers.

The First Novelty: Deriving a realistic inter-laminar damage model and implemented it in ABAQUS using the UMAT subroutine and incorporating thermal effects, alongside delamination growth.

The Second Novelty: Developing a fatigue damage degradation law, and to present a novel rate of fatigue damage ($\partial \mathrm{D}/\partial \mathrm{N}$).

The Third Novelty: Developing a new expression for the damage parameter of fibres and matrix and also developing a new approach to the matrix damage degradation law.

6.2 The contributions to knowledge of thesis:

The First Contribution

Prediction of onset of mixed-mode softening and damage propagation prediction of the cohesive zone model was derived and coded as a UMAT subroutine. After that thermal stress effect on the cohesive zone was obtained and added to the UMAT subroutine to investigate its effects on delamination growth. All results of this objective were presented in Chapter Three.

In addition, it is important to mention that, this work was published in a high-ranked journal: Ibrahim, G. R., & Albarbar, A. (2019). A new approach to the cohesive zone model that includes thermal effects. **Composites Part B: Engineering**, 167, 370-376.

The Second Contribution

Fatigue damage degradation was derived based on the relation between damage evaluation and damaged length ratio. So that the evaluation of the rate ($\partial \mathrm{D}/\partial \mathrm{N}$) is a function of the novel term ($\partial D/\partial L_d$) and the damage growth rate ($\partial L_d/\partial N$) over the process zone. The effectiveness of the new rate of fatigue damage ($\partial \mathrm{D}/\partial \mathrm{N}$) was assessed using experimental data available in the literature. The results are presented in Chapter Four. This work was also published in a high-ranked journal: Ibrahim, G. R., Albarbar, A., & Brethee, K. F. (2021). Progressive failure mechanism of laminated composites under fatigue loading. **Journal of Composite Materials**, 55(1), 137-144.

The Third Contribution

Derivation of a damage degradation model and incremental law for Intra-laminar failure was achieved in this study. The proposed damage evolution law takes into consideration energy release rate during loading /unloading, fracture toughness as well as strain. Validation of the proposed damage model of laminated composites was performed via the impact simulation model and open hole tension model. This work was published in a high-ranked journal: Ibrahim, G. R., Albarbar, A., & Brethee, K. F. (2022). Damage degradation modelling for transverse cracking in composite laminates under low-velocity impact. **Engineering Fracture Mechanics**, 263, 108286.

6.3 Conclusions

6.3.1 Cohesive zone model that includes thermal effects

The objective of the proposed method was and remains to develop a damage model that includes the effect of temperature on the unidirectional laminated composite response. The numerically predicted results were in a good agreement with experimental data and revealed the underlying toughening mechanisms as an increase in the damage initiation stress at cryogenic temperatures by $\tau_{thermal} = k\alpha\Delta T$, which enhanced the fracture energy by $\Delta G = \frac{1}{2}\delta^f \delta^c \left[\left(\frac{\tau_c^{new}}{\tau_c}\right)^2 - 1\right]$. In addition, the damage onset and final failure displacement were changed with the embrittlement of the matrix in unidirectional composite materials at temperatures greater than room temperature, together with the inter-laminar thermal stresses generated in the interface element facilitate the initiation and propagation of damage.

6.3.2 Progressive failure mechanism of laminated composites under fatigue loading

A novel fatigue delamination accumulation mode was presented. The novel approach was tested numerically under two different load conditions: Mode I loading which was performed on a DCB specimen, and Mode II loading which was carried out on an adhesively bonded joint. In addition, the simulation was performed of the mixed-mode model and compared with experimental data available in the literature (Kenane and Benzeggagh 1997) as shown in Figure 6. The simulation findings were compared against experimental results available in literature, the maximum difference between them was 5.0 % for the DCB specimen and 5.2 % for the SLJ

specimen. This is taken as confirmation that the proposed model converges well with experimental data when tested using numerical simulation.

6.3.3 Damage degradation modelling for transverse cracking

Severe environmental conditions including both low-velocity and high-velocity impacts, can cause damages in composite materials. Damage in laminated composites affects mechanical properties (e.g., stiffness degradation) of the composite structure. The developed model based on a computational algorithm was successful in predicting consequential damage and thus, can save hugely in time and money when used to assess the integrity of large structures.

A three-dimensional intralaminar damage model has been developed and implemented in finite element software. Impact response of laminates subjected to impact energies 1.0 J and 12.5 J, has been quantified using the developed approach for predicting intralaminar damage. The observed matrix cracking features, and delamination damage area are discussed. Obtained results have been verified by comparison with experimental tests and it is clearly observed that the maximum central displacement and behaviour response when using the proposed model are very similar to the experimental findings reported in the literature. Also, the results showed that the use of plastic damage model gives consistent results for both impact energies tested.

6.4 Future work

The damage in composite materials is considered a one of the peculiarities in mechanical structures due to the complexities of failures, which consist of three failure modes shapes; fibre, matrix and interlaminar damage

(delamination). Many applications tend to use composite materials in their structure, especially aircraft structures, e.g., wing stringers, fuselage, and the empennage. This work can be extended to explore the more detail the progressive damage in laminated composites. Some suggested future work is pointed out below:

6.4.1 Cohesive zone model related

- A bilinear traction separation law has been adopted in this study to describe the cohesive zone model with and without thermal effects. Further study could be done using a different traction separation law such as exponential, trapezoidal, and polynomial to develop damage degradation in hot environments.

6.4.2 Intralaminar damage related

- Developing the damage evolution law for transverse cracking so that the thermal effect is taken into account.
- Future plans can be set to extend this study to derive a coupling relationship between the damage and plasticity.

6.4.3 Condition monitoring related

- Damage detection in composite materials at an early stage would play an important role in preventing catastrophic failure. Therefore, it is essential to do more research to investigate the best failure detection method in laminated composites.
- Applying signal processing techniques to detect damage (i.e. matrix cracking, and delamination) in wind turbine blades.

6.4.4 Experimental work

- An environmental conditioning chamber could be integrated with the test machine to investigate behaviour of laminated composites at different temperatures.

References

Aktas, M., R. Karakuzu, and Y. Arman. 2009. Compression-after impact behavior of laminated composite plates subjectedto low velocity impact in high temperatures. *Composite Structures* 89 (1):77-82.

Al-Azzawi, A. S., L. F. Kawashita, and C. A. Featherston. 2019. A modified cohesive zone model for fatigue delamination in adhesive joints: numerical and experimental investigations. *Composite Structures* 225 (111114):1-18.

AL-Hadrayi, Z., and Z. Chwei. 2016. Effect the stacking sequences of composite laminates under low velocity impact on failure modes by using carbon fibre reinforced polymer. *The International Journal Of Engineering And Science (IJES)* 5 (2):53-62.

Alfano, G. 2006. On the influence of the shape of the interface law on the application of cohesive-zone models. *Composites Science and Technology* 66 (6):723-730.

Amaro, A. M., P. N. B. Reis, and M. A. Neto. 2016. Experimental study of temperature effects on composite laminates subjected to multi-impacts. *Composites Part B-Engineering* 98:23-29.

Aymerich, F., and P. Priolo. 2008. Characterization of fracture modes in stitched and unstitched cross-ply laminates subjected to low-velocity impact and compression after impact loading. *International Journal of Impact Engineering* 35 (7):591-608.

Ao, W., Zhuang, W., Xing, B., Zhou, Q., & Xia, Y. 2022. Finite element method of a progressive intralaminar and interlaminar damage model for woven fibre laminated composites under low velocity impact. Materials & Design, 223, 111256.

Bak, B. L. V., A. Turon, E. Lindgaard, and E. Lund. 2016. A simulation method for high-cycle fatigue-driven delamination using a cohesive zone model. *International Journal for Numerical Methods in Engineering* 106 (3):163-191.

Bak, B. L. V., Turon, A., Lindgaard, E., & Lund, E. 2017. A benchmark study of simulation methods for high-cycle fatigue-driven delamination

based on cohesive zone models. *Composite Structures* 164:198-206.

Balzani, C., and W. Wagner. 2008. An interface element for the simulation of delamination in unidirectional fibre-reinforced composite laminates. *Engineering Fracture Mechanics* 75 (9):2597-2615.

Barbero, E. J. 2011. *Introduction to Composite Materials Design*. 2nd ed: CRC Press.

Belnoue, J. P. H., S. Giannis, M. Dawson, and S. R. Hallett. 2016. Cohesive/adhesive failure interaction in ductile adhesive joints Part II: Quasi-static and fatigue analysis of double lap-joint specimens subjected to through-thickness compressive loading. *International Journal of Adhesion and Adhesives* 68:369-378.

Bilisik, K., and M. Syduzzaman. 2021. Carbon nanotubes in carbon/epoxy multiscale textile preform composites: A review. *Polymer Composites* 42 (4):1670-1697.

Boominathan, R., V. Arumugam, C. Santulli, A. A. P. Sidharth, R. A. Sankar, and B. T. N. Sridhar. 2014. Acoustic emission characterization of the temperature effect on falling weight impact damage in carbon/epoxy laminates. *Composites Part B-Engineering* 56:591-598.

Boumbimba, R. M., M. Coulibaly, A. Khabouchi, A. Kinvi-Dossou, N. Bonfoh, and P. Gerard. 2017. Glass fibres reinforced acrylic thermoplastic resin-based tri-block copolymers composites: Low velocity impact response at various temperatures. *Composite Structures* 160:939-951.

Bouvet, C., S. Rivallant, and J. J. Barrau. 2012. Low velocity impact modeling in composite laminates capturing permanent indentation. *Composites Science and Technology* 72 (16):1977-1988.

Bunsell, A. R., and J. Renard. 2005. *Fundamentals of Fibre Reinforced Composite Materials*. 1st Edition ed. Boca Raton.

Camanho, P. P., C. G. Davila, and M. F. de Moura. 2003. Numerical simulation of mixed-mode progressive delamination in composite materials. *Journal of Composite Materials* 37 (16):1415-1438.

Cui, W. C., and M. R. Wisnom. 1993. A Combined Stress-Based and Fracture-Mechanics-Based Model for Predicting Delamination in Composites. *Composites* 24 (6):467-474.

Davila, C. G., P. P. Camanho, and C. A. Rose. 2005. Failure criteria for FRP laminates. *Journal of Composite Materials* 39 (4):323-345.

de Moura, M. F. S. F., and J. P. M. Goncalves. 2014. Cohesive zone model for high-cycle fatigue of adhesively bonded joints under mode I loading. *International Journal of Solids and Structures* 51 (5):1123-1131.

de Oliveira, L. A., and M. V. Donadon. 2020. A cohesive zone model to predict fatigue-driven delamination in composites. *Engineering Fracture Mechanics* 235 (107124):1-17.

Donadon, M. V., L. Iannucci, B. G. Falzon, J. M. Hodgkinson, and S. F. de Almeida. 2008. A progressive failure model for composite laminates subjected to low velocity impact damage. *Computers & Structures* 86 (11-12):1232-1252.

Dubary, N., G. Taconet, C. Bouvet, and B. Vieille. 2017. Influence of temperature on the impact behavior and damage tolerance of hybrid woven-ply thermoplastic laminates for aeronautical applications. *Composite Structures* 168:663-674.

Dunne, F., and N. Petrinic. 2005. *Introduction to computational plasticity*. Oxford University Press on Demand.

Ellison, A., and H. Kim. 2020. Shadowed delamination area estimation in ultrasonic C-scans of impacted composites validated by X-ray CT. *Journal of Composite Materials* 54 (4):549-561.

Eghbalpoor, R., Akhavan-Safar, A., Jalali, S., Ayatollahi, M. R., & da Silva, L. F. M. 2023. A progressive damage model to predict the shear and mixed-mode low-cycle impact fatigue life of adhesive joints using cohesive elements. Finite Elements in Analysis and Design, 216, 103894.

Fagan, E. M., C. R. Kennedy, S. B. Leen, and J. Goggins. 2016. Damage mechanics based design methodology for tidal current turbine composite blades. *Renewable energy* 97:358-372.

Feng, D., and F. Aymerich. 2014. Finite element modelling of damage induced by low-velocity impact on composite laminates. *Composite Structures* 108:161-171.

Gornet, L., and H. Ijaz. 2011. A high-cyclic elastic fatigue damage model for carbon fibre epoxy matrix laminates with different mode mixtures. *Composites Part B: Engineering* 42 (5):1173-1180.

Gong, Y., Jiang, L., Li, L., Ren, S., Zhao, Y., Wang, Z., & Hu, N. 2022. Temperature effect on the static mode I delamination behavior of aerospace-grade composite laminates: Experimental and numerical study. Fatigue & Fracture of Engineering Materials & Structures, 45(10), 2827-2844.

Guo, D., Zhou, H., Wang, H. P., & Dai, J. G. 2022. Effect of temperature variation on the plate-end debonding of FRP-strengthened steel beams: Coupled mixed-mode cohesive zone modeling. Engineering Fracture Mechanics, 270, 108583.

Hameed, M. A., G. R. Ibrahim, and A. Albarbar. 2020. Effect of friction and shear strength enhancement on delamination prediction. *Journal of Composite Materials* 54 (23):3329-3342.

Harper, P. W., and S. R. Hallett. 2010. A fatigue degradation law for cohesive interface elements - Development and application to composite materials. *International Journal of Fatigue* 32 (11):1774-1787.

Haselbach, P. U., R. D. Bitsche, and K. Branner. 2016. The effect of delaminations on local buckling in wind turbine blades. *Renewable energy* 85:295-305.

Hashin, Z. 1980. Failure Criteria for Unidirectional Fibre Composites. *Journal of Applied Mechanics-Transactions of the Asme* 47 (2):329-334.

Hashin, Z., and A. Rotem. 1973. Fatigue Failure Criterion for Fibre Reinforced Materials. *Journal of Composite Materials* 7 (Oct):448-464.

Hinton, M. J., A. S. Kaddour, and P. D. Soden. 2002. A comparison of the predictive capabilities of current failure theories for composite

laminates, judged against experimental evidence. *Composites Science and Technology* 62 (12-13):1725-1797.

Ibekwe, S. I., P. F. Mensah, G. Li, S. S. Pang, and M. A. Stubblefield. 2007. Impact and post impact response of laminated beams at low temperatures. *Composite Structures* 79 (1):12-17.

Ibrahim, G., A. Albarbar, A. Abouhnik, and R. Shnibha. 2013. Adaptive filtering based system for extracting gearbox condition feature from the measured vibrations. *Measurement* 46 (6):2029-2034.

Ibrahim, G. R., and A. Albarbar. 2011. Comparison between Wigner-Ville distribution- and empirical mode decomposition vibration-based techniques for helical gearbox monitoring. *Proceedings of the Institution of Mechanical Engineers Part C-Journal of Mechanical Engineering Science* 225 (C8):1833-1846.

Ibrahim, G. R., and A. Albarbar. 2019. A new approach to the cohesive zone model that includes thermal effects. *Composites Part B: Engineering* 167:370-376.

Ibrahim, G. R., A. Albarbar, and K. F. Brethee. 2020. Progressive failure mechanism of laminated composites under fatigue loading. *Journal of Composite Materials*.

Icten, B. M., C. Atas, M. Aktas, and R. Karakuzu. 2009. Low temperature effect on impact response of quasi-isotropic glass/epoxy laminated plates. *Composite Structures* 91:318–323.

Jia, Z. A., T. T. Li, F. P. Chiang, and L. F. Wang. 2018. An experimental investigation of the temperature effect on the mechanics of carbon fibre reinforced polymer composites. *Composites Science and Technology* 154:53-63.

Jiang, H. Y., Y. R. Ren, and B. H. Gao. 2017. Research on the progressive damage model and trigger geometry of composite waved beam to improve crashworthiness. *Thin-Walled Structures* 119:531-543.

Jiang, W., W. Yao, W. Qi, and H. Shen. 2020. Study on the fractal dimension and evolution of matrix crack in cross-ply GFRP laminates. *Theoretical and Applied Fracture Mechanics* 107:102478.

Jousset, P., and M. Rachik. 2014. Comparison and evaluation of two types of cohesive zone models for the finite element analysis of fracture

propagation in industrial bonded structures. *Engineering Fracture Mechanics* 132:48-69.

Kawashita, L. F., and S. R. Hallett. 2012. A crack tip tracking algorithm for cohesive interface element analysis of fatigue delamination propagation in composite materials. *International Journal of Solids and Structures* 49 (21):2898-2913.

Kenane, M., and M. L. Benzeggagh. 1997. Mixed-mode delamination fracture toughness of unidirectional glass/epoxy composites under fatigue loading. *Composites Science and Technology* 57:597-605.

Khojin, A., R. Bashirzadeh, M. Mahinfalah, and R. Jazar. 2006. The role of temperature on impact properties of Kevlar/fibreglass composite laminates. *Composites: Part B* 37 (7-8):593-602.

Khoramishad, H., A. D. Crocombe, K. B. Katnam, and I. A. Ashcroft. 2010. Predicting fatigue damage in adhesively bonded joints using a cohesive zone model. *International Journal of Fatigue* 32 (7):1146-1158.

Kiefer, K. 2014. Simulation of high-cycle fatigue-driven delamination in composites using a cohesive zone model, Department of Aeronautics, Imperial College London.

Kim HS, W. W., Taka Y. 1999. Effects of temperature and fibre orientation on the mode I interlaminar fracture toughness of carbon/epoxy composites. Paper read at Proc 12th Int Conf Compos Mater, ICCM 12

Knight, N. F., Jr. 2006. User-Defined Material Model for Progressive Failure Analysis. NASA.

Landry, B., and G. LaPlante. 2012. Modeling delamination growth in composites under fatigue loadings of varying amplitudes. *Composites Part B-Engineering* 43 (2):533-541.

Liao, B. B., and P. F. Liu. 2017. Finite element analysis of dynamic progressive failure of plastic composite laminates under low velocity impact. *Composite Structures* 159:567-578.

Liu, P. F., B. B. Liao, L. Y. Jia, and X. Q. Peng. 2016. Finite element analysis of dynamic progressive failure of carbon fibre composite laminates under low velocity impact. *Composite Structures* 149:408-422.

Llorca, J., C. Gonzalez, J. M. Molina-Aldareguia, and C. S. Lopes. 2013. Multiscale Modeling of Composites: Toward Virtual Testing ... and Beyond. *Jom* 65 (2):215-225.

Maiti, S., and P. H. Geubelle. 2005. A cohesive model for fatigue failure of polymers. *Engineering Fracture Mechanics* 72 (5):691-708.

Mallick, P. K. 2007. *Fibre-reinforced composites: materials, manufacturing, and design*. 3rd ed: CRC press.

Moroni, F., and A. Pirondi. 2011. A procedure for the simulation of fatigue crack growth in adhesively bonded joints based on the cohesive zone model and different mixed-mode propagation criteria. *Engineering Fracture Mechanics* 78 (8):1808-1816.

Mrazova, M. 2013. Advanced composite materials of the future in aerospace industry. *Incas bulletin* 5 (3):139.

Naghipour, P., M. Bartsch, L. Chernova, J. Hausmann, and H. Voggenreiter. 2010. Effect of fibre angle orientation and stacking sequence on mixed mode fracture toughness of carbon fibre reinforced plastics: Numerical and experimental investigations. *Materials Science and Engineering a-Structural Materials Properties Microstructure and Processing* 527 (3):509-517.

Namdar, Ö., and H. Darendeliler. 2017. Buckling, postbuckling and progressive failure analyses of composite laminated plates under compressive loading. *Composites Part B: Engineering* 120:143-151.

Needleman, A. 1987. A Continuum Model for Void Nucleation by Inclusion Debonding. *Journal of Applied Mechanics-Transactions of the Asme* 54 (3):525-531.

Nojavan, S., D. Schesser, and Q. D. Yang. 2016. A two-dimensional in situ fatigue cohesive zone model for crack propagation in composites under cyclic loading. *International Journal of Fatigue* 82:449-461.

Olsson, R. 2012. Modelling of impact damage zones in composite laminates for strength after impact. *The Aeronautical Journal* 116 (1186):1349-1365.

Ouyang, T., W. Sun, R. Bao, and R. Tan. 2021. Effects of matrix cracks on delamination of composite laminates subjected to low-velocity impact. *Composite Structures* 262 (113354).

Puck, A., and H. Schürmann. 2002. Failure analysis of FRP laminates by means of physically based phenomenological models. *Composites Science and Technology* 62 (12-13):1633-1662.

Reed, R. P., and M. Golda. 1994. Cryogenic Properties of Unidirectional Composites. *Cryogenics* 34 (11):909-928.

Reedy, E. D., F. J. Mello, and T. R. Guess. 1997. Modeling the initiation and growth of delaminations in composite structures. *Journal of Composite Materials* 31 (8):812-831.

Reinoso, J., G. Catalanotti, A. Blazquez, P. Areias, P. P. Camanho, and F. Paris. 2017. A consistent anisotropic damage model for laminated fibre-reinforced composites using the 3D-version of the Puck failure criterion. *International Journal of Solids and Structures* 126:37-53.

Rio, T. G. D., R. Zaera, E. Barbero, and C. Navarro. 2005. Damage in CFRPs due to low velocity impact at low temperature. *Composites Part B-Engineering* 36 (1):41-50.

Robinson, P., U. Galvanetto, D. Tumino, G. Bellucci, and D. Violeau. 2005. Numerical simulation of fatigue-driven delamination using interface elements. *International Journal for Numerical Methods in Engineering* 63 (13):1824-1848.

Sayer, M., N. B. Bektaş, E. Demir, and H. Çallioğlu. 2012. The effect of temperatures on hybrid composite laminates under impact loading. *Composites Part B: Engineering* 43 (5):2152–2160.

Serebrinsky, S., and M. Ortiz. 2005. A hysteretic cohesive-law model of fatigue-crack nucleation. *Scripta Materialia* 53 (10):1193-1196.

Shen, Z. 2015. Characterisation of low velocity impact response in composite laminates, School of Engineering and Technology, University of Hertfordshire.

Shi, Y., T. Swait, and C. Soutis. 2012. Modelling damage evolution in composite laminates subjected to low velocity impact. *Composite Structures* 94 (9):2902-2913.

Shor, O., and R. Vaziri. 2017. Application of the local cohesive zone method to numerical simulation of composite structures under impact loading. *International Journal of Impact Engineering* 104:127-149.

Skvortsov, Y. V., S. A. Chernyakin, S. V. Glushkov, and S. N. Perov. 2016. Simulation of fatigue delamination growth in composite laminates under mode I loading. *Applied Mathematical Modelling* 40 (15-16):7216-7224.

Sridharan, S., and M. Pankow. 2020. Performance evaluation of two progressive damage models for composite laminates under various speed impact loading. *International Journal of Impact Engineering* 143:103615.

Strong, A. B. 2002. History of Composite Materials-opportunities and necessities. *Brigham Young University*.

Sun, C. T., B. J. Quinn, and D. W. Oplinger. 1996. Comparative Evaluation of Failure Analysis Methods for Composite Laminates

Suvarna, R., V. Arumugam, D. J. Bull, A. R. Chambers, and C. Santulli. 2014. Effect of temperature on low velocity impact damage and post-impact flexural strength of CFRP assessed using ultrasonic C-scan and micro-focus computed tomography. *Composites Part B: Engineering* 66:58–64.

Tan, R., J. Xu, W. Sun, Z. Liu, Z. Guan, and X. Guo. 2019. Relationship Between Matrix Cracking and Delamination in CFRP Cross-Ply Laminates Subjected to Low Velocity Impact. *Materials* 12 (23):3990.

Tarfaoui, M., A. El Moumen, and K. Lafdi. 2017. Progressive damage modeling in carbon fibres/carbon nanotubes reinforced polymer composites. *Composites Part B: Engineering* 112:185-195.

Tumino, D., and F. Cappello. 2007. Simulation of fatigue delamination growth in composites with different mode mixtures. *Journal of Composite Materials* 41 (20):2415-2441.

Turon, A., J. Costa, P. P. Camanho, and C. G. Davila. 2007. Simulation of delamination in composites under high-cycle fatigue. *Composites Part a-Applied Science and Manufacturing* 38 (11):2270-2282.

Tvergaard, V., and J. W. Hutchinson. 1992. The Relation between Crack-Growth Resistance and Fracture Process Parameters in Elastic Plastic Solids. *Journal of the Mechanics and Physics of Solids* 40 (6):1377-1397.

Vassilopoulos, A. P. 2015. *Fatigue and fracture of adhesively-bonded composite joints*. 1st edition. ed.

Verma, A. S., N. P. Vedvik, and Z. Gao. 2019. A comprehensive numerical investigation of the impact behaviour of an offshore wind turbine blade due to impact loads during installation. *Ocean Engineering* 172:127-145.

Wang, Y., J. P. Zhang, G. D. Fang, J. Z. Zhang, Z. G. Zhou, and S. Y. Wang. 2018. Influence of temperature on the impact behavior of woven-ply carbon fibre reinforced thermoplastic composites. *Composite Structures* 185:435-445.

Wang, R., Liu, Y., Mao, J., Liu, Z., & Hu, D. 2022. Cyclic cohesive zone model damage parameter acquisition for fatigue crack growth considering crack closure effect. International Journal of Fatigue, 163, 107021.

Wu, Z., L. Shi, X. Cheng, Z. Xiang, and X. Hu. 2020. Transverse impact behavior and residual axial compression characteristics of braided composite tubes: Experimental and numerical study. *International Journal of Impact Engineering* 142:103578.

Xu, X. P., and A. Needleman. 1994. Numerical Simulations of Fast Crack-Growth in Brittle Solids. *Journal of the Mechanics and Physics of Solids* 42 (9):1397-&.

Yang, W., R. Court, and J. Jiang. 2013. Wind turbine condition monitoring by the approach of SCADA data analysis. *Renewable energy* 53:365-376.

Yashiro, S., T. Okabe, N. Toyama, and N. Takeda. 2007. Monitoring damage in holed CFRP laminates using embedded chirped FBG sensors. *International Journal of Solids and Structures* 44 (2):603-613.

Yu, X., B. Zhang, and B. Gu. 2020. Interfacial fatigue damage behavior of fibre reinforced rubber—A combined experimental and cohesive zone model approach. *Polymer Engineering & Science* 60 (6):1316-1323.

Yuan, M., Zhao, H., Xie, Y., Ren, H., Tian, L., Wang, Z., & Zhang, B. 2022. Prediction of stiffness degradation based on machine learning: Axial

elastic modulus of [0m/90n]s composite laminates. Composites Science and Technology, 218, 109186.

Zhang, C., J. L. Curiel-Sosa, and T. Q. Bui. 2017. A novel interface constitutive model for prediction of stiffness and strength in 3D braided composites. *Composite Structures* 163:32-43.

Zhang, X. 1998. Impact damage in composite aircraft structures-experimental testing and numerical simulation. *Proceedings of the Institution of Mechanical Engineers, Part G: Journal of Aerospace Engineering* 212 (4):245-259.

Zhang, B., Allegri, G., & Hallett, S. R. 2022. Embedding artificial neural networks into twin cohesive zone models for composites fatigue delamination prediction under various stress ratios and mode mixities. International Journal of Solids and Structures, 236, 111311.

Zou, Z. M., and M. Hameed. 2018. Combining interface damage and friction in cohesive interface models using an energy based approach. *Composites Part a-Applied Science and Manufacturing* 112:290-298.

Zou, Z. M., and H. Lee. 2017. A cohesive zone model taking account of the effect of through-thickness compression. *Composites Part a-Applied Science and Manufacturing* 98:90-98.

Zuo, Y. J., J. Montesano, and C. V. Singh. 2018. Assessing progressive failure in long wind turbine blades under quasi-static and cyclic loads. *Renewable energy* 119:754-766.